Title
RF Sheath Mitigation and RF Wave Coupling Studies for Optimal ICRF Heating

Author
Bal, Gurleen Kaur

Publication Date
2023

Peer reviewed|Thesis/dissertation

UNIVERSITY OF CALIFORNIA

Los Angeles

RF Sheath Mitigation and RF Wave Coupling Studies for Optimal ICRF Heating

A dissertation submitted in partial satisfaction

of the requirements for the degree

Doctor of Philosophy in Physics

by

Gurleen Bal

2022

ABSTRACT OF THE DISSERTATION

RF Sheath Mitigation and RF Wave Coupling Studies for Optimal ICRF Heating

by

Gurleen Bal
Doctor of Philosophy in Physics
University of California, Los Angeles, 2022
Professor Troy Carter, Chair

Ion cyclotron range of frequencies (ICRF) heating in fusion plasmas is significantly hampered by the phenomenon of RF sheath rectification. Addressing RF sheaths and their related effects, such as impurity generation and convective cell formation, is important to make ICRF an effective heating option for future fusion devices. Experiments were performed on the Large Plasma Device (LAPD) using a single strap ICRF antenna to better understand how to mitigate RF sheath formation and its subsequent effects.

The initial set of experiments explored the effects of electrically insulating antenna enclosures on RF-rectified sheaths. A single-strap RF antenna was powered using a high-power amplifier and matching network. Although the high-power amplifier and matching network were constructed during prior work, some improvements and changes were incorporated for this thesis work. For example, the amplifier, the matching network, and the antenna were modeled using the software LT-spice and simulations helped guide the changes made to the matching network. Additionally, the antenna design was updated to better shield against RF noise otherwise broadcasted into the lab, contaminating several data signals and electronics.

Data from three experiments were compared where the enclosure material was made of

copper, MACOR (electrically insulating), and MACOR over copper, respectively. The non-conductive MACOR material was exposed to the bulk plasma in the case of the MACOR-copper side walls, but a layer of copper was placed below to let image currents flow. All three experiments were carried out in a helium plasma with a background magnetic field of 1kG. In each of these three experiments, a single-strap, high-power (100kW) RF (2.4MHz) antenna was used to launch fast waves into the dense core of the magnetized helium plasma. The core density of the plasma was $n_e \approx 5 \times 10^{12}$ cm^{-3} to 8×10^{12} cm^{-3} during each experiment. No Faraday screens were used on the front face of the antenna enclosure for all three experiments.

In the case of the copper enclosure, RF rectified potentials, many times the local electron temperature, and associated formation of convective cells were observed and reported [1]. The experiments with MACOR and MACOR-copper enclosures showed a considerable reduction in RF rectification. Furthermore, neither of these last two experiments indicated convective cell development. Although the results from the MACOR experiment are reminiscent of the results obtained in ASDEX-U with a 3-strap antenna optimized to reduce image currents on the antenna limiters [2], the MACOR-copper experiment seems to suggest that insulating plasma-facing materials have at least an equally strong impact on reducing potential rectification.

To further explore the DC RF sheath mitigation seen in MACOR and MACOR-copper experiments, another set of experiments were executed with different thickness MACOR enclosures. A 1D voltage divider model by Myra and others has been presented to predict mitigation behavior depending on the insulator material and plasma properties. A series of experiments were conducted to investigate the effect of insulator material qualities and plasma properties on the degree of sheath mitigation. These experiments were conducted using enclosure walls made of copper, 1mm, 2mm, and 5mm MACOR. Also, each experiment was carried out under various plasma conditions by varying the time during discharge when the experiment was performed. RF rectified potentials in the copper enclosure experiment

were used as a benchmark to determine the degree of mitigation in the MACOR studies. Findings from the various MACOR thickness and plasma parameters demonstrate that, with a few exceptions, sheath mitigation often follows the indicated trend of the voltage divider model. Moreover, the model's projected mitigation quantities and the measured sheath potentials do not agree well. To more accurately predict sheath mitigation in these experiments, the voltage divider sheath model will need to consider the 2D impacts of evolving density and plasma potential.

In addition to the sheath mitigation work outlined above, additional work was done to document the parasitic lower hybrid (slow) wave in the LAPD edge. Most fusion experiments where coupling to the slow wave is a concern often have plasma densities and temperatures that are far too harsh for in-vessel diagnostics to be placed in the plasma volume. This work is unique because a fast-wave RF antenna was used to launch fast-wave, typically used for heating, in the core while simultaneously launching the unwanted slow-wave in the edge. Furthermore, this simultaneous coupling of waves was documented using electric dipole probes. Two new dipole probes were developed for this work to allow for better wave propagation mapping along the LAPD's length. One of the big challenges with this work has been achieving a range of densities in the LAPD that span the propagation region of the slow wave and fast wave. With the newly upgraded large LaB_6 source, several different plasma configurations were explored using annular limiters, different species plasmas, and a range of accessible frequencies. After the work done for documenting slow-wave propagation with the new LaB_6 source, we are better equipped to run high-power slow-wave experiments for future work.

The dissertation of Gurleen Bal is approved.

Bart Van Compernolle

George Morales

Chris Neimann

Walter Gekelman

Troy Carter, Committee Chair

University of California, Los Angeles

2022

To my parents and sister for their endless love and support

TABLE OF CONTENTS

LIST OF FIGURES

ACKNOWLEDGMENTS

I would like to take this opportunity to express my deepest gratitude to the individuals who have contributed to my journey and supported me throughout my graduate school experience. First and foremost, I would like to extend my deepest gratitude to my advisor and mentor, Troy Carter. My appreciation for Troy goes beyond his endless knowledge and love for plasma physics. Troy has been an incredible source of guidance and support throughout my research. His endless patience, wisdom, and belief in my abilities have been truly invaluable to my success in grad school. His unique advising style is supportive and gave me the opportunity to take risks and drive my own research. He has empowered me to take ownership of my work and develop confidence in conducting research. In addition to all the research opportunities at UCLA, I'm grateful for all the different ways Troy has helped me access opportunities that have resulted in professional and personal growth. A few of my favorites have been opportunities like fusion day, teaching at Windward, and of course, weekly bikes ride up Mandeville. Thank you for always supporting me as a researcher and a person with interests beyond plasma physics.

I am equally grateful to my co-advisor and collaborator, Bart Van Compernolle. I see Bart as the ultimate guru of RF experiments on the LAPD. From helping me get acquainted with RF experiments to advising me through data runs, providing invaluable feedback, and more, Bart's expertise and support have been indispensable.

I would like to express my sincere appreciation to Pat Pribyl, the wizard of electronics and more, whose expertise has been a crucial asset to my research. During experiments, electronics often failed repeatedly, but Pat's tremendous knowledge and experience consistently helped resolve such issues and made my experiments possible. I would like to thank Shreekrishna Tripathi for his support and patience through countless data runs. I'm beyond amazed by his patience and persistence in troubleshooting any issue during experiments. A special thank you to Steve Vincena for always being my lifeline through all my troubles with

Labview and beyond during data runs.

I would also like to sincerely thank Zoltan Lucky, Marvin Drandell, and Tai Ly for their invaluable support and assistance during each data run. There were countless occasions when we realized that we needed a completely new piece of hardware in the middle of a data run, and with their help, we were able to build such hardware in a matter of hours and continue with the experiment. Lucky, Marvin, and Tai are invaluable resources to the LAPD experiments. I would also like to thank Advit Kohli for his support with experiments and for sharing his expertise of probes.

Additionally, I would like to express my gratitude to my lab mates, who have made every day in the lab exciting and enjoyable. A special thanks goes to Kamil, Phil, and Yhoshua for their unwavering sass, camaraderie, and willingness to entertain my sometimes ridiculous ideas. I am forever grateful for the memorable moments we have shared.

I would like to express my gratitude to Meg Murphy, the best office administrator. Thank you for always being there for all of us students and shielding us from the madness that can be involved with conference travel and other administrative tasks. We started as coworkers with a common connection of growing up in India. Over the years, we have become friends who need to catch up on life events regularly. I'll always cherish our memories and look forward to more in the future.

Lastly and most importantly, I am immensely grateful to my family for their endless love, unwavering support, and understanding. I want to thank my parents, Juspinderpal Kaur and Gursher Singh, my sister, Chandan Kaur, and my brother-in-law, Kaushik Gopal. Their unconditional love, encouragement, and belief in me have been instrumental in my success, and I am forever indebted to them.

Finally, I would like to extend my appreciation to all the individuals, whether mentioned here or not, who have contributed to my growth during this graduate school journey. Your support, encouragement, and contributions have been invaluable, and I am deeply grateful

for the impact you have had on my journey.

VITA

2011-2012	Undergraduate Research Assistant, University of California, San Diego
2012	B.S. (Physics) and B.S. (Mechanical Engineering), University of California, San Diego
2012-2015	Teach For America Corp Member, Los Angeles, CA
2015-2017	Teaching Assistant, Department of Physics and Astronomy, UCLA, Los Angeles, California
2016	M.S. (Physics), UCLA
2017-2023	Graduate Research Assistant, Department of Physics and Astronomy, UCLA, Los Angeles, California

CHAPTER 1

Introduction

Fusion presents a potential long-term energy source that uses an abundant supply of fuel and doesn't generate any long-lived radioactive waste or greenhouse gases. When the nuclei of deuterium and tritium combine in a fusion reaction, an alpha particle and a neutron are released. A decrease in total mass as a result of the nuclear rearrangement causes a release of energy in the form of the kinetic energy of the reaction products. A single deuterium-tritium (D-T) fusion reaction releases 17.6MeV of energy. Heating plasma particles to extremely high temperatures is one of the primary criteria for having an adequate reaction cross-section for achieving fusion. In order to get the plasma to these high temperatures, there are different modes of auxiliary heating which include- ohmic heating, neutral beam injection (NBI), electron cyclotron resonance heating (ECRH), and ion cyclotron resonance heating (ICRH). Each of these methods will be briefly described in the subsections below.

1.1 Heating in Magnetically Confined Fusion Experiments

Auxiliary heating schemes are necessary to heat plasma to fusion reactor temperatures and are additionally needed to control the plasma and current profiles. There are a number of different auxiliary heating schemes available in present magnetic confinement fusion experiments that include ohmic heating, neutral beam injection (NBI), and radio frequency (RF) wave heating. RF wave heating is a blanket term for heating plasma by launching high-frequency electromagnetic waves in the radio frequency regime. Using RF waves to heat the plasma is analogous to heating food using microwaves. The energy being carried by the

EM waves is transferred to the plasma particles by driving them at their respective resonant frequencies. RF heating relies upon three main ways of heating that include- ion cyclotron resonance heating (ICRH), electron cyclotron resonance heating (ECRH), and lower hybrid resonance heating (LHRH). This work mainly focuses on the deleterious effects of ICRH in fusion experiment devices. Therefore, more detail will be provided regarding ICRH in comparison to other methods of heating in the introduction.

1.1.1 Ohmic Heating

Ohmic heating uses the toroidal current to heat the plasma via collisions. But this technique is limited to heating the plasma to around 10 million degrees Celsius because, above this range, the plasma resistivity (collisions) is too low to result in any additional heating. However, a fusion reactor needs to be at least ten times hotter. Other auxiliary methods are used to heat the plasma to these much higher temperatures.

1.1.2 Neutral Beam Injection (NBI)

The basic concept behind NBI heating relies on injecting high-energy neutral atoms into the plasma. These neutral atoms are unaffected by the background field until they are ionized by collisions with the background plasma. After being ionized, these particles are confined by the background magnetic field, and they continue to donate their energy to the background plasma via coulomb collisions. The energy of the neutral beam must be high enough to penetrate the dense core of the plasma. Neutral beam injection will be one of the main heating schemes on ITER. Two or optionally three neutral beams will be injected into plasma, each supplying 16.7 MW of energy via 1MeV deuterium beams [11, 12]. In addition to providing heating for ramp-up, NBI can also provide current drive and induction of plasma rotation [13–15].

1.1.3 Electron Cyclotron Resonance Heating(ECRH)

The mechanism of ECRH capitalizes on the collision-less electron-cyclotron-resonance interaction between the launched wave and electrons. Collisions with ECRH-heated electrons indirectly heat the ions. There are two main mechanisms responsible for electron cyclotron absorption. One mechanism of absorption is the interaction of an elliptically polarized electric field that rotates in the same direction as the electron and has a frequency close to the electron gyro-frequency or one of its harmonics. The second mechanism is the Lorentz force that results from the interaction between the electron velocity, parallel to the static magnetic field, and the wave magnetic field [16, 17]. ECRH is efficient, flexible, localized, and controllable. Either the toroidal field or the poloidal and/or toroidal steering of the launched beam at a fixed magnetic field can be used to control the location of power deposition [16]. The ITER Electron Cyclotron (EC) system will be deployed for electron heating, current drive, current profile tailoring, and control of plasma magneto-hydrodynamic (MHD) instabilities. This EC system will consist of 4 major subsystems, including 12 high voltage power supplies, up to 26 gyrotrons (between 1 to 2MW each), 24 transmission lines, and five launching antennae [18].

1.1.4 Ion cyclotron resonance heating (ICRH)

ICRH is another way of heating plasmas using RF waves. The general process of ICRH can be broken down into three sub-components: generation of RF waves, coupling of RF waves to the plasma, and absorption of RF waves to heat the plasma. The generation of RF waves involves several RF power generation electronics and a physical antenna launcher. Coupling the RF waves from the power generator to the plasma requires an impedance-matched system. This system matches the output impedance of the power generator to the plasma load impedance seen by the antenna. In addition to this impedance matching, the coupling of the RF waves to the plasma is heavily dependent on the plasma parameters near

the antenna. Depending on the dispersion relation, RF waves have their respective regions of propagation, evanescence, resonance, and cut-off. Ion cyclotron range of frequency (ICRF) antennae are often placed in the periphery of the Tokamak, which is often not ideal for coupling to the fast wave, which is responsible for ICRF heating. In the region directly in front of the antenna, the fast wave is often evanescent and starts to propagate once it reaches a high enough density region toward the core. In a Tokamak, we do not have the luxury of placing the RF launcher into the hot, dense core because this would destroy the antenna and disrupt the plasma. Therefore, coupling RF power from the generator to the plasma presents a great challenge and is a current topic of research in the fusion community. Finally, the last component of RF heating includes the different mechanisms of wave absorption. These mechanics include Landau resonance, cyclotron resonance (including harmonics), as well as transit time magnetic pumping.

1.2 Deleterious Effects of ICRH in Fusion Experiments

Although ICRF heating has been widely used for heating in many plasma experiments, many challenges with ICRH are currently being studied and researched. One of the challenges in ICRH includes anomalous coupling to the slow wave. Fig 1.1a shows the fast-wave and the lower-hybrid (slow-wave) dispersion for LAPD-like parameters using the cold plasma dispersion. Fig. 1.1b shows the JET in-vessel view of the ICRH antenna. The yellow arrow in each panel signifies the direction of increasing density. The crucial takeaway from the dispersion plot is the high-density requirement for the desirable fast wave propagation for heating. For the given plasma and antenna parameters in the figure, the fast wave is evanescent below density values of $1.5 \times 10^{18} m^{-3}$, and the slow wave propagates in a good portion of that low-density region. This is problematic because the RF antenna is typically placed in a region of low density in a Tokamak where the fast wave is evanescent, and the antenna couples part of its RF power to the propagating, undesirable, slow wave. The

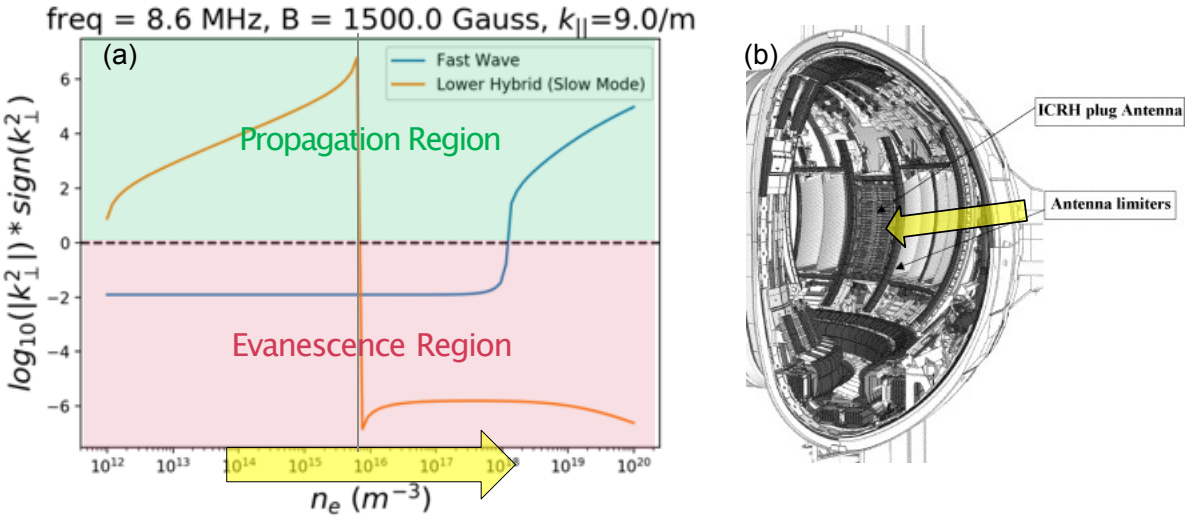

Figure 1.1: (a) Fast wave and lower hybrid wave (slow-wave) dispersion plots for LAPD-like parameters using the cold plasma dispersion. (b) JET in-vessel view of ICRH antenna [3]

propagating slow wave is also associated with the potential risk of far-field sheath effects.

The plasma densities near the antenna, in the outer edge, are typically much lower than the core density. One obvious solution to this challenge would be to push the RF antenna far enough into the core where only the fast wave is able to propagate. Unfortunately, this is not possible. The high density and high-temperature core of the plasma would destroy the antenna, and the antenna would disrupt the plasma.

As a consequence of the RF antenna position in the SOL, there are a number of ICRF heating challenges linked to the non-linear interaction between the low-density plasma and the antenna. One of these effects includes near-field sheaths. Near-field sheaths occur when field lines containing plasma contact with conducting surfaces. Due to the complex 3D structure of the antenna, adjacent grazing field lines can start and end at very different locations, resulting in different sheath voltages. This variation in sheath potential typically results in a perpendicular (with respect to the background magnetic field) electric field that drives EXB convection. This EXB convection is also referred to as RF convection.

1.3 Relevant Results on RF Sheaths

1.3.1 Alcator C-Mod

The Alcator C-Mod Tokamak was used in the experiment with a toroidal field strength of approximately 5.4T, a minor radius of around 0.22m, and a major radius of about 0.67m [19]. The plasma was heated using 6MW of ICRH power at 50, 78, 80, and 80.5MHz. Additionally, 1.2MW of LH power at 4.6GHz was used for non-inductive current drive [20]. The plasma potential in the scrape-off-layer (SOL) was measured using a hot emissive probe [21] and an ion-sensitive probe [4,22], which were mounted on a reciprocating probe. An estimate of the plasma density was obtained via the Isat collected by the ion-sensitive probe and temperature from the Langmuir probes. As depicted in Fig. 1.2, the results from this work documented rectified plasma potential up to 200 Volts and found that there was a density threshold of $1 \times 10^{16} m^{-3}$ above which these rectified potentials were documented. Their finding also showed that plasma potential rectification occurs in ICRH heated discharges and is attributed to the slow ICRH waves propagating along open magnetic field lines and striking material surfaces [4]. Additional results from C-MOD documented sheath rectification associated with fast wave rectification that was unlike slow-wave rectification and not local to active RF antennas. These results also showed a correlation between plasma potential, ϕ_p, and fast wave intensity values [23].

1.3.2 Attenuation of ICRH-induced potentials in the SOL of Tore Supra

The Tore Supra Tokamak, equipped with three plasma heating antennas, was used to study ICRH-induced potentials as a function of edge density. The antennas operate in the range of 42-63MHz, injecting a maximum of 4MW of heating power per antenna. These antennas consist of a 2-strap phased array centered at the equatorial plane with poloidal limiters on either side of the antenna to protect the straps from plasma SOL [24]. While high potentials are detected across the leading edge of the poloidal limiters, the highest potentials are seen

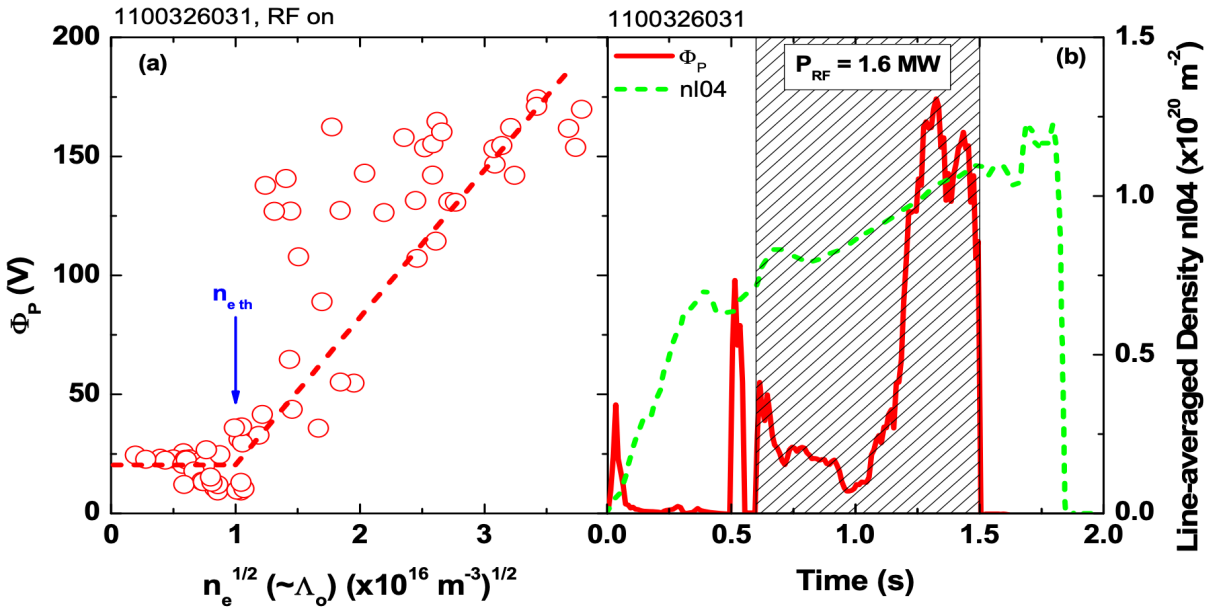

Figure 1.2: (a) Relation between the measured plasma potential, Φ_p, and the local density, n_e, in presence of constant 1.6 MW of ICRH power. The active antenna was magnetically mapped to the probes, $R_{probes} = R_{Limiter} = 0.910m$. (b) Time trace of the plasma potential measurements during a core density sweep. Figure from experiments performed on CMOD [4]

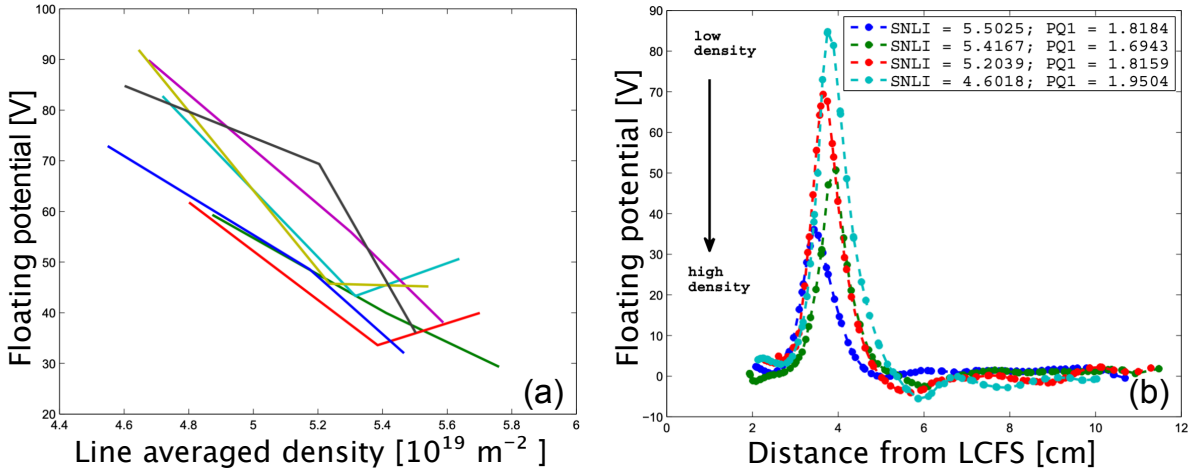

Figure 1.3: (a) Density dependence of floating potential structures for different magnetic connections. (b) and for one specific position on the antenna. Figure from experiments on Tore Supra [5]

near the top and bottom of the antenna straps. In these experiments, the floating potential is used as a lower estimate for the plasma potential. Potential values up to 200 Volts were measured during these studies. Additionally, as shown in Fig. 1.3 these results also showed that the amplitude of floating potential perturbation decreases with increasing density. Therefore, this work suggests control of edge density could provide a way to attenuate RF sheath potential in ICRH-heated Tokamaks [5].

1.3.3 ASDEX-Upgrade (AUG)

Three approaches were investigated as part of work done on the ASDEX Upgrade (AUG) to lower the tungsten (W) concentration at the plasma edge after tungsten yield (YW) at the antenna limiters and PFCs during ICRF [25]. These approaches include increasing the separatrix-antenna clearance, increasing the gas puffing rate, and operating the neighboring antenna at the phase difference close to -90 °. Antenna 4 had W-coated shields covering the antenna corners, where the magnetic field lines cross just one antenna strap to explore

how the antenna straps affect $V_{\|}$. Spectroscopic monitoring was performed on the W-coated antenna limiters. The radial profile of the tungsten and hydrogen D(H) line intensities were gathered from several lines of sight locations. These intensities were then used to get measurements of particle fluxes.

In addition to the spectroscopic measurements, calculations with 3-D finite element HFSS code were used with a planar antenna model to calculate $E_{\|}$ and $V_{\|}$ at the antenna plane (close to the surface of the antenna limiters). These calculations corroborate the findings that in AUG, the box currents play a dominant role in forming sheath driving voltages on the magnetic field lines connecting to the antennas [25].

Following the motivation from the work described above, additional work has been done on AUG that used the local value of $E_{\|}$ as a figure of merit for minimizing RF sheath effects [6]. Particularly reducing $E_{\|}$ field values close to the radially protruding antenna side limiters. The 3-strap ICRF antenna was used for this work. The general principle is that the individual antenna straps are phased and powered with respect to each other to minimize image currents in the side limiters. The top row in Fig. 1.4 shows three different configurations of power ratio between the central and outer straps- $P_{cen}/P_{out} = 0.1$, $P_{cen}/P_{out} = 2$, $P_{cen}/P_{out} = 10$. For the case where $P_{cen}/P_{out} = 2$, the best cancellation of image currents is achieved on both the left and right sides of the antenna box [6]. The bottom row in Fig. 1.4 shows the subsequent effect of image current cancellation on the $E_{\|}$ fields. Re($E_{\|}$) in front of the antenna was calculated using the linear electromagnetic TOPICA code [26]. Note that the reduction in $E_{\|}$ fields is location dependent along y.

RF voltage, V_{RF} was measured at the limiters of the antenna at several locations and compared to the TOPICA flat-model calculation of the spatial averaged $E_{\|}$ as a function of the strap power ratio (P_{cen}/P_{out}), and phase ($\Delta\Phi$) between straps at the same locations as the experimental measurements. The comparison between the measured values and calculations agrees well about the existence of the minima of the RF quantities. The comparison also agrees on how changes in the power ratio values impact these minima from location to

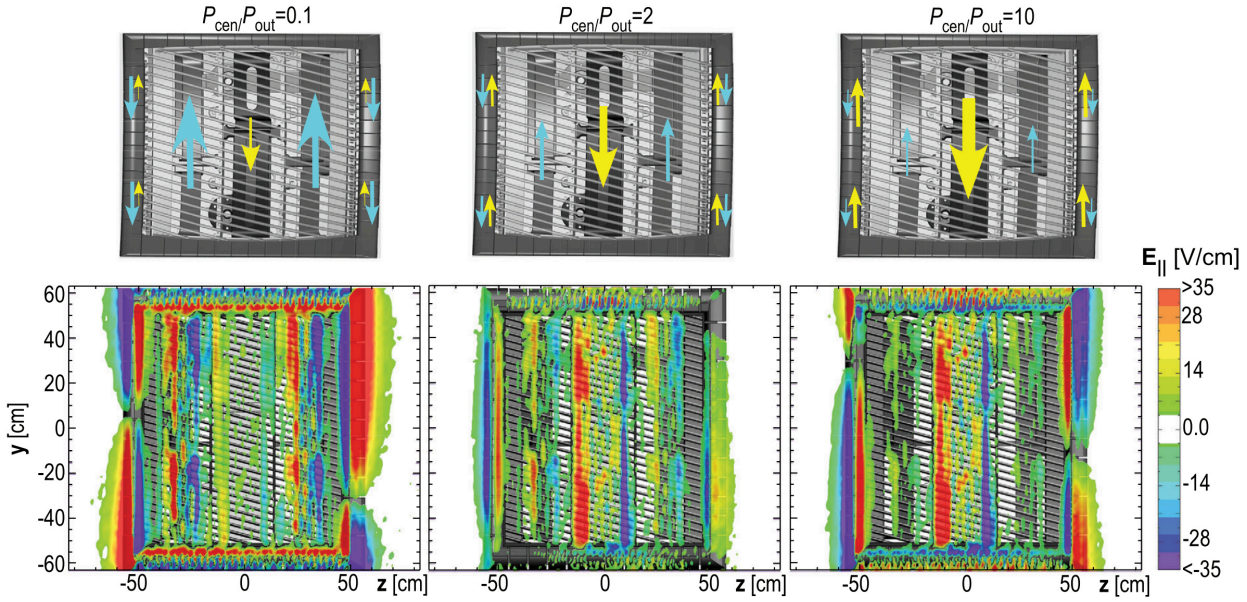

Figure 1.4: Upper row: the RF image current cancellation close to a power ratio of 2:1 (middle) in dipole phasing, compared to a power ratio of 1:10 (left) and 10:1 (right). The 3-strap antenna is shown using a CAD view with every second FS rod removed. Lower row: the corresponding TOPICA calculations of Re ($E_{||}$) at 36.5 MHz, 0.5 MW power, in a plane in front of a flat model of the antenna. Figure from [6]

location. In some locations, the exact values of the strap power ratio and the minima show a less good agreement. The strong temporal and spatial perturbations of the density profile in front of the antennas that are present during plasma discharges are likely responsible for such discrepancies. Additionally, the data's limited phase resolution and differences between the real geometry and the antenna's modeling geometry are likely responsible for the lack of agreement between measurements and calculations [6].

The overall results from this work suggest that the E-field must be primarily lowered on radially protruding structures where the RF sheaths can form in order to reduce the plasma-wall interactions adjacent to the antenna. This suggests that the RF currents on such structures should be kept to a minimum.

1.4 Thesis Outline:

This thesis describes the work done to understand better and mitigate the deleterious effects of ICRH with experiments on the LAPD. This work mainly focuses on the rectified RF sheath effects that arise in the vicinity of an ICRF antenna. Chapter 2 describes the Large Plasma Device (LAPD), diagnostics, the RF antenna, the RF antenna amplifier electronics, and data analysis methods used in this work. Chapter 4 focuses on results from three sets of experiments on the LAPD that show that DC RF sheaths can be mitigated by the use the electrically insulating MACOR and MACOR-copper stack antenna enclosure walls. The first experiment was done with copper enclosure walls, and the results characterize the DC RF sheath potentials and subsequent $E \times B_0$ flows in the plasma. This experiment's results also include wave field measurements and power-scaling measurements for the RF sheath potentials. Using this first experiment as a benchmark, two additional experiments were performed using different antenna enclosure wall materials to measure their impact on DC RF sheath potentials. These included one experiment with MACOR sidewalls and an additional set of experiments with MACOR-copper stack sidewalls. These experiments aimed to explore the effects of image currents and a DC electrical connection between the enclosure sidewalls and the bulk plasma on sheath rectification. For the case of MACOR enclosure sidewalls, there was neither an electrical connection between the sidewall and the bulk plasma nor any image currents. And for the case of MACOR-copper stack sidewalls, image currents were allowed to exist in the inner layer of copper. Still, the DC electrical connection between the sidewalls and the bulk plasma was broken by the MACOR covering the copper. Chapter 4 details the comparison of all three experiments' results. Afterward, chapter 5, describes the work done to understand better sheath mitigation results presented in the previous chapter. A series of experiments were performed on the LAPD with different thickness MACOR walls (1mm, 2mm, and 5mm) to understand the impact of material properties on the extent of sheath mitigation. Additionally, these experiments were carried out during varying plasma conditions by varying the time during discharge when the experiment was

performed. Chapter 6 details the progress made in the RF wave coupling studies carried out on the LAPD. The focus of this work was to document slow-wave propagation in the low-density edge of the LAPD via the single-strap RF antenna designed for launching fast-waves in the dense core of the machine. Finally, chapter 7 includes concluding remarks and future experiments that can be done in continuation of this research work.

CHAPTER 2

Experimental Setup

2.1 The Large Plasma Device (LAPD)

The Large Plasma Device (LAPD) is a 26-meter-long linear plasma device housed at the Basic Plasma Science Facility at the University of California, Los Angeles (UCLA). It was originally constructed in 1991 to research Alfvén waves [27]. It has since undergone several upgrades and become a national user facility for the study of basic plasma physics [28]. Since the most recent upgrades, the LAPD generates an 18m long, quiescent magnetized plasma at a high repetition rate using two Lanthanum Hexaboride (LaB_6) cathodes on either end of the machine. Fig. 2.1 shows a composite photograph of the exterior of the machine before the cathode upgrade in 2021.

2.1.1 Plasma Generation Process

The plasma in the LAPD is generated by two emissive cathodes located at either end of the machine. Each cathode can be run independently and can achieve different temperatures, densities, and plasma diameters. Prior to the cathode upgrade in 2020, there was a 60cm diameter Barium Oxide (BaO) source on the south end of the machine. This source consisted of a nickel substrate that was coated with a thin ($\sim 50\mu m$) layer of BaO. This source was capable of producing discharge densities between 10^{10} cm^{-3} to 2×10^{12} cm^{-3} with an electron temperature up to 5eV. Since the 2020 cathode upgrade, this source has been replaced by a 38cm diameter Lanthanum Hexaboride (LaB_6) cathode. The new LaB_6 source is capable

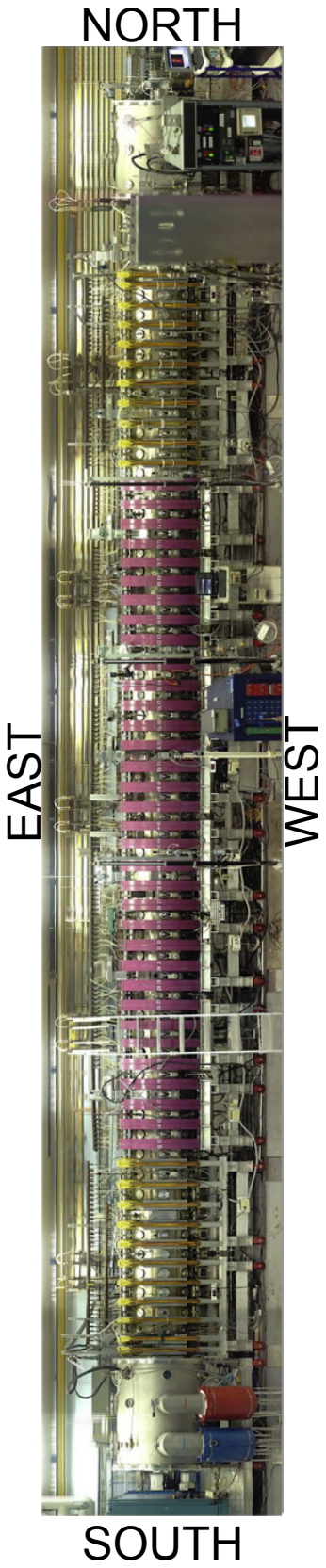

Figure 2.1: Panoramic image of the LAPD before the most recent cathode upgrade in 2020.

of producing discharge densities between 2×10^{11} cm^{-3} to 2×10^{13} cm^{-3} with an electron temperature up to 12eV. A molybdenum mesh anode is located 50cm away from the LaB_6 cathode. The cathode is indirectly heated to $\sim 1700°C$ and made to emit electrons. The cathode-anode assembly is biased to accelerate the emitted electrons across a potential of up to 140 Volts. The electron beam then ionizes and heats the neutral gas in the chamber.

On the south end of the machine, there is a removable LaB_6 cathode composed of 4 square LaB_6 tiles that are held together in a tongue and groove arrangement to form a 20cm by 20cm square source. This source is heated to $\sim 1850°C$ for maximum emission, which requires about $50kW$ of DC power. This source can produce densities up to 3×10^{13} cm^{-3} and an electron temperature up to $12eV$.

An independent set of power supplies and capacitor banks supports each of the cathodes. For typical operation, first, the cathode heater is brought up slowly at about $2A/min$ while monitoring the pressure level of impurities. To create the discharge, the anode is biased with respect to the cathode. Each of the sources has its own power bank and respective power supply, and they are typically biased between 80V to 170V. High discharge voltages typically correspond to higher density and hotter electron temperature. The two sources can be pulsed simultaneously or with a delay with respect to each other for varying discharge lengths.

2.1.2 Magnetic Field

The axial field in the LAPD is generated by a set of purple and yellow electromagnets, as seen in Fig. 2.1. These magnets are powered in a steady state by a set of 15 power supplies that power sections of adjacent electromagnets in parallel, providing a field strength between $175G$ to $3000G$. This allows for variable background magnetic field profiles.

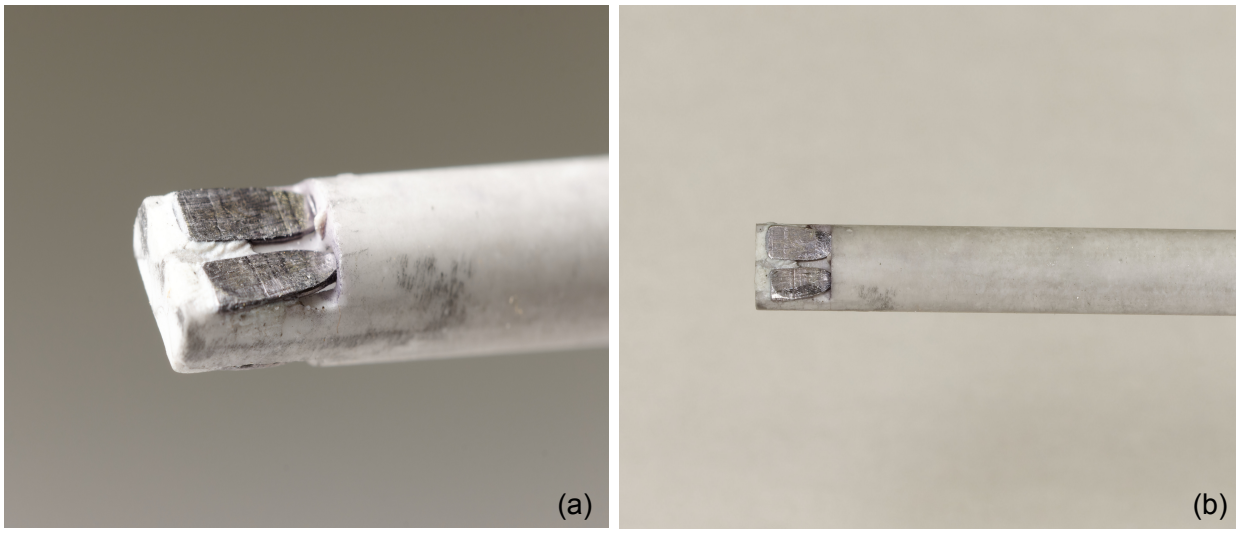

Figure 2.2: (a) A picture of the Langmuir probe tips, which are flattened Tungsten conductors. (b) A picture of the Langmuir probe tip shows the ceramic tube holding the Tungsten conductors.

2.2 Diagnostics

2.2.1 Langmuir Probes

Langmuir probes are one of the most commonly used diagnostics on the LAPD. Fig. 2.2 shows two pictures of the probe tip for Langmuir probes used in this work. They are often used to determine the density, potential, and electron temperature of the plasma. Langmuir probes often consist of one or more conductors that are inserted into the plasma while the probe is biased at a constant or varying potential.

The ion saturation current measurement is a prominent measurement often made using Langmuir probes. For this measurement, the probe is biased, with respect to the vessel wall, well below the plasma potential. The current collection at the probe tip is measured and digitized at the ion-saturation current. Assuming cold ions, the ion saturation current is given by:

$$I_{isat} = e^{-1/2} A_{eff} q_i n_i \sqrt{\frac{T_e}{m_i}} \tag{2.1}$$

Where A_{eff} is the effective probe area, q_i is the ion charge, n_i is the ion density, T_e is the electron temperature, m_i is the ion mass. A_{eff} is used to calculate I_{isat} since a large negative bias can form a Debye sheath on the probe area, which effectively increases the ion collection area at the probe tip. For plasmas where the Debeye length is small compared to the probe area, the probe area can be used as the effective collection area.

If we consider the fluctuations in I_{isat} due to the ion density and electron temperature, we get:

$$\delta I_{isat} = I_{isat}\left(\frac{\delta n}{n_i} + \frac{\delta T_e}{2T_e}\right) \tag{2.2}$$

In the case that the relative fluctuations in temperature are small compared to the relative fluctuation in density, we use fluctuations in I_{isat} as a proxy for fluctuations in density. In subsequent chapters, fluctuations in the I_{isat} signal will be used to represent fluctuations in plasma density.

The plasma potential, V_p, and electron temperature, T_e, can be obtained by sweeping through a range of voltages for the Langmuir probe tip bias and recording the current collection response, also known as the $I-V$ curve. The $I-V$ sweep analysis theory is documented in detail in several works of literature [29, 30]. The $I-V$ curve can be split into three main regions- the ion saturation region, the transition region, and the electron saturation region. In a Maxwellian plasma with thermal electrons and cold ions, the electron current at the probe tip is given by:

$$I_e(V) = A_{eff} q_e n_e \sqrt{\frac{KT_e}{2\pi m_e}} e^{\frac{-q_e(V-V_p)}{KT_e}} \tag{2.3}$$

A_{eff} being the effective collection area of the probe, q_e is the electron charge, n_e is the electron density, K is the Boltzmann constant, T_e is the electron temperature, m_e is the electron mass, V is the probe bias, and V_p is the plasma potential. Eqn. 2.3 is used to determine the electron temperature, T_e for the $I-V$ response. Taking the Ln of both sides in eqn. 2.3, we can determine the electron temperature by finding the slope of the $\ln I_p$ in the

transition region. The slope of the linear transition region is equal to $1/T_e$ where T_e is given in electron volts (eV). Although the electron saturation region can be used to determine the plasma density in the plasma, making this measurement using an ion saturation measurement is considered more reliable.

2.2.2 Emissive Probes

One of the main challenges of measuring plasma potential with a swept probe is the speed at which the probe can be swept. This speed dictates the fastest time variation in plasma potential that can be measured using a swept probe. If the time variation of the plasma potential is much faster than the speed at which a probe can be swept, a floating measurement can be used to measure plasma potential by proxy. In relation to the floating potential, plasma potential is given by:

$$V_p = V_f + \alpha \frac{T_e}{e} \tag{2.4}$$

Here V_p is the plasma potential, V_f is the floating potential, α is a parameter that characterizes the probe sheath, T_e is the electron temperature, and e is the elementary charge. For an emitting probe, when the emission is high, the relationship between plasma potential, floating potential, and electron temperature is the same as eqn. 2.4. A number of models can be used to determine α, and most of them result in $\alpha = 1$. One of the disadvantages of using a cold probe for V_f measurements is the limitations on the temporal responses given the formation of the capacitive sheath at the tip of the cold probe. With an emitting probe, the sheath characteristics change such that an emissive probe is able to track the plasma potential much better than a cold probe [31].

A fundamental design requirement for an emissive probe is that it should be able to emit sufficiently to match the plasma's electron saturation current. The emission current is

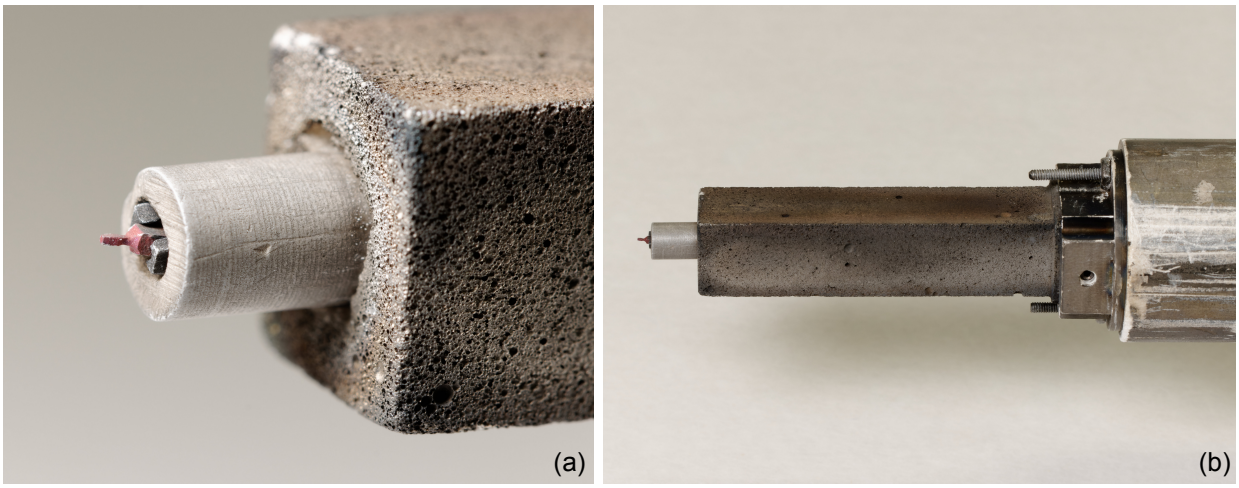

Figure 2.3: (a) A picture of the emissive probe tip between carbon levers. (b) A picture of the emissive probe assembly, including the boron-nitride sleeve covering the carbon lever assembly.

determined by the Richardson-Dushman equation:

$$J = AT^2 e^{-\phi/k_B T} \tag{2.5}$$

In this equation, J is the emitted current density, A is the Richardson constant, T is the material temperature in Kelvin, ϕ is the work function in eV, and k_B is the Boltzmann's constant. A thoriated tungsten filament is often used for common emissive probe applications. But in order to get sufficient emission for the LAPD plasma density range, the tungsten tip would need to be heated beyond its temperature dictate structural limits. Therefore materials with a lower work function are necessary to achieve sufficient emission at a reasonable temperature. Cerium Hexaboride, CeB_6, and Lanthanum Hexaboride, LaB_6 have an adequately low work function and are structurally stable at the necessary temperature.

Fig 2.3 shows an image of the emitting tip as well as an image of the probe assembly that holds the emitting tip between two carbon levers. The carbon tweezers are not visible in this image since a boron-nitride sleeve has been put over the assembly to protect and hold the

assembly in place. The emissive probe is heated using a 150kHz power inverter, transformer-coupled to drive current in the floating probe configuration. More information about the design of the probe and heating circuit can be found in [32]. For the general operation, the emissive probe is heated slowly by increasing the heating current by 2-5 amps every 5 minutes. If the probe has been exposed to air, the tip will likely out-gas surface contaminants, and additional time in the heating process is ideal. In the experiments presented in this thesis, the probe tip often starts visibly glowing near 40-60 Watts of heating power. The tip is placed in the highest plasma density region for obtaining operational heating power while it is connected to sweeping circuitry. The heating power is increased while the $I-V$ characteristics are tracked. As the heating power increases, the floating potential of the tip will start to increase towards the plasma potential and eventually saturate. This is the point of optimal operation. Heating the probe tip further beyond this point will not induce much of a change in the floating potential. At this point, the sweeping circuitry can be disconnected, and the floating potential measurement is able to track the plasma potential.

2.2.3 B-dot Probes

The magnetic wave fields in this work are characterized by B-dot probes which utilize Faraday's law to measure magnetic field fluctuations via induced emf, $V = -A_{eff}\frac{\delta B}{\delta t}$, across deferentially wound loops. V is the voltage measured across the loops, A_{eff} is the effective area of the pickup loop an B is the fluctuating magnetic field. These probes consist of a set of three differential wound loops around a ceramic cube which help detect magnetic field fluctuations in three orthogonal directions in space. The cube is then covered with a ceramic dome to prevent a direct connection between the plasma and the loops. The loops are deferentially wound to cancel out the electrostatic component of pickup. The signal from each set of wires is sent to a differential amplifier that subtracts and amplifies the two signals.

These probes are calibrated using a setup that involves creating a known field and comparing that to the signal pickup from the B-dot loops. This is done using a vector network

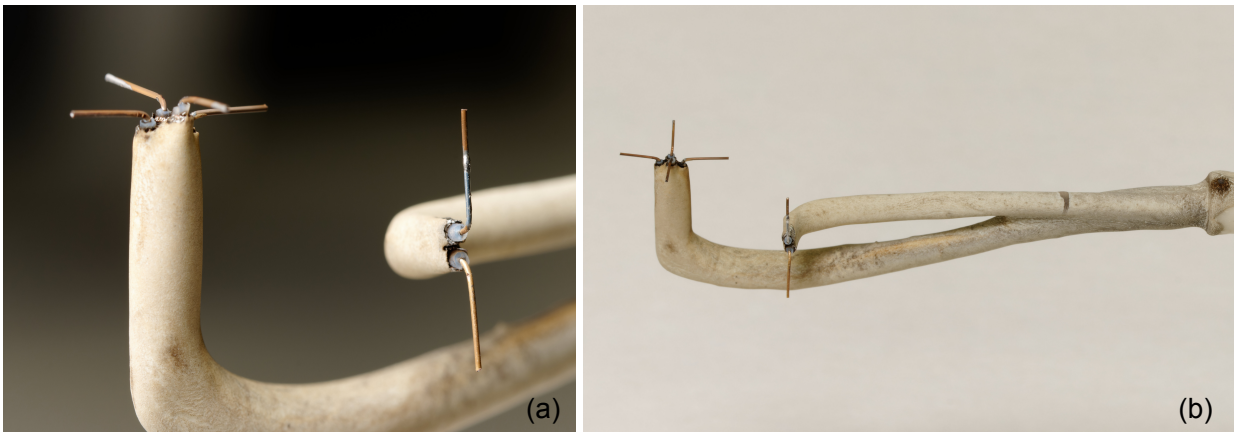

Figure 2.4: (a) A picture of the dipole probe tips (b) A zoomed-out view of the dipole probe assembly.

analyzer (VNA) and a Helmholtz coil. This setup provides us with a frequency response of the probe. In the 10-turn B-dots used for this work, the frequency response is linear up to 7-10MHz, and this is well above the frequency range necessary for the fast-wave sheath experiments. The Helmholtz coil setup also helps determine the "upright" orientation for the probe. This is done by producing a field in the y-direction and rotating the probe about the x-axis until the pick-up in the other two directions is minimized. Further details on these probes' design, construction, and calibration can be found in this work [33].

2.2.4 Electric Dipole Probes

Dipole probes are one the few reliable methods of measuring small time-varying electric fields in collisionless plasmas [34]. These probes consist of insulated conductors with small exposed whiskers for measuring time-varying electric fields. This is done by measuring the difference between the floating potential at the two tips of the conductors, where the floating potential is given by

$$\Phi_f = \Phi_p - (kT_e/e)\ln\left(T_e m_i / T_i m_e\right)^{1/2} \tag{2.6}$$

The difference in the floating potential Φ_p is representative of the difference in the plasma

potential and hence the electric field as long as there aren't any temperature gradients or electron tails. These probes are constructed using a high-frequency coaxial cable. They are made by stripping off the outer conductor and inner insulation, exposing typically 2-4 mm of the inner conductor, and bending the exposed tip at 90° angle. In this part of the construction, one has to be careful not to short the inner conductor to the outer shield while bending the whiskers. This is then done for three pairs of coax, and each set of three whiskers is oriented orthogonal to each other to measure the fields in all three directions. Finally, the signal from each pair of whiskers is subtracted using a differential amplifier and divided by the separation between the whiskers to get a signal proportional to the electric field.

2.3 Single-Strap ICRF Antenna and RF Amplifier

The antenna used in this work is a single-strap antenna that was previously designed and tested to launch fast waves in the LAPD. As shown in Fig. 2.5 a, the antenna consists of an approximately 28cm tall and 6cm wide antenna strap housed in an enclosure box. Fig. 2.5b shows a model cross-section of the antenna and enclosure box with one of the enclosure side walls being removed from the model. The particular enclosure box shown in this figure is a slotted copper box with a sheet of MACOR (machinable glass ceramic) epoxied to the inside of the slotted copper walls. The MACOR prevents a direct connection between the antenna strap and the plasma. This particular antenna design is analogous to other ICRH fast-wave antenna designs, including one or more antenna straps, an enclosure box, and a dielectric material [35, 36]. This particular antenna strap was used for all the results presented in this work. But the slotted copper enclosure walls were only used for a portion of the results. For the remaining experiments, the sidewalls of this enclosure box were replaced with different thickness MACOR material or a MACOR-copper stack material. Details on all the other enclosures used in this work will be provided in subsequent chapters, along with respective results.

Chapters 4 and 5 present results acquired during high-power experiments. The power system for the high-power RF antenna experiment is a complex system that consists of a charging power supply, a capacitor bank, a pulse modulator, an RF amplifier, and a matching network. The DC charging supply is able to output up to 37.5kW (1.5A at 25kV). This supply is used to charge a 624 F capacitor bank. A pulse modulator with a single ML-8618 vacuum tube is used to deliver power from the capacitor bank to the RF amplifier. The pulse modulator is connected to a water cooling system and has built-in failure modes to shut off the modulator in case the water cooling system malfunctions. The capacitor bank and pulse modulator are located in the power room, which is approximately 50-70 ft away from the amplifier, matching network, and antenna assembly. The output from the pulse modulator is connected to the RF amplifier using a high-voltage coax cable. In order to provide shielding, the high-voltage coax cable is grounded on both ends. The output from the RF amplifier is then connected to the RF antenna strap via a matching network that consists of a tunable capacitor and inductor. Details about each individual part of this system can be found in [37].

2.4 Data Acquisition

There are two main data acquisition systems for the LAPD named- the "housekeeper" and the "DAQ".

2.4.1 Housekeeping System

The role of the housekeeper is to monitor and maintain the health of the device. The housekeeper is stationed on a dedicated computer connected to several diagnostics, sensors, and controls. These diagnostics and sensors monitor the state of the machine and the plasma, including- neutral gas pressures from the RGA, magnetic coil currents, magnetic coil temperatures, interferometer time traces, cathode heater parameters, discharge current,

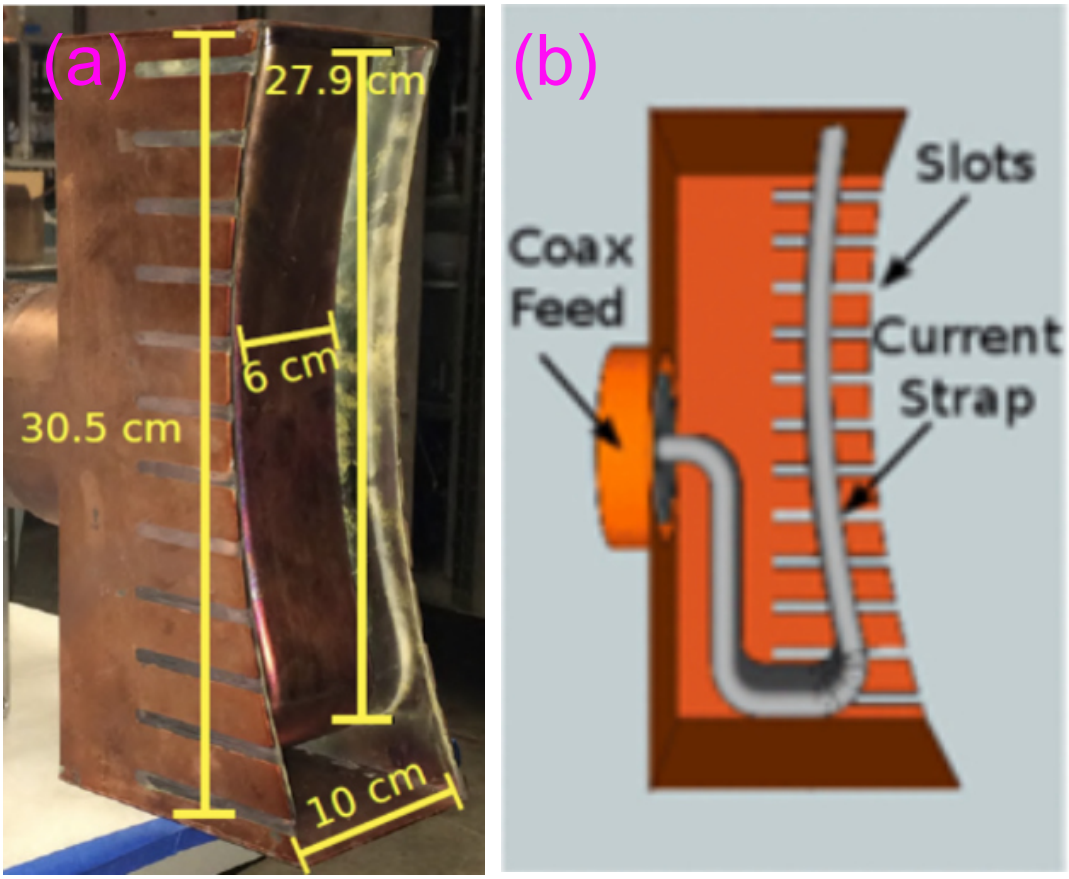

Figure 2.5: (a) A picture of the single-strap antenna with a slotted copper box enclosure. (b) A model of the antenna showing a cross-section of the antenna strap with one of the slotted sidewalls removed from the model.

and discharge voltage etc. One of the main purposes of the housekeeper is to safeguard the LAPD. There are a number of safety switches built into the system to shut off a different part of the machine to prevent damage in case of a malfunction.

2.4.2 DAQ System

The role of the DAQ is to control devices and acquire/record data per user-defined sequences of programmable tasks known as the "data sequence." During an experiment, several "data runs" are performed using a different set of probes, probe drives, additional devices, and data acquisition parameters. The data is digitized using 4- SIS3302 8-channel digitizers with 16-bit resolution and a sampling rate of up to 100MHz. This provides a total of 32 channels where diagnostic data can be digitized in parallel. Each of the four digitizer boards can be independently triggered at different times during the plasma discharge and set to acquire data at different sampling frequencies up to 100MHz. The digitizer input accepts an analog signal between $\pm 2.5V$. Signals from different diagnostics are often attenuated or amplified to make appropriate use of the data acquisition dynamic range. The DAQ system also sets the configuration of digitizer boards and channels. A new configuration can be set for each new data run, or a previously set configuration can be used for multiple data runs in an experiment. In addition to setting the digitizer parameters, the DAQ system is also responsible for controlling probe drives.

Diagnostic probes in the machine are often connected to a remote-controlled probe drive to move the probe tip through an array of desired locations. First, the probe drive is calibrated to the machine coordinate system by moving the probe tip to the machine center. Once the probe drive is calibrated, different "motion lists" can be defined within the DAQ system to dictate the movement of the probe during a data run. These motion lists often consist of either a line or a plane of points where data is being collected. The data sequence sets the order in which the probes are moved, where the probes are moved, and how many data shots per location are acquired.

All the measured data, machine state information, data description, and motion-list information is stored in a binary data format called Hierarchical Data Format version 5 (HDF5). These data files can be read using a number of different programming languages. Data for this work were all analyzed in Python. For Python, there is an interface available to the HDF5 binary data format known as the package h5py. H5py enables the process of manipulating data seamlessly and makes use of Numpy and Python metaphors, like a dictionary and Numpy array syntax.

CHAPTER 3

Theory

3.1 Sheath Physics

3.1.1 Debye Sheath

The basic idea of a Debye sheath at the edge of the plasma is dependent on the flow of the electrons and ions to the surface wall. The electron thermal speed significantly exceeds the ion thermal speed; therefore, electrons are lost faster to the wall. This leaves the overall plasma with a net positive charge with respect to the walls. In order to maintain ambipolarity in the bulk plasma, a sheath is formed at the plasma edge next to the plasma bounding surface. This sheath region has a high electrostatic field that repels the majority of free-streaming electrons and establishes ambipolarity of the plasma flow at the sheath boundary.

3.1.2 RF sheaths

The basics of Debye sheaths can be extended to understand and form a picture of RF sheaths. Consider a plasma volume between two biased electrodes that are being biased at $\pm V_0$ with respect to each other. Both electrons and ions attempt to escape at their respective thermal velocities at first, which are must faster for the electrons. As depicted in Fig. 3.1, the plasma develops an overall potential to contain the electrons and restore charge ambipolarity in response to the increasing charge imbalance. As a result, nearly all of the electrons are reflected at this potential, which must be higher than the applied voltage at either of the two electrodes. The requirement that the un-neutralized ion space charge

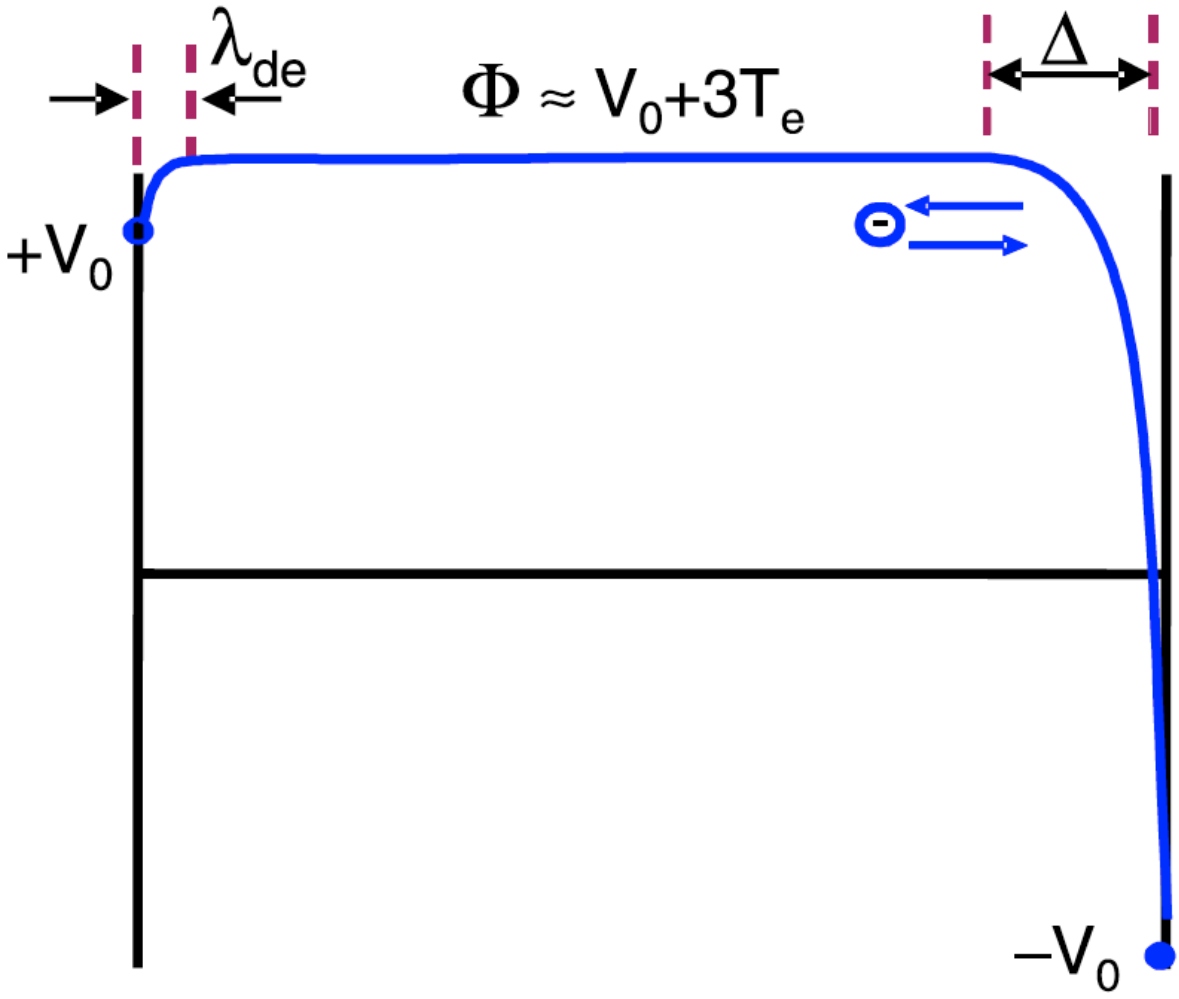

Figure 3.1: Basic sheath physics. The sheath forms to equalize electron and ion loss rates. The resulting potential enhances electron confinement by forming a potential barrier for electrons, i.e., the sheath of width. The same potential accelerates ions into the plates and causes the dissipation of sheath power. For the rf-sheath, the driving voltages ±V0 at each end oscillate in time, and the central potential must remain (3Te) above the maximum voltage at either end. Figure form [7].

in the sheath layer be adequate to give rise to the necessary potential drop determines the sheath width, $\Delta\ \lambda_d(eV_0/T_e)^{3/4}$ at each end. Here, the electron temperature is Te, the applied voltage is V_0, the proton charge is e, and the Debye length is λ_d [7]. This sheath reflects electrons and accelerates ions into the biased plates, resulting in a fast ion distribution that can exacerbate physical sputtering.

The fundamentals of sheath physics above lead into an ICRF sheath [10–15], where each of the electrodes is now subjected to an oscillating voltage. Electrons escape with the highest applied voltage from the end by exiting alternately from one end and the other. An oscillating parallel electron current results from this phenomenon. The applied voltage at either end is always higher than the central voltage of the plasma, which oscillates up and down at twice the applied frequency. Overall, the applied voltage ends up being rectified by the plasma.

Butler and Kino present another qualitative picture of the DC sheath rectification [8]. Suppose an RF potential $V_i(t)$ is applied to an electrode in a plasma discharge. A plasma current flows in response to the instantaneous $V_i(t)$. The typical $I-V$ characteristics of the plasma determine the magnitude of the current flowing to the electrodes, as shown in Fig. 3.2. In the top panel of the figure, when $V_i(t)$ is positive, an electron current much greater than the available ion current flows to the wall. Therefore, during the positive portion of $V_i(t)$ each cycle, an excess electron current would flow to the wall. Since the net DC current to the wall must be zero, V_i can only become slightly positive at its maximum value. It must assume a peak negative value that is a sizable portion of the peak-to-peak amplitude of the applied RF voltage. As depicted in the bottom panel of Fig. 3.2, in order to maintain ambipolarity, the plasma develops a DC rectification, and the electron and ion currents are balanced during each cycle.

3.1.3 Sheath Mitigation Model

Sheath control by insulating limiters has been explored by Majeski, et al. [38] and by Myra, et al. [9, 39]. The model presented in the latter work treats the insulator and plasma sheath

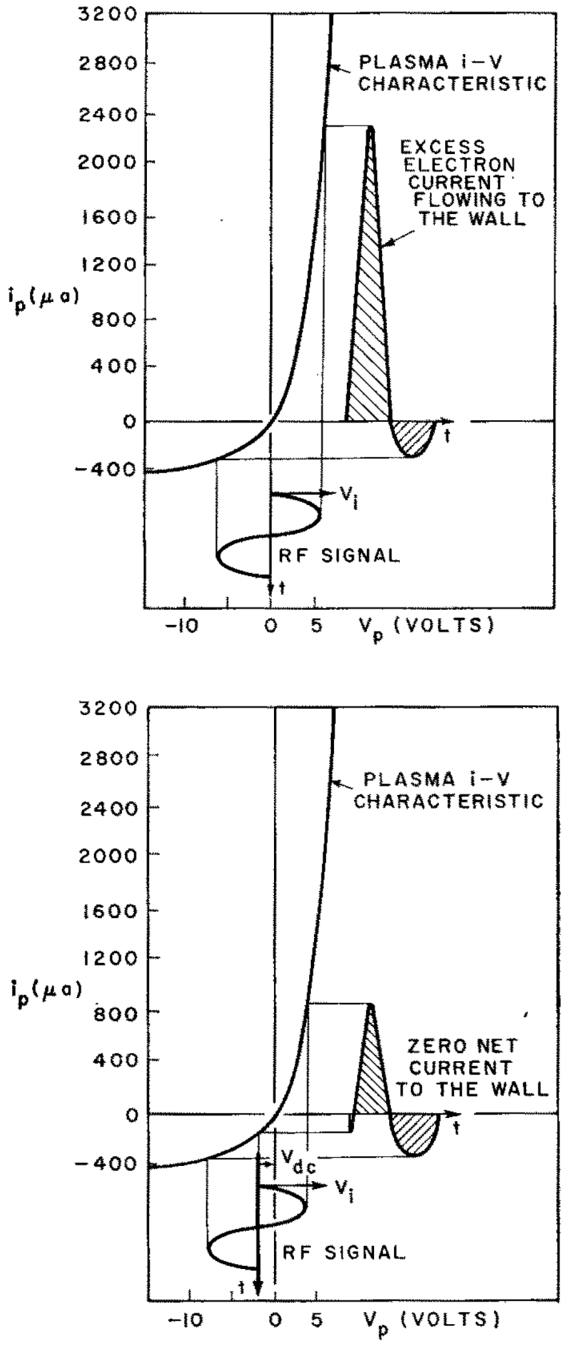

Figure 3.2: Pictorial representation of the mechanism by which a positive ion sheath is formed as a result of applying an RF voltage outside the plasma. Figure form [8].

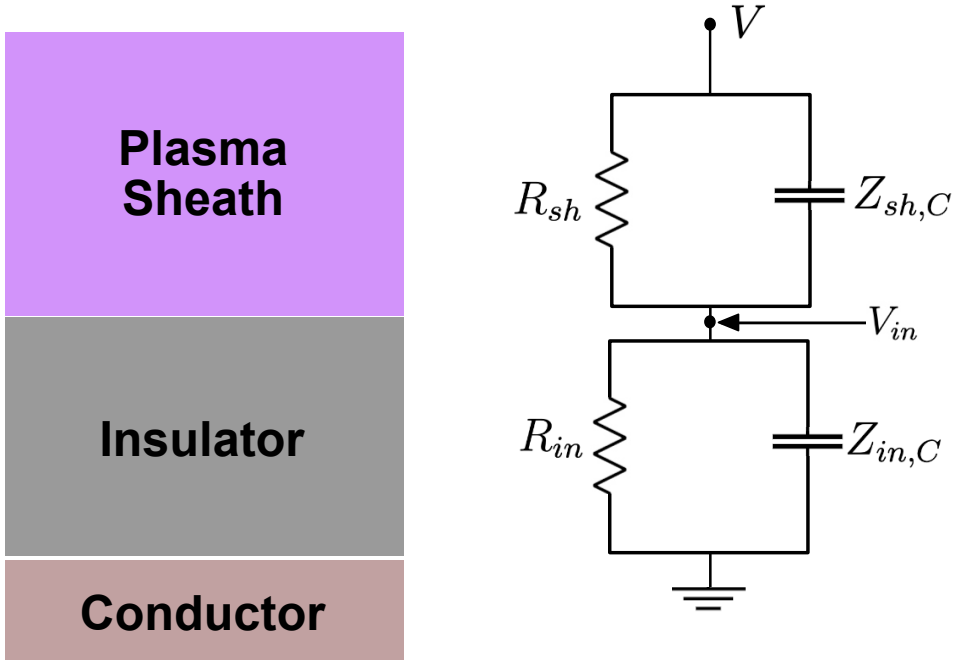

Figure 3.3: Basic circuit diagram for sheath and insulator calculations. This figure was reproduced from [9].

as two electrical elements in series with each other. The insulator and the plasma are individually represented as parallel resistance and capacitance in the model, with those individual representations in series.

As shown in Fig. 3.3, the sheath resistance and capacitance are represented by R_{sh} and $Z_{C,sh}$, respectively. Similarly, R_{in} and Z_{Cin} represent the insulator resistance and capacitance. The voltage drop across the insulator and plasma sheath in series is defined as V, and the voltage drop across the insulator is defined as V_{in}. Therefore, $V_{sh} = V - V_{in}$ gives the voltage drop across the plasma sheath. The degree of sheath mitigation is given by the following quantity-

$$\frac{V_{sh}}{V_{sh} + V_{in}} = \frac{Z_{sh}}{Z_{sh} + Z_{in}} \tag{3.1}$$

Depending on the RF voltage, plasma parameters, and insulator parameters, one can determine the potential drop across the plasma sheath versus the potential drop across the

insulator. The capacitive impedance of the sheath is given by-

$$|Z_{sh,C}| = \frac{\Delta}{\epsilon_0 \omega A}, \tag{3.2}$$

where the sheath width $\Delta = \lambda_D (eV_{sh}/T)^{3/4}$, λ_D is the Debye length, $\lambda_D = (T/4\pi n)ee^2)^{1/2}$, T is the electron temperature, n_e is the electron density, and e is the electron charge. The sheath resistance can be expressed as

$$R_{sh} = \frac{V_{sh}^2}{2P_{sh}} \tag{3.3}$$

where P_{sh} is the power dissipated by the ions accelerated in the sheath and is given by

$$P_{sh} = \frac{Anc_s Th(\xi)\xi I_1(\xi)}{I_0(\xi)}. \tag{3.4}$$

In the expression for P_{sh}, c_s is the sounds speed, $\xi = eV_{sh}/T$, I_0 and I_1 are Bessel functions and $h(\xi) = (0.5 + 0.3\xi)/(1 + \xi)$. The insulator resistance is given by-

$$R_{in} = \eta d/A \tag{3.5}$$

where η is the effective ac volume resistivity, d is the insulator thickness, and A is the surface area of the insulator. The capacitive impedance of the insulator is given by-

$$|Z_{in,C}| = \frac{d}{\epsilon \omega A} \tag{3.6}$$

where ϵ is the dielectric constant of the insulator and ω is the RF frequency. For sheath control, the goal is to minimize the potential drop across the plasma sheath by maximizing the potential drop across the insulator.

3.2 Plasma Waves

This section will present a derivation of the cold plasma dispersion and the slow wave and fast wave dispersion relations.

3.2.1 Cold Plasma Dielectric Tensor

In the cold plasma approximation, we make several simplifying assumptions. These include ignoring the motion of charged particles due to the particles' thermal energy and omitting the effect of collisions. Additionally, we assume the plasma to be homogeneous and quasineutral; the background plasma is assumed to have $\mathbf{B} = \mathbf{B_0}$ and $\mathbf{E_0} = \mathbf{0}$.

Starting with the single particle equation, Faraday's law, and Ampere's law-

$$m_s \frac{\partial \mathbf{v_s}}{\partial t} = q_s(\mathbf{E_1} + \mathbf{v_s} \times \mathbf{B_0}) \tag{3.7}$$

$$\nabla \times \mathbf{E_1} = -\frac{\partial \mathbf{B_1}}{\partial t} \tag{3.8}$$

$$\frac{1}{\mu_0}(\nabla \times \mathbf{B_1}) = \epsilon_0 \frac{\partial \mathbf{E_1}}{\partial t} + \mathbf{j_1} \tag{3.9}$$

Here the relationship between the first-order current and the first-order wave electric field $\mathbf{E_1}$ is through a conductivity tensor as follows-

$$\mathbf{j_1} = \sigma \cdot \mathbf{E_1} = \sum_s q_s n_s v_s \tag{3.10}$$

Note that the conductivity σ represents a tensor quantity. Additionally, we assume that the electric and magnetic fields vary as $exp[i(k_x x + k_z z - \omega t]$. Where k_x and k_z are constants that are not dependent on position and ω is also a constant that does not vary in time.

Then taking the curl of both sides of Faraday's law-

$$\nabla \times (\nabla \times \mathbf{E}) = \nabla \times (-\frac{\partial \mathbf{B}}{\partial t}) \tag{3.11}$$

and the fact that-

$$\nabla \times (\frac{\partial \mathbf{B}}{\partial t}) = -\frac{\partial}{\partial t}(\nabla \times \mathbf{B}) \tag{3.12}$$

we end up with-

$$\nabla \times (\nabla \times \mathbf{E}) = -\mu_0 \epsilon_0 \frac{\partial^2 \mathbf{E}}{\partial t^2} \tag{3.13}$$

Then using the assumed form of the electric and magnetic field, we can rewrite the above equation as,

$$\mathbf{k} \times \mathbf{k} \times \mathbf{E} + k_0^2 \varepsilon \cdot \mathbf{E} = 0 \tag{3.14}$$

where ε is given by-

$$\varepsilon = \begin{bmatrix} 1 - \sum_s \frac{\omega_{ps}^2}{\omega^2 - \Omega_s^2} & -i \sum_s \frac{\Omega_s}{\omega} \frac{\omega_{ps}^2}{\omega^2 - \Omega_s^2} & 0 \\ i \sum_s \frac{\Omega_s}{\omega} \frac{\omega_{ps}^2}{\omega^2 - \Omega_s^2} & 1 - \sum_s \frac{\omega_{ps}^2}{\omega^2 - \Omega_s^2} & 0 \\ 0 & 0 & 1 - \sum_s \frac{\omega_{ps}^2}{\omega^2} \end{bmatrix} \tag{3.15}$$

In the dielectric tensor above, we've made use of the following definitions-

$$\omega_{ps}^2 = \frac{q_j^2 n_s}{\varepsilon_0 m_s} \tag{3.16}$$

$$\Omega_s = \frac{q_j B_0}{m_s} \tag{3.17}$$

The dielectric tensor above is often written using Stix notation as-

$$\varepsilon = \begin{bmatrix} S & -iD & 0 \\ iD & S & 0 \\ 0 & 0 & P \end{bmatrix} \tag{3.18}$$

where the parameters S, P, and D are defined as-

$$S = \tfrac{1}{2}(R+L), \quad D = \tfrac{1}{2}(R-L), \tag{3.19}$$

$$R \equiv 1 - \sum_s \frac{\omega_{ps}^2}{\omega\left(\omega + \Omega_s\right)} \tag{3.20}$$

$$L \equiv 1 - \sum_s \frac{\omega_{ps}^2}{\omega\left(\omega - \Omega_s\right)} \tag{3.21}$$

$$P \equiv 1 - \sum_s \frac{\omega_{ps}^2}{\omega^2}. \tag{3.22}$$

3.2.2 Fast Wave and Slow Wave Dispersion Relations

Using the Stix formulation for the dielectric tensor, defining $k_\parallel$ as the component of the wave vector parallel to the background magnetic field, defining $k_\perp$ as the component of the wave vector perpendicular to the background magnetic field, and introducing $k_0 = \omega/c$, we can rewrite equation 3.14 as-

$$\begin{pmatrix} k_0^2 S - k_\parallel^2 & -\mathrm{i}k_0^2 D & k_\perp k_\parallel \\ \mathrm{i}k_0^2 D & k_0^2 S - k_\parallel^2 - k_\perp^2 & 0 \\ k_\perp k_\parallel & 0 & k_0^2 P - k_\perp^2 \end{pmatrix} \begin{pmatrix} E_x \\ E_y \\ E_z \end{pmatrix} = 0 \tag{3.23}$$

The wave equation above has non-trivial solutions when the determinant of the 3×3

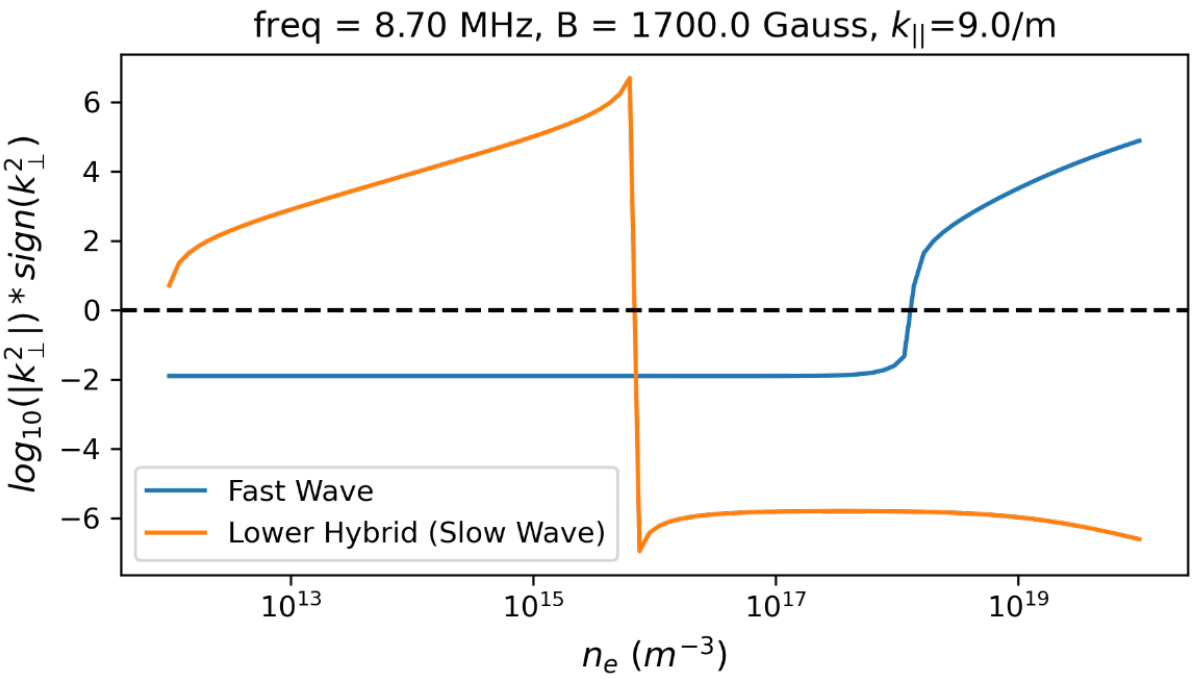

Figure 3.4: Dispersion Plot: $k_\perp^2$ as a function of plasma density for typical LAPD parameters. The wave is evanescent when $k_\perp^2$ is negative, below y =0. The slow wave is evanescent for densities higher than the lower-hybrid-resonance. which is approximately at $n \approx 6 \times 10^{15}$. Similarly, the fast wave is evanescent below the fast wave cutoff, approximately at $n \approx 1{\times}10^{18}$ for the plotted LAPD parameters.

matrix is zero. This gives us a fourth-order equation for $k_\perp$. Taking into the account the high ion-to-electron mass ratio, we approximate $|P| \approx \left|\omega_{pe}^2/\omega^2\right| \gg |L|$ and $|R|$. Exploiting this approximation, we arrive at the following solutions for $k_\perp$-

$$k_{\perp,FW}^2 = \frac{\left[k_0^2 R - k_\parallel^2\right]\left[k_0^2 L - k_\parallel^2\right]}{k_0^2 S - k_\parallel^2} \tag{3.24}$$

$$k_{\perp,SW}^2 = \frac{P}{S}\left[k_0^2 S - k_\parallel^2\right] \tag{3.25}$$

The two roots are labeled with subscripts FW and SW, indicating the fast wave and slow wave dispersions, respectively, where the phase velocity, ω/k is larger for the fast wave and $k^2_{\perp,FW} < k^2_{\perp,SW}$. Equation 3.24, the fast wave dispersion relation has a cutoff at $k_0^2 L = k_\parallel^2$ and $k_0^2 R = k_\parallel^2$. Equation 3.25, the slow wave dispersion relation has cutoffs at $P = 0$ and $k_0^2 S = k_\parallel^2$, and a resonance at $S = 0$. The $S = 0$ resonance is also known as the lower-hybrid-resonance. For typical LAPD parameters, these solutions have been plotted in Fig. 3.4. In this figure, the slow wave is evanescent for densities higher than the lower-hybrid-resonance. which is approximately at $n \approx 6 \times 10^{15}$. Similarly, the fast wave is evanescent below the fast wave cutoff, approximately at $n \approx 1 \times 10^{18}$ for the plotted LAPD parameters.

CHAPTER 4

Reduction in RF sheath rectification with insulating antenna enclosure walls

In this chapter, we present results from experiments performed on the Large Plasma Device (LAPD) to explore the effects of using electrically-insulating antenna enclosures on RF-rectified sheaths. Three different enclosure side-wall materials were used: copper, MACOR (electrically insulating), and MACOR over copper. In the case of the MACOR-copper side walls, the non-conductive MACOR material was exposed to the bulk plasma, but a layer of copper was added below to allow for image currents to flow. All three experiments had similar plasma density, temperature, and background magnetic field. In the case of the copper enclosure, RF rectified potentials, many times the local electron temperature, and associated formation of convective cells were observed and reported [1]. RF rectification was significantly reduced in the experiments with MACOR and MACOR-copper enclosures. Additionally, these latter two experiments showed no evidence of convective cell formation. Although the results from the MACOR experiment are reminiscent of the results obtained in ASDEX-U with a 3-strap antenna optimized to reduce image currents on the antenna limiters [2], the MACOR-copper experiment seems to suggest that insulating plasma-facing materials have at least an equally strong impact on reducing potential rectification.

4.0.1 Motivation

Plasma potential structures and convective cells resulting from RF rectification were directly measured in detail near an ICRF antenna in the Large Plasma Device (LAPD), part of the

Basic Plasma Science Facility at UCLA [1]. This chapter will compare the results presented in that paper with results from two new experiments performed on the LAPD. The motivation for the two new experiments is strongly tied to understanding the cause of RF sheath potential rectification and improving ICRH efficiency in current and future fusion devices. Experiments on ASDEX Upgrade and simulations suggest that minimizing image currents in antenna enclosure walls also minimizes parallel electric fields at the antenna's edge, reducing DC sheath rectification and impurities in the plasma [40]. The first RF sheath experiment at the LAPD was carried out with a single-strap RF antenna housed in a copper enclosure. A plasma potential rectification of over 70 volts was documented, much larger than the local electron temperature. In order to explore the role of image currents in antenna enclosure walls, a second experiment was carried out where copper side walls were replaced with insulating MACOR side walls. This change proved effective in eliminating large potential rectifications. These results suggest that image currents in the enclosure side walls or a DC electrical connection between the side walls and the bulk plasma may be responsible for the DC potential rectification.

To investigate this further, a third experiment was carried out with double-layered antenna walls consisting of a layer of insulating MACOR on the outside in contact with the bulk plasma and a layer of copper on the inside, closest to the antenna strap. The third experiment aimed to test whether potential rectification persists if image currents are allowed to exist in the inner copper walls. At the same time, the bulk plasma is DC electrically isolated from the enclosure walls. Majeski's work [38] suggests that adding insulators on and around antenna structures can help eliminate RF sheaths. A model for this mechanism is laid out in D'Ippolito, and Myra's work [9, 41]. This model treats the insulator and plasma sheath to be two circuit elements in series with each other, effectively creating a voltage divider. The insulator and the plasma sheath are considered to have resistive and capacitive components in parallel. The model suggests sheath control by insulating limiters can be achieved by minimizing the potential drop across the plasma sheath and maximizing the

potential drop across the insulator.

ICRH schemes aim to couple the maximum power into the core plasma while minimizing the deleterious effects caused by nonlinear effects such as RF sheaths and convective cells. Therefore, the strategy to compare the three antenna enclosures was to do the experiments in plasmas with similar plasma density, temperature, and background field, and with similar fast wave power coupled to the core of the plasmas, and then evaluate the relative impact of nonlinear near-field effects.

The remainder of this chapter is organized as follows. Section 4.0.2 describes the machine parameters and its diagnostics and outlines the details of the different ICRF antenna configurations. Section 4.1 juxtaposes the results obtained with the three antenna enclosures in terms of power coupled to the plasma, strength of the RF sheaths, and convective cells near the antenna. Section 5.4 discusses the results in detail.

4.0.2 Experimental Setup and Diagnostics

This chapter will compare results from three experiments conducted on the LAPD. A schematic of the machine and the setup for this experiment are shown in Fig. 4.1. For the copper and MACOR experiments, the background plasma column is generated by a barium oxide (BaO) cathode source. After the MACOR experiment, the large BaO source was upgraded to a Lanthanum Hexaboride (LaB_6) source. Both of the larger sources were operated to generate a background plasma of density, $n \approx 10^{12}$ cm^{-3}, such that the plasma diameter was approximately 20cm in each experiment. The plasma discharge operates at a 0.67 Hz to 1 Hz repetition rate, with the plasma discharge lasting around 10-12ms, with typically a few hundred kiloWatt discharge power. Experiments were performed in helium plasmas in a background magnetic field of 1 kG. More details about the LAPD or the generation mechanisms of the plasma can be found in the LAPD upgrade RSI paper [42].

In each of the three experiments described in this chapter, a single-strap, high-power

(100kW) RF (2.4MHz) antenna was used to launch fast waves into the dense core of the magnetized helium plasma. The core density of the plasma was $n_e \approx 5 \times 10^{12}$ cm^{-3} to 8×10^{12} cm^{-3} during each experiment. No Faraday screens were used on the front face of the antenna enclosure for all three experiments. The main difference in these experiments was the material used for the antenna enclosure sidewalls: copper, MACOR, and a MACOR-copper stack. An image of these antennae and enclosure wall assemblies is shown in Fig. 4.2(a-c). The same antenna strap was used with a different enclosure in each case. For the first case, the entire enclosure was made of copper and had slots in the sidewalls to allow the magnetic flux to flow out of the antenna box. Additionally, MACOR sheets were epoxied to the interior of the box to cover the slots and prevent direct contact between the plasma and the current strap. MACOR was used because it is electrically insulating and has low thermal conductivity. For the second experiment, the side walls of the enclosure were replaced with single sheets of MACOR. The third experiment used a MACOR-copper stack for the antenna sidewalls. As shown in Fig. 4.2(c), the inner layer was slotted copper, and the outer layer was solid MACOR sheets. Experiments 1, 2, and 3 aimed to determine the impact of a DC electrical connection between the plasma and the antenna enclosure sidewalls and the impact of image currents in the sidewalls on RF sheath rectification in the plasma. Experiment 2 eliminates both the DC electrical connection and the image currents. Experiment 3 allows for image currents to persist in the side walls but prevents a DC electrical connection between the bulk plasma and the side walls. In each experiment, the antenna was inserted into the plasma such that at y=0, the edge of the sidewall was at x = -12 cm. As shown in the top view schematic in Fig. 4.1, there were two limiters placed on either side of the antenna to prevent a connection along magnetic field lines between the antenna enclosure and the biased plasma source cathode-anode systems.

All three experiments measured plasma and wave characteristics using emissive, magnetic pickup, and Langmuir probes. Probes were inserted through "ball valve" feed-throughs that allow 3D motion of the probe tip in the vacuum vessel [43] and were mounted onto a

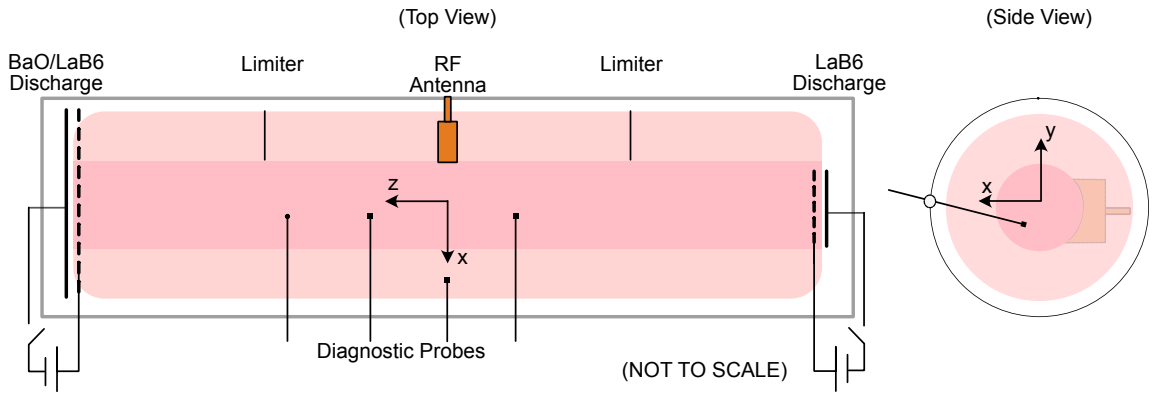

Figure 4.1: Top View of experimental setup on left and side view on the right, not to scale.

.

computer-controlled motorized drive to control the probe position for data acquisition. The data presented in this work was taken along different xy planes in the machine. As shown in Fig.4.1, the LAPD coordinate system is oriented with the z-axis parallel to the axis of the machine and to the background magnetic field.

10-turn differential magnetic field probes (also known as B-dot probes) were used to measure magnetic field fluctuations and characterize wave fields launched by the fast wave antenna [33]. Langmuir probes were used to characterize the plasma electron temperature and density. An emissive probe was used to measure the spatial plasma potential profiles [44]. Though tungsten is commonly used for the construction of emissive probe tips, in this particular case, due to the high-density plasma, the probe tips were made of sintered pieces of LaB_6 [44]. The advantage of using LaB_6 over tungsten is that LaB_6 is mechanically stable at temperatures necessary for adequate emission.

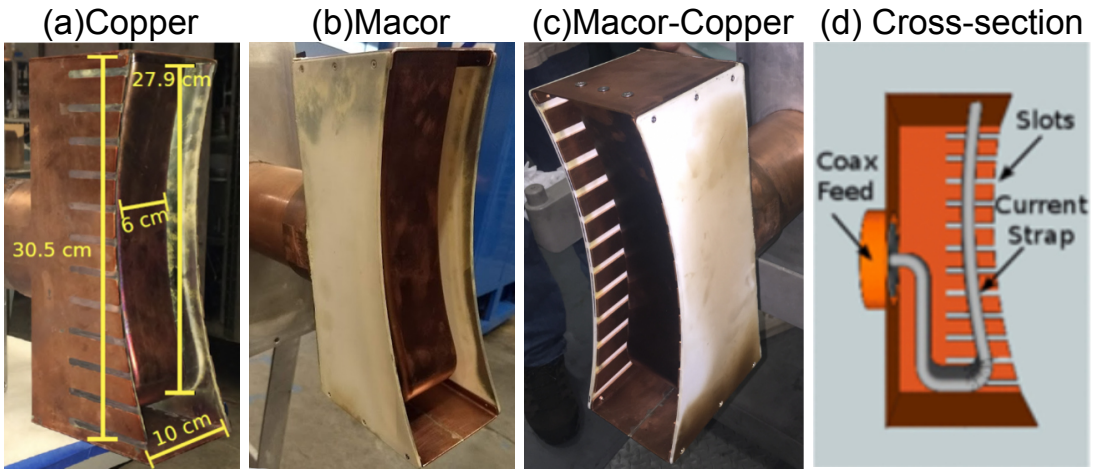

Figure 4.2: Antennas used in the three experiments (a)Antenna strap with slotted copper side walls. (b) Antenna strap with electrically insulating MACOR side walls. (c)Antenna strap with MACOR-copper side walls with MACOR exposed to the bulk plasma and slotted copper walls placed on the inside. (d)A cross-section schematic of the antenna showing the shape of the strap and the slots added to the copper side walls.

4.1 Results

4.1.1 Plasma conditions and measured wave amplitudes

Each experiment was carried out during the combined plasma discharge for the two sources at either end of the machine. The average core plasma densities during the three experiments ranged from $5 \times 10^{12}\text{cm}^{-3}$ to $8 \times 10^{12}\text{cm}^{-3}$. The core plasma electron temperature was measured between 8-14 eV for the three experiments. Although there were some variations in the core temperature during each experiment, in the region of interest, between the limiters and the antenna, the temperature was much colder, in the range of a few eV for all three experiments. The core temperature in the MACOR-copper stack experiment is greater than the first two experiments, which can compromise the emissive probe's ability to accurately track the plasma potential if it is not able to obtain a high enough emission current. However, this work is focused on comparing plasma potential measurements between the antenna and

the limiters, where the electron temperature is lower, and the emissive probe is able to emit adequately.

The single-strap RF antenna was powered at 2.38MHz ($6.2f_{ci}$), 2.35MHz ($6.1f_{ci}$), and 2.31MHz ($6.02f_{ci}$) for the copper, MACOR, and MACOR-copper experiments respectively. The RF antenna launched fast waves into the dense core of the plasma in each experiment. In order to draw a reasonable comparison between the three experiments, B-dot probes were used to measure and compare the coupled fast wave amplitudes. Fig. 4.3 shows an (x, y) plane contour plot with each experiment's perpendicular magnetic wave amplitude. The maximum wave amplitudes for all three experiments were approximately 4-6 Gauss. The variation in the topology of the wave magnitude can be explained by the difference in density profiles in each of the three experiments. Comparing the magnitude of the perpendicular magnetic wave in Fig. 4.3 for each of the three experiments to the ion saturation profiles in Fig. 4.7(a-c) from each experiment, we can see that the wave amplitude is peaked in the same location as the peak in the Ion saturation signal, the proxy for plasma density. This work aims to show that potential rectification can be reduced while launching fast waves of comparable magnitude in the core.

4.1.2 Experimental Fast Wave Mode Observation

In addition to comparing the wave amplitudes, the wave mode structure was also studied in these experiments. Fig. 4.4 shows m=1, fast wave mode propagation at three times during the antenna pulse within a single RF period. B_z component of the wave is shown in the color plot. Additionally, the vector plot overlay shows the B_x and B_y components of the wave.

4.1.3 Simulating Fast Wave Mode using Petra-m

Petra-m (Physics Equation Translator for MFEM) is an MFEM based finite element simulation code. Piscope is the graphical user interface used to set up the geometry and all the

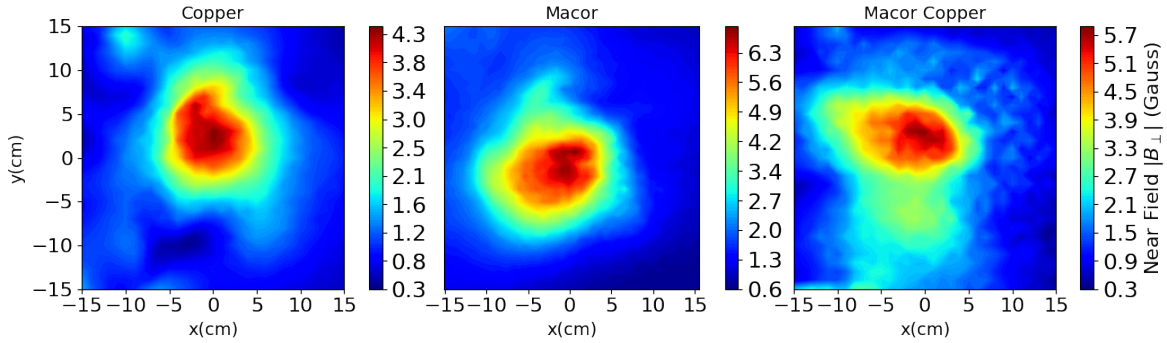

Figure 4.3: Magnitude of perpendicular magnetic wave amplitude for each experiment.(a)Copper Enclosure: Bdot probe was located at z = -64 cm (b)MACOR Enclosure: Bdot probe was located at z = -32 cm (c) MACOR and Copper stacked enclosure: Bdot probe was located at z = -64 cm. For comparison, the parallel wavelength of the wave is on the order of 90 cm.

parameter of the simulation. Piscope allows the user to import 3D CAD models to build a full geometry, or some geometry components can be imported while the rest of the geometry can be built in the piscope. The Petra-m simulations were run in a full-size LAPD model with the single-strap RF antenna to compare the fast wave mode experimental results presented in the previous section. The results from these simulations are shown in the bottom row of Fig. 4.4. Panels d, e, and f show the mode propagation at three different times during a single RF cycle. Comparing the Bz component shown in panels a, b, and c, we observe that the mode structure of the experimental results and the simulation agree with each other.

4.1.4 Potential Rectification

To better illustrate the rectification in time, Fig. 4.6 shows the time traces of the antenna current and the plasma potential at the location (-15, -11) cm, which is the location of peak rectified potential in the copper sidewall case. As seen from the plasma potential time trace, as soon as the RF antenna turns on, the potential is DC rectified, but only in the copper case does the potential increase by a large amount. Although this point in the (x, y) plane is not

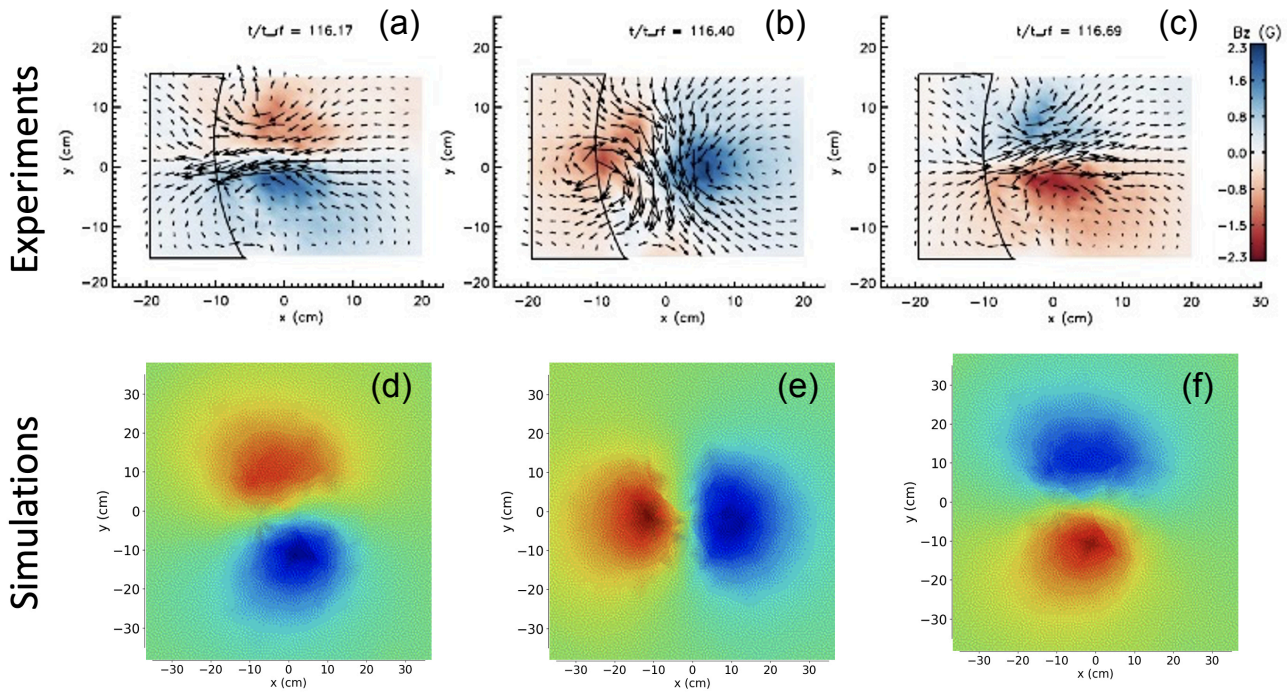

Figure 4.4: (a-c)Fast wave mode propagation at three different times during a single RF cycle. Bz is shown in the color plot, while the Bx and By components are shown in the overlayed vector plot. (d-f)Simulation results of fast wave mode propagating at three different times during a single RF cycle. The color plot shows the Bz component of the simulated fields.

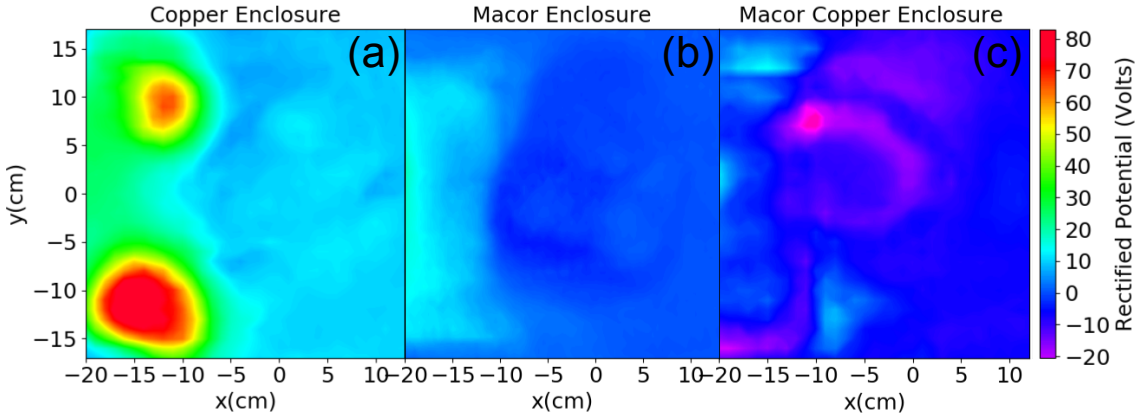

Figure 4.5: Plasma Potential Rectification profiles for each of the three experiments. (a)Copper enclosure data was taken at z = 64 cm. (b)MACOR enclosure data was taken at z = 1.5 m. (c)MACOR-copper stacked enclosure data was taken at z = 1.5 m.

necessarily the point of absolute maximum potential for the MACOR and MACOR-copper case, the same consistent location was chosen for comparison to illustrate that the expected rectification at the bend of the antenna is significantly reduced due to the presence of insulating MACOR sidewalls. Additionally, for MACOR and MACOR-copper experiments, the points of maximum positive rectified potential occurred near the x = -20 region, where the back side of the enclosure and copper coax are located. It's important to note that the back side of the enclosure and coax in the second two experiments consisted of copper exposed to the plasma. In conclusion, the comparison between the copper, MACOR, and MACOR-copper stack experiments show that the near-field RF rectification is significantly reduced while coupling the same amount of fast wave power to the core plasma by replacing conducting copper walls with insulating MACOR walls and MACOR-copper stacked walls. This idea is further supported by comparing the density modifications in each of the experiments during the RF pulse.

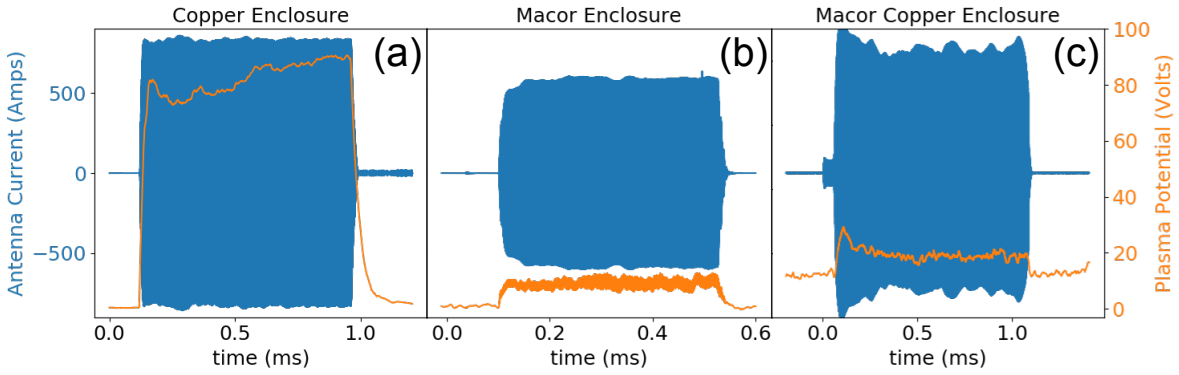

Figure 4.6: A single-time trace of antenna current and plasma potential at (x, y) = (-15, -11) cm for each experiment. RF fluctuations have been filtered out from the plasma potential trace. (a)We observed a plasma potential rectification of about 80 Volts in the copper enclosure experiment. (b) In the MACOR enclosure experiment, we observed a plasma potential rectification of less than 10 volts. (c) In the MACOR-copper stacked enclosure experiment, we also observed a plasma potential rectification of fewer than 20 volts.

4.1.5 Convective flows and evolution of plasma density

In the copper experiments, the large RF rectified potential structures and associated cross-field electric fields led to strong convective cells that modified the plasma density in front of the antenna. In each of the three experiments ion saturation (I_{isat}) measurements were taken using a Langmuir probe. Since the electron temperature during the RF pulse only differs by a few tens of percent, and since I_{isat} scales as $n_e\sqrt{T_e}$, the significant changes in the I_{isat} measurements represent changes in plasma density during the RF pulse.

As seen in Fig. 4.5a, for the copper experiment, there are two obvious hot spots in the plasma potential along field lines that connect between the antenna side walls and the limiters. As a consequence of these areas of rectified potential, strong electric fields are present along the potential gradients ranging from a few hundred to 800 V/m. These electric fields and the background magnetic field results in E×B flows that form convective cells around the hots spots. These flows were previously documented and presented in the original PRL [1].

Fig. 4.7 shows each experiment's ion saturation current profiles in the xy plane. Panels a-c show the profiles before the RF pulse, panels d-f show the profiles during the RF pulse, and panels g-i show the normalized difference between RF OFF and RF On($\delta I_{isat}/I_{isat,max}$). The difference plots have been normalized by the largest value of ion saturation while RF is off for each respective experiment. Note that the difference images were all plotted using a common color scale to show the stark difference between copper vs. MACOR and copper-MACOR. For the case of copper side walls, there are significant differences in the density profiles between RF off(panel a) and RF on(panel d). In contrast to the copper experiment, the latter two experiments show no significant changes in the ion saturation due to the RF pulse. Additionally, in the copper experiment, probes were found to be coated in a layer of copper after the experimental run. This coating is likely a result of sputtering from the copper antenna structure. Unlike the copper experiment, the latter two experiments showed no obvious copper deposition on the probes, further supporting the lack of rectified sheaths and sputtering.

4.1.6 Power Scaling

To study the scaling of rectified potential as a function of antenna power, for all three experiments, emissive probe data was obtained for a number of different applied RF powers. The measurement location was chosen based on where the highest potential rectification occurred in the full (x, y) plane. For the copper experiment, the center of the plasma potential hot spot occurred near (-16,-12) cm. For the MACOR experiment, the measurement was taken at (-16,0), at the midplane of the antenna as there is little variation in rectified potential in the vertical direction. Lastly, for the MACOR-copper experiment, rectification was greatest near (-16,13) cm. Fig. 4.8 shows the rectified potential ($V_{p,ON} - V_{p,OFF}$) as a function of RMS antenna current for each of the three experiments at their respective y locations mentioned above. This figure illustrates the significant reduction in DC rectification between copper vs. MACOR and MACOR-copper stack antenna enclosures.

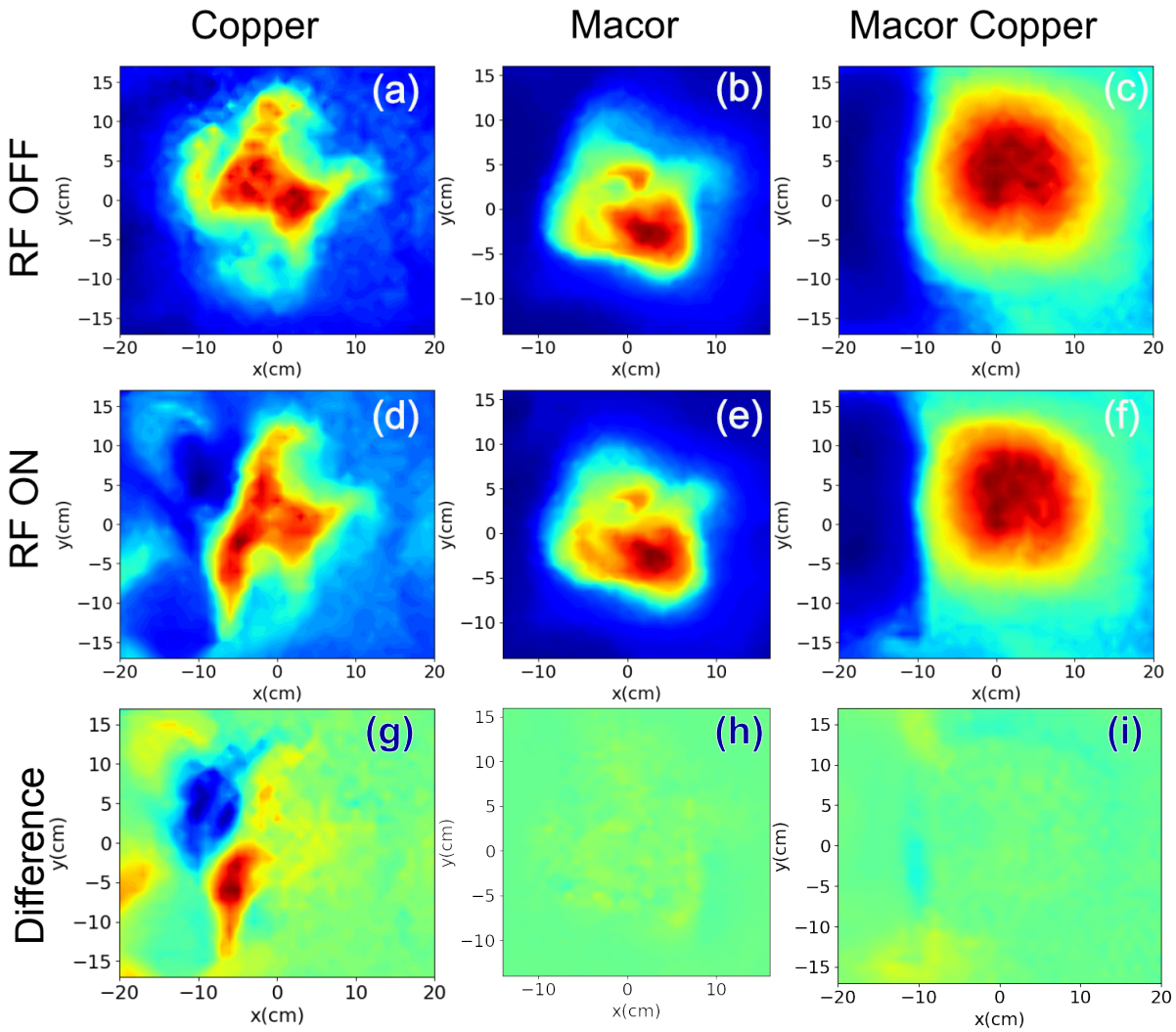

Figure 4.7: (a-c)Ion saturation profiles before RF pulse for each of the three experiments. (d-f)Ion saturation profiles during RF pulse for each of the three experiments. (g-i)Difference in ion saturation profiles(RF On - RF Off), normalized by the max ion saturation value during RF Off($\delta I_{isat}/I_{isat,max}$).

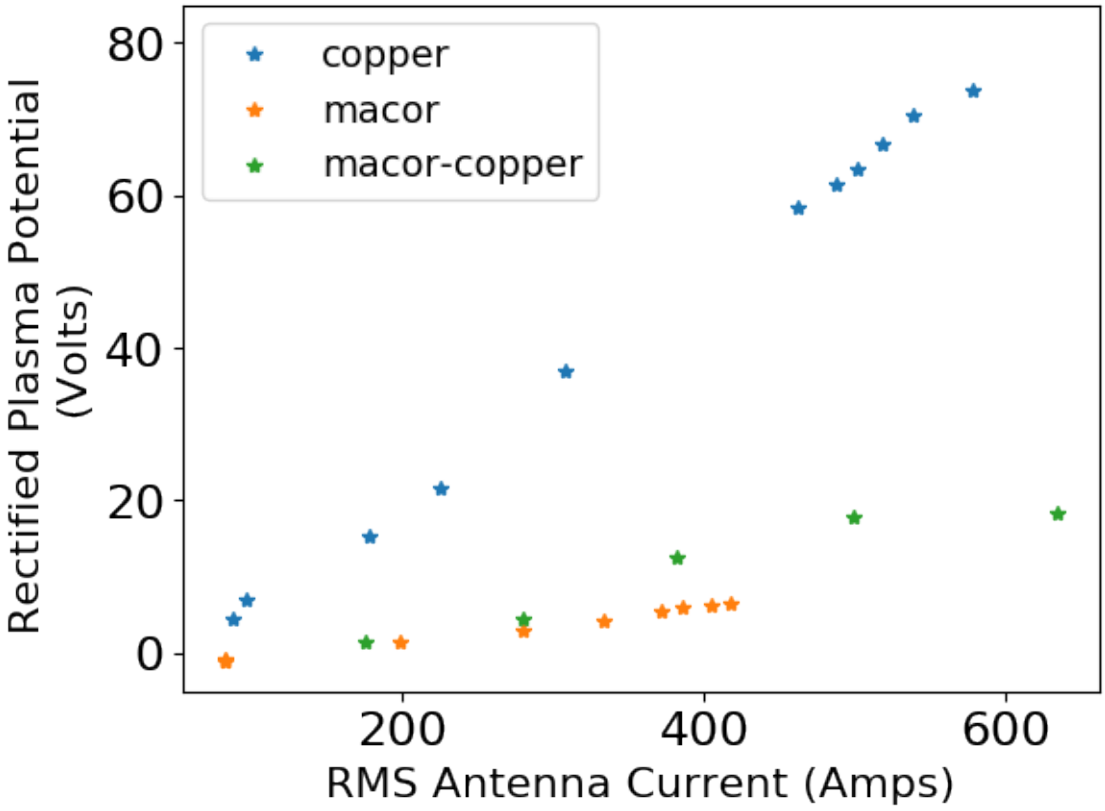

Figure 4.8: This plot shows rectified plasma potential as a function of antenna current for each of the three experiments. In each experiment, emissive probe data was recorded for a range of antenna currents near the area of greatest potential rectification. For each current setting, the rectified potential ($V_{p,ON} - V_{p,OFF}$) was calculated and plotted as a function of RMS antenna current.

4.2 Discussion

In this chapter, we have described three different experiments on the LAPD that use the same RF fast wave antenna in different enclosures. The three enclosures had sidewalls made of copper, MACOR, and MACOR-copper stack materials. In the results section, we have reported on the wave fields launched by the antenna in each experiment, the plasma potential profiles showing evidence of any RF rectification, and possible density modifications due to the RF pulse.

As seen in Fig. 4.3 the fast wave amplitudes in the core were very similar for all three experiments. For the copper experiment, plasma potential measurements show significant potential rectification along field lines in the SOL region, connecting the antenna walls to the grounded limiters. In contrast, for the MACOR and MACOR-copper stack experiments, while coupling similar wave power to the fast wave in the dense core, the results show a significant reduction of RF rectification. Comparing the plasma potential profiles in Fig. 4.5a, 4.5b, and 4.5c, it is clear that the notable RF rectification near locations (x,y): (-15,-11) cm and (-12,10) cm is appreciably reduced when the electrical connection between the sidewalls is broken via DC electrically insulating MACOR and MACOR-copper stack sidewalls. This result can play a key role in reducing unwanted effects such as convective cells and impurity generation that result from RF rectification during fast wave heating in a tokamak.

Although the regions of expected rectification hot spots from the copper experiment are mitigated, in the latter two experiments, there are still some regions of positive potential rectification towards the backside of the antenna enclosure near (-20,0) cm and the top of the enclosure near (-16,13) cm for the MACOR and MACOR-copper case respectively. The relative magnitude of rectification is greater in the MACOR-copper case, which could be attributed to the presence of image currents in the inner copper layers of the enclosure.

Sheath control by insulating limiters has been described in section 3.1.3. Depending

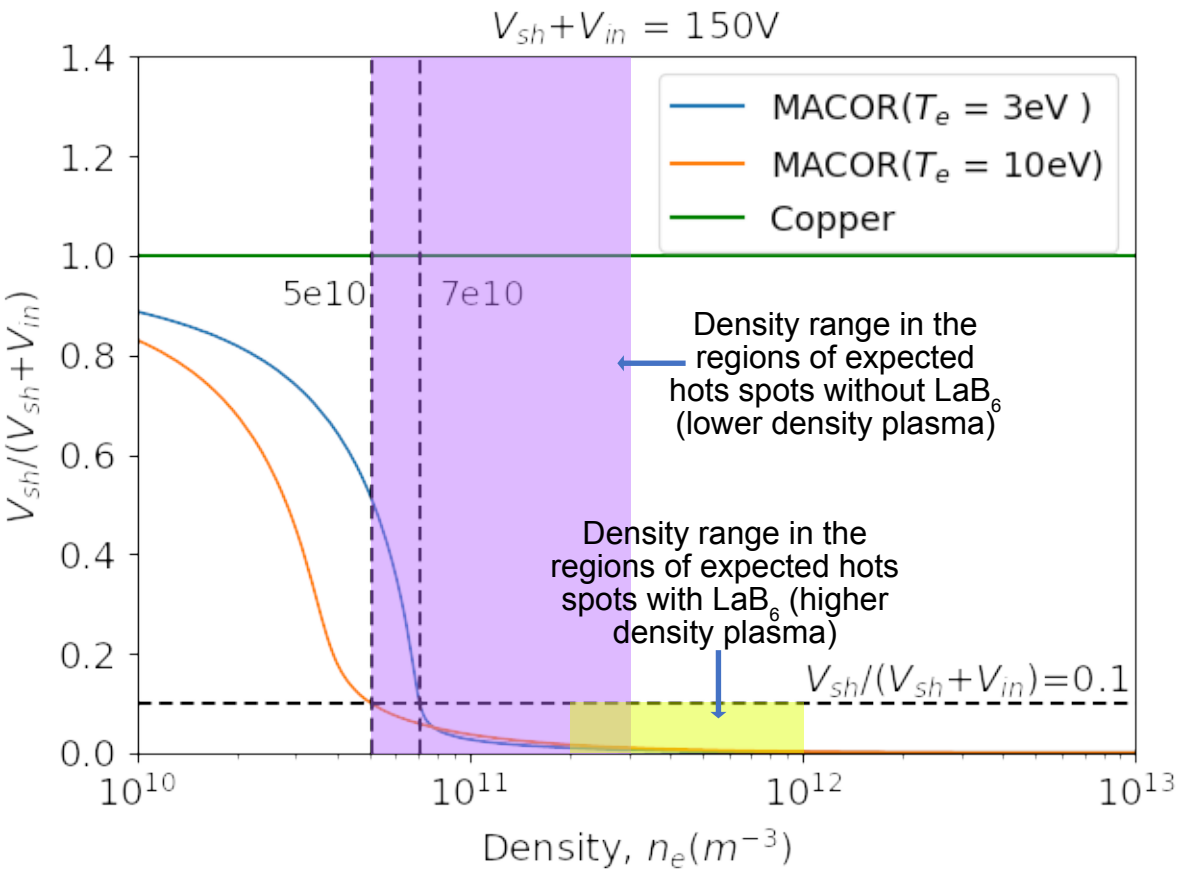

Figure 4.9: Predicted sheath control due to insulating side walls: $V_{sh}/(V_{sh} + V_{in})$ as a function of density for two different electron temperatures. The highlighted yellow region corresponds to the density range in the regions of expected potential rectification hot spots for the MACOR experiment with the LaB_6 source, which corresponds to a high-density plasma. In this region, the curves predict that the rectified sheath potential in the MACOR case should be well below 10% of the total potential drop across the insulator and plasma sheath. The highlighted purple region corresponds to the density range in the regions of expected potential rectification hot spots for the MACOR experiment without the LaB_6 source, which corresponds to a lower-density plasma. In a portion of this purple region, the curves predict that the rectified sheath potential in the MACOR case should be well above 10% of the total potential drop across the insulator and plasma sheath.

on the RF voltage, plasma parameters, and insulator parameters, one can determine the potential drop across the plasma sheath versus the potential drop across the insulator. For sheath control, the goal is to minimize the potential drop across the plasma sheath. Fig. 4.9 shows the model prediction for the ratio between the sheath potential and the total potential drop across the insulator and plasma sheath for parameters corresponding to the MACOR-copper experiment and the copper experiment. The plasma temperature is about 10 eV in the core and drops down to a few eV in the edge. Curves for both 3 eV and 10 eV are shown to demonstrate the effect of plasma temperature on this ratio. In the region of expected sheath rectification, the plasma density ranges between $2 \times 10^{11}\text{cm}^{-3}$ to $1 \times 10^{12}\text{cm}^{-3}$. This density range is highlighted in yellow in the figure and shows that the model predicts a plasma sheath drop that is well below 10% of the RF voltage. The model prediction is, therefore, consistent with the lack of rectified hots spots in the experimental results for the MACOR and MACOR-copper cases. During the MACOR experiment, an additional plane of plasma potential data was taken without the additional LaB_6 source operating (shown on the right end of the machine in Fig. 4.1). Due to the lack of a second source, the density in the region beside the antenna reduces from the yellow highlighted region to the purple highlighted region in Fig. 4.9. Note that as the density decreases, the model predicts a much larger plasma sheath voltage drop and, therefore, less effective sheath mitigation by the MACOR insulator. Fig. 4.10 shows measured plasma potential profiles for the MACOR experiment with and without the secondary LaB_6 source. The densities in the regions of expected hot spots in the left panel correspond to the yellow-shaded region in Fig. 4.9 while in the right panel, the expected hot-spot densities correspond to the purple-shaded region. As predicted by the model, we see a greater potential rectification on field lines connecting to the antenna in the lower-density case. Comparing the hot-spot region near $(x, y) = (-12, 11)$ cm, the rectified potential increases from about 9 Volts to 27 Volts. This additional data gives us further confidence in the voltage-divider model mentioned above.

The potential rectification results from both the MACOR-copper stack experiment and

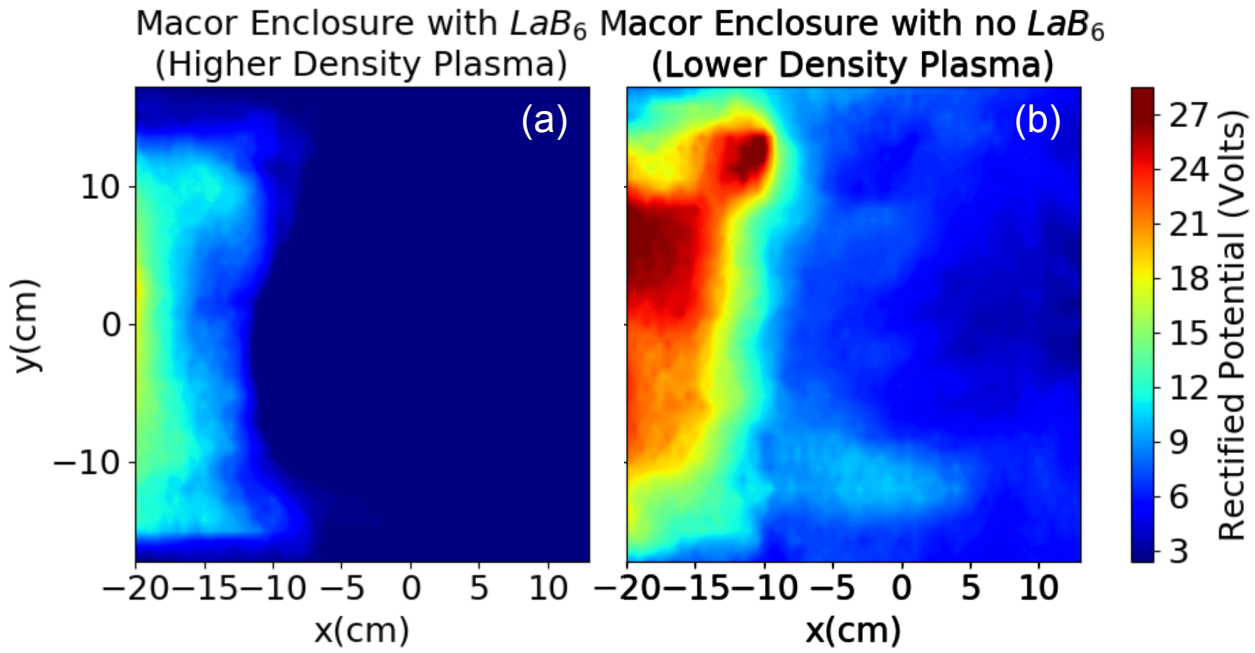

Figure 4.10: Effect of plasma density on sheath control. Panel (a) shows the plasma potential profile for the MACOR experiment with the additional LaB_6 plasma source. This profile shows clear mitigation of hot spots as predicted by Fig. 4.9. Panel (b) show the plasma potential profile for the MACOR experiment without the additional LaB_6 plasma source, leading to a lower-density plasma. As predicted in Fig. 4.9, we see an increase in rectified potential and clear reappearing of a hot-spot near $(x, y) = (-12, 11)$ cm.

the MACOR experiment support that the presence of conducting enclosure materials exposed to the plasma results in greater RF potential rectification. Figure 4.5b and c shows a plasma potential profile from the MACOR and MACOR-copper stack experiment. Although the expected hot spots near (x, y)= (-15, -11) cm and (-12, 10) cm are not present, it's important to note that the location of maximum rectified potential in these experiments occurs where the enclosure is still made of copper and exposed to the plasma chamber. In both the latter experiments, rectification is seen at x = -20 cm, near the back side of the antenna where copper coax is exposed to the plasma. Furthermore, in the MACOR-copper stack experiment, there is an additional region of rectification near (x,y) = (-15,13) cm, which corresponds to the top antenna enclosure with exposed copper. Although these rectified potentials for the MACOR and MACOR-copper cases are not nearly as high as 70 volts, they are greatest near the exposed copper surfaces.

Taken as a whole, these results indicate that replacing or masking the conducting enclosure material with DC electrically insulating enclosure material and thus breaking the DC connection between the antenna structure and the plasma can significantly reduce RF rectification. The absence of image currents on the enclosure sidewalls could further explain the lower rectified potentials in the MACOR case compared to the MACOR-copper case. The results presented in chapter 5 further explore the predicted sheath control voltage divider model by using different thicknesses of the MACOR layer and placing the antenna into regions of varying densities to explore the transition from efficient to poor sheath control.

CHAPTER 5

Effect of Plasma Parameters and Enclosure Material Properties on RF Sheath Mitigation

In chapter 4, the results have shown that replacing or covering plasma-facing components with MACOR (glass ceramic-an electrical insulator) significantly mitigates DC RF sheaths near ICRF antenna structures. Discussed in section 3.1.3, a Myra and others have presented 1D voltage divider model to predict the behavior of mitigation depending on the insulator material and plasma properties. In order to experimentally explore the impact of insulator material properties and plasma properties on the extent of sheath mitigation, a set of experiments were performed on the LAPD. These experiments were performed with copper, 1mm MACOR, 2mm MACOR, and 5mm MACOR enclosure walls. Additionally, each of these experiments was performed during varying plasma conditions by varying the time during discharge when the experiment was performed. In the copper enclosure experiment, RF rectified potentials were bench-marked for qualifying the extent of mitigation in the MACOR experiments. However, the model-predicted mitigation values from the varying MACOR thickness and plasma parameters do not quantitatively match the experiment results. The results show that sheath mitigation qualitatively follows the suggested trend of the voltage divider model, except for a few cases. For example, thicker MACOR walls are better at mitigating rectified RF sheaths, and the MACOR walls are better able to mitigate RF sheaths during higher-density plasma discharges. The voltage divider sheath model will likely need to take into account the 2D effects of evolving density and plasma potential to better predict sheath mitigation in these experiments.

5.1 Introduction

Results from LAPD in chapter 4 have reported on the plasma potential structures, convective cells, and mitigation of rectified plasma potentials via insulating antenna enclosure walls [1, 45]. Majeski's work [38] suggests that RF sheaths can be mitigated by adding insulators on and around antenna structures. A model for this mechanism is presented in D'Ippolito and Myra's work [9, 41]. This model is described in detail in section 3.1.3. The goal of this work is to quantify the effects of plasma parameters and material thickness of the insulator on the rectified sheath potential formed near the antenna.

This manuscript is organized as follows. Section 5.2 describes the machine parameters and its diagnostics used in the experiments. It also outlines the details of the different ICRF antenna enclosure material configurations. Section 5.3 compares the plasma potential results obtained during the copper and the three MACOR experiments at different times during the discharge. Section 5.4 discusses the results in detail and presents possible future experiments.

5.2 Experimental Setup and Diagnostics

This chapter will compare results from four experiments conducted on the LAPD. A schematic of the machine and the setup for this experiment are shown in Fig. 5.1. For the results presented in this chapter, the larger of the two sources was operated alone to generate a background plasma of density, $n \approx 5 \times 10^{12}\text{cm}^{-3}$, with a plasma diameter of approximately 36 cm in each experiment. The plasma discharge was operated at a 1 Hz repetition rate for a duration of 10 ms, with a few hundred kiloWatt discharge power. Each of the experiments was performed in a helium plasma with a background magnetic field of 1 kG.

In all four experiments, a high-power RF antenna with a single strap (100 kW, 2.4 MHz) was used to launch fast waves into the dense core of a magnetized helium plasma, which had

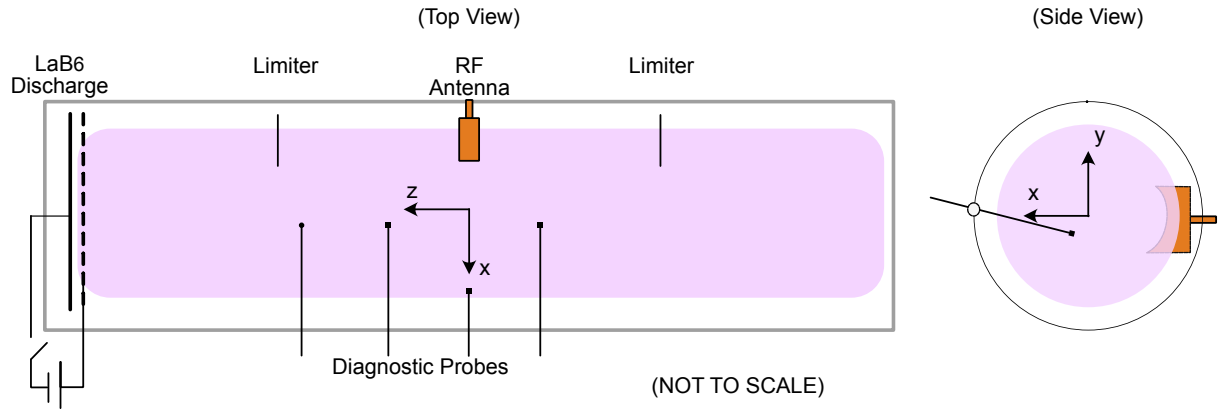

Figure 5.1: Top View of experimental setup on left and side view on the right, not to scale.
.

a density of $n_e \approx 5\times10^{12}$ cm^{-3} to 6×10^{12} cm^{-3} in each case. No Faraday screens were placed on the front face of the antenna enclosure in any of the experiments. The main difference in experiments was the material used for the sidewalls of the antenna enclosure. In the first experiment, the sidewalls were made of copper metal. In the remaining three experiments, the sidewalls were made of MACOR sheets of three different thicknesses: 1 mm, 2 mm, and 5 mm. The copper experiment was performed in order to measure the strength of the DC RF sheath and then used to quantify the extent of sheath mitigation as a function of MACOR thickness and plasma properties.

All four experiments were performed during different times of the discharge to study the response of the DC RF sheath to plasma density. In the results presented in this chapter, t = 0 ms refers to the start of the discharge, and t = 10 ms corresponds to the discharge turn-off, when the plasma density and temperature start to decay. Fig. 5.2 shows the core plasmas ion saturation as a proxy for density during the main discharge (t = 0 to 10ms) and the afterglow (t = 10ms and onward). The figure also highlights the 2ms time intervals during which 2D plasma potential data was collected. The highest-density experiments were performed during the main discharge starting at t = 8ms, depicted by the red interval. Subsequent lower-density experiments were performed during afterglow starting at t = 13,

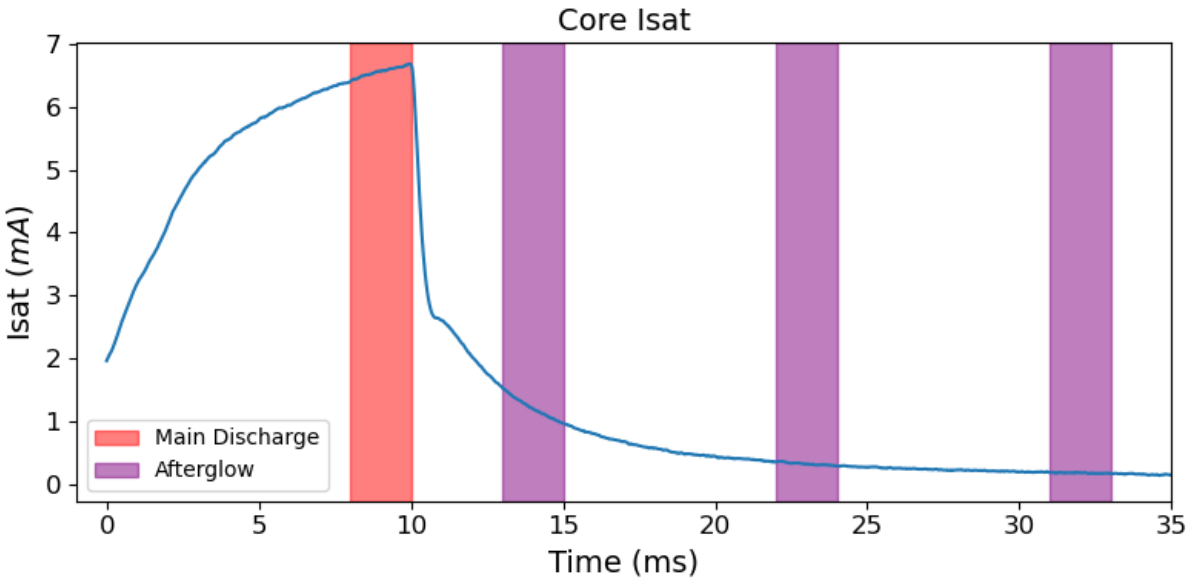

Figure 5.2: Core ion saturation of the plasma during the main discharge and afterglow. 2D data in the chapter was taken during 2ms intervals starting at t = 8, 13, 22, and 31ms.

.

22, and 31ms, depicted by the purple intervals. Additional data were collected at various single-point locations with a finer temporal resolution during the afterglow.

In each of the four experiments, data were collected using an emissive, magnetic pickup, and Langmuir probes. These probes were inserted into the LAPD plasma through ball valves located at intervals of 32 cm along the length of the machine. Each moving probe was mounted on a motorized drive controlled by a computer, which regulated the probe's position during data collection. The plasma potential data presented in this chapter was collected at various xy planes at a fixed axial location within the machine.

Langmuir probes were utilized to assess the plasma's electron temperature and density, while an emissive probe was employed to determine the spatial plasma potential profiles [44]. While tungsten is often used to construct emissive probe tips, in this particular case, due to the high-density plasma, LaB_6 was used instead. LaB_6 was chosen for its mechanical stability at the high temperatures necessary for sufficient emission, which is an advantage

over tungsten in these conditions.

5.3 Results

5.3.1 Potential Rectification in Copper

In order to accurately quantify the extent of sheath mitigation as a function of plasma properties and thickness of MACOR, the DC RF sheath was measured for the case of a copper enclosure as a function of density. Fig. 5.3 shows the spatial profile of the rectified potential 64cm away from the antenna in the xy plane. This rectified potential profile was calculated by taking an average of the plasma potential during the 2ms long RF pulse and subtracting the average plasma potential while the RF pulse was off. Since there was some variation in antenna current between data runs, peak-to-peak antenna current in kA was used to normalize the rectified potential. Prior results published from similar experiments have shown a linear scaling of rectified potential as a function of antenna current [45]; therefore, we can reasonably compare rectified potentials normalized by the antenna current between runs. As shown in Fig.5.3a, with the copper enclosure, during the main discharge, a DC RF sheath of approximately 95V/kA was measured in the region of the top hot spot and approximately 50 V/kA in the bottom hot spot. These current normalized potentials correspond to rectified potentials of 85 Volts and 45V, respectively. As shown in Fig. 5.3b, the same measurement was repeated in the afterglow 3ms after the plasma discharge was shut off at t = 13ms. These measurements show some minor changes in the spatial structure of the rectified potentials during the high-density main discharge vs. the lower-density early afterglow. Furthermore, to quantify the DC RF sheath over a wide range of plasma densities, an array of 9 points was chosen in the top hot spot, centered around $(x, y) = (-17, 10)$, and the plasma potential was measured during the afterglow as the plasma density decayed overtime at t = 13, 16, 19, 22, 25, 28, and 31 ms. Fig. 5.4 shows the rectified plasma potential averaged over the 9 points in the top spot, as the plasma density decays, the rectified potential drops approximately

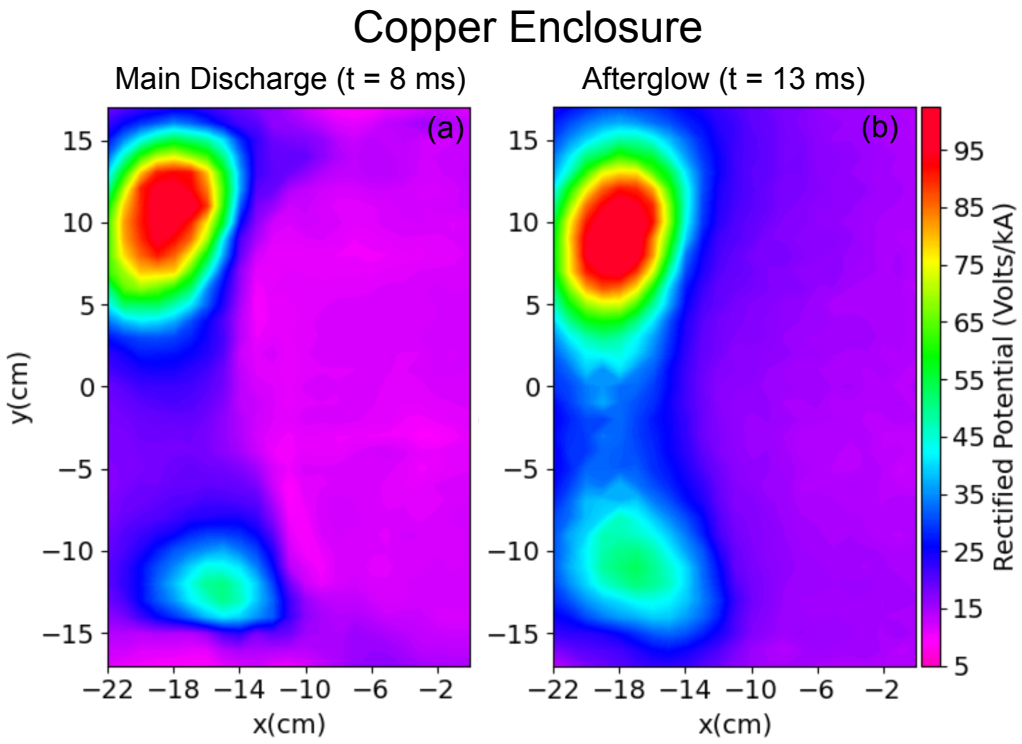

Figure 5.3: Plasma Potential Rectification profiles for the copper experiment at z = -64cm. (a)RF pulse starting at t = 8ms during the main plasma discharge (b)RF pulse starting at t = 13ms during early plasma afterglow

.

from 95 Volts to 65 Volts.

5.3.2 Sheath Mitigation with MACOR

Although sheath mitigation was demonstrated using 2mm MACOR sidewalls in previous work [45], this set of experiments was done in a larger plasma profile; therefore, sheath mitigation via MACOR enclosures was confirmed in each of the three MACOR cases. The experiment was carried out for all three cases during the high-density main discharge at t = 8ms. Fig. 5.5 shows the xy planar profile of the rectified plasma potential during the RF pulse. As mentioned, the rectified potential is obtained by taking a difference between the average plasma potential while the RF is on and the average plasma potential while the

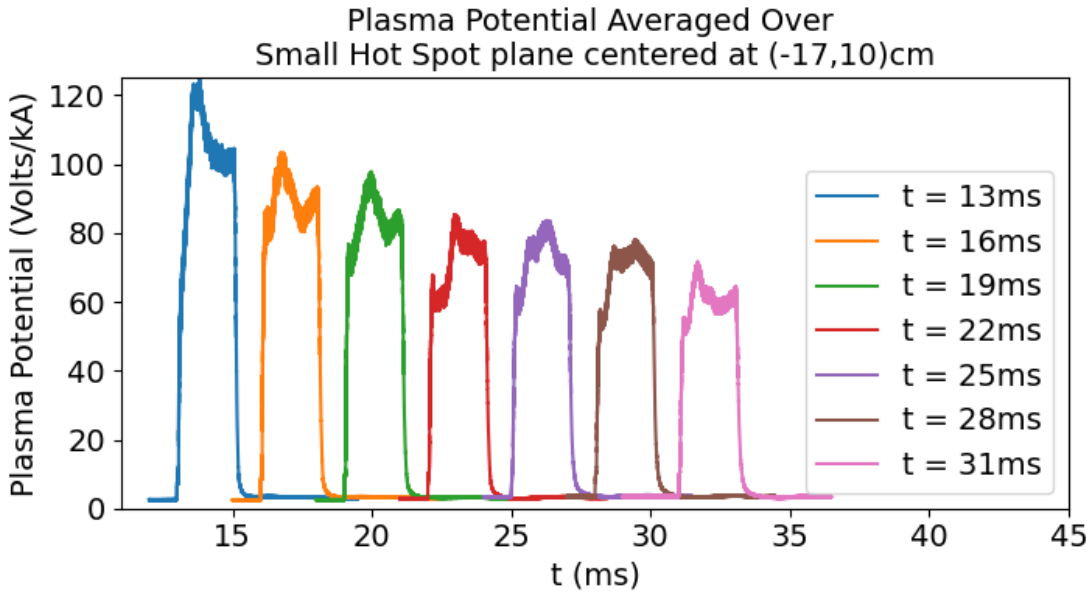

Figure 5.4: Rectified Potential in the hot spot during the plasma afterglow

RF is off. For all three cases, we observe a maximum rectification of about 4-10 V/kAmps in comparison to the 80 V/kAmps for the copper case. Additionally, it's important to note that at the location of the expected hot spot, the rectified plasma potential is less than a few V/kAmps. For the 2mm MACOR experiment, the location of the maximum rectified potential is near (x,y) = (-24,4)cm, which corresponds to the location of the copper coax attached to the antenna enclosure box. Since the coax has an exposed copper surface to the plasma, it makes sense that we observed some rectified potentials at this location. As mentioned earlier, these results for the 2mm MACOR case have been previously published along with corresponding density, wave fields, and power scaling.

5.3.3 Breakthrough rectification with MACOR during low-density afterglow

As shown in the previous section, the DC RF sheath was mitigated with the use of 1, 2, and 5mm MACOR enclosure material during the main discharge. According to the sheath-mitigation model presented by Myra et al., the insulating material is not as effective at

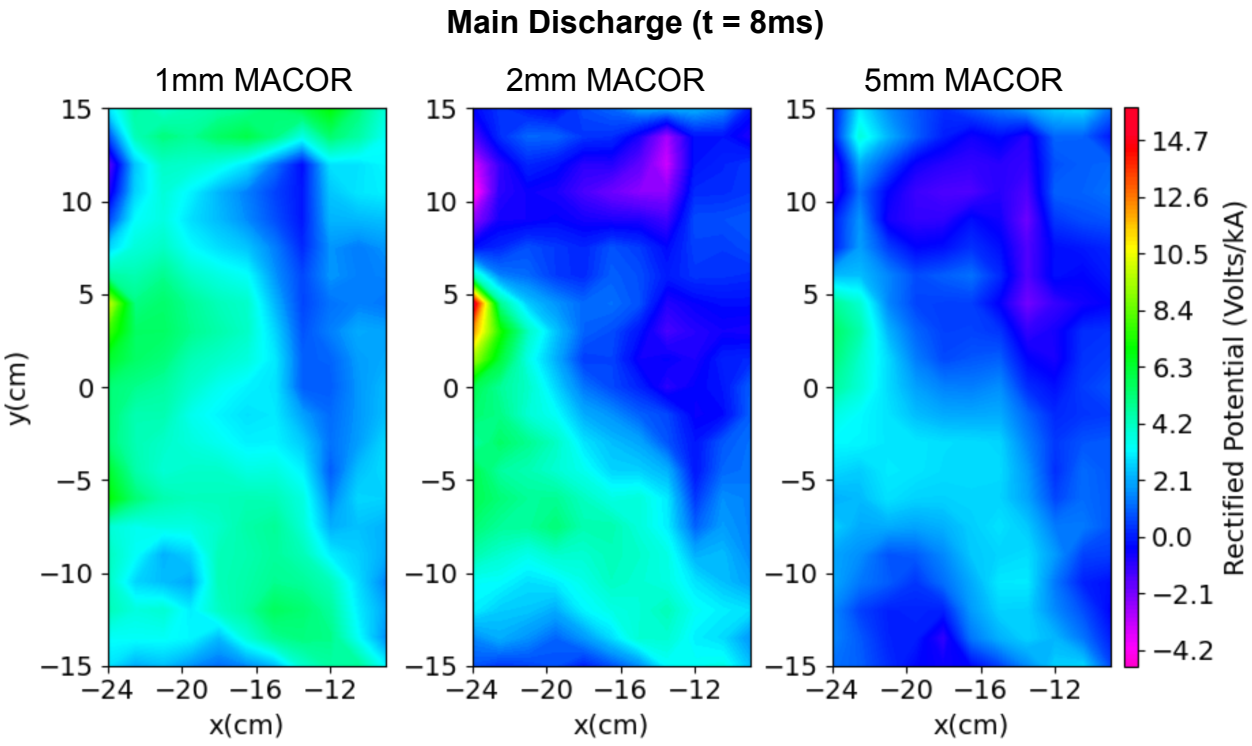

Figure 5.5: Plasma potential rectification profiles for the three MACOR cases acquired during the main plasma discharge at 8ms and at z = -64cm. (a) MACOR 1mm (b) MACOR 2mm (c) MACOR 5mm

mitigating the plasma sheath at lower densities and with thinner insulating material. In order to measure the extent of breakthrough rectification as a function of plasma density, for each of the MACOR experiments, the RF pulse was launched at t = 13, 22, and 31 ms for a duration of 2ms in the afterglow. As seen in Fig. 5.6, in the case of 1mm and 5mm MACOR enclosures, we see progressively increasing rectified plasma potential as the density decreases late into the afterglow. As shown in Fig. 5.6 d-e, for the 2mm MACOR case, we observe a peculiar result where the spatial size of the rectified region seems to decrease from t = 22 ms to t = 31 ms. This is unexpected because we would expect greater breakthrough rectification at lower densities. Next, as we compare the rectified potential profiles for a fixed time in the three different enclosure cases, we see that at t =13 and 22 ms, the magnitude of rectified potential and the size of the hot spot both decrease with increasing MACOR thickness. At t = 31ms, we first see the size of the hot spot decrease when comparing 1mm MACOR to 2mm MACOR, but for 5mm MACOR, the size of the hot spot unexpectedly increases. In summary, Fig. 5.6 demonstrates changes in the magnitude and spatial size of the rectified plasma potential as density decreases later into the afterglow and as the MACOR enclosure thickness increases between experiments.

In addition to the 2D plasma potential data acquired at 13ms, 22ms, and 31ms, plasma potential data was taken at a single point over a period of 200ms for the cases of 1mm and 5mm MACOR. This data was acquired at $(x, y) = (-12, 20)$cm. Since the hot spot with the highest rectified potential migrated up and to the right for the MACOR enclosure cases, the single point was chosen to be at the center of this hot spot. Fig. 5.7 shows the rectified plasma potential at $(x, y) = (-12, 20)$cm for the 1mm and 5mm MACOR case. The rectified potential for both cases at this location is nearly equal until 40ms during the afterglow. After 40ms, the rectified potential for the thinner 1mm MACOR enclosure is a few V/kA greater than the 5mm MACOR case. Additionally, according to the voltage-divider model, we would expect the rectified potential to continuously increase and eventually plateau as the density decays during the afterglow. But here, we observe that the rectified potential

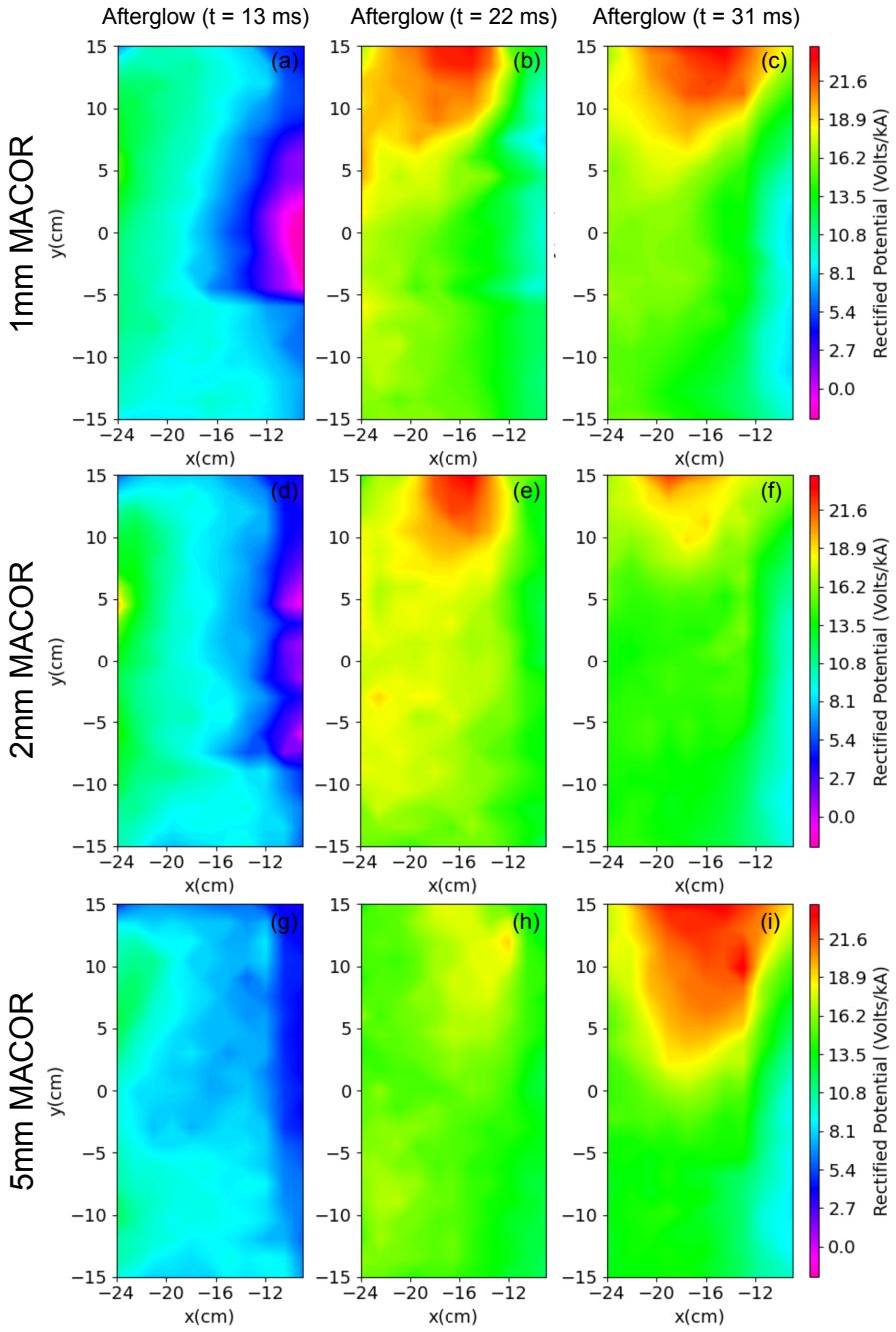

Figure 5.6: Plasma potential rectification profiles for the three different thickness MACOR enclosures during the afterglow at t = 13, 22, and 31ms. (a) 1mm MACOR at t = 13 ms (b) 1mm MACOR at t = 22 ms (c) 1mm MACOR at t = 31 ms (d) 2mm MACOR at t = 13 ms (e) 2mm MACOR at t = 22 ms (f) 2mm MACOR at t = 31 ms (g) 5mm MACOR at t = 13 ms (h) 5mm MACOR at t = 22 ms (i) 5mm MACOR at t = 31 ms

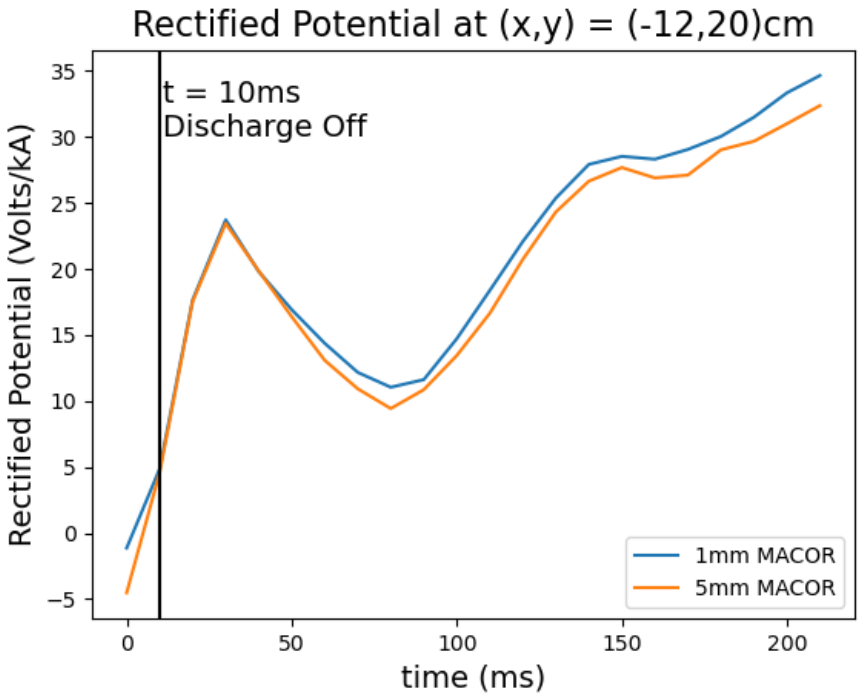

Figure 5.7: Rectified plasma potential normalized by antenna current at (x,y) = (-12,20) cm for 1mm and 5mm MACOR enclosures.

unexpectedly decreases between 30 to 80 ms even though the density continues to decrease continuously after 10 ms.

5.4 Discussion

In this chapter, we have described four different experiments on the LAPD that use the same RF fast wave antenna in different enclosures. The four enclosures had sidewalls made of copper, 1mm thick MACOR, 2mm thick MACOR, and 5mm thick MACOR. Each of the four experiments was performed at different times during the discharge to explore the dependence of plasma parameters on the DC RF sheath. In the results section, we have reported the 2D plasma potential profiles showing evidence of any RF rectification for each of the four experiments at different times in the discharge and afterglow. We have also

presented plasma potential measured at a single as a function of time in the afterglow.

As seen in Fig. 5.3 there are two signification regions of RF rectification for the copper enclosure case. These two hot spots formed near $(x, y) = (-18, 10)$ and $(-16, -12)$. While comparing the potential profile in Fig. 5.3a vs. Fig. 5.3b, there is a small shift in the location of the hot spot at 8 ms vs. 13 ms. This small shift is likely due to the changing density profile since the density begins to decay once the discharge is turned off at 10ms. These results provide a reference for the maximum expected RF rectification when there is no MACOR present to mitigate the RF sheath. Since the sheath mitigation model is a 1D model and does not account for the spatial distribution of the rectified potential, for comparison, we'll use the maximum rectified potential over the 2D plane in the copper case to quantify the extent of sheath mitigation. As seen in Fig. 5.3 at the top hot spot, we observe a rectified potential of 95V/kA.

In order to compare the results of sheath mitigation as a function of plasma density and temperature, Fig. 5.8 and 5.9 show the model prediction for the ratio between the sheath potential and the total potential drop across the insulator and plasma sheath for the three different thicknesses of MACOR during the main discharge (t = 8ms) and afterglow (t = 13, 22, and 31 ms). Note that the curves in Fig. 5.8 were calculated at $T_e = 2eV$, and it has a single vertical dashed line at $n_e = 4 \times 10^{17} m^{-3}$, this corresponds to the edge plasma temperature and density at t =8 ms during the main discharge. And the curves in Fig. 5.9 were calculated at $T_e = 0.5eV$ and it has three vertical dashed line at $n_e = 2 \times 10^{17} m^{-3}$, $1.5 \times 10^{17} m^{-3}$, and $5 \times 10^{16} m^{-3}$, these lines correspond to the edge plasma density at t =13, 22, and 31 ms with a corresponding electron temperature of 0.5eV during the afterglow. According to Fig. 5.8, none of the three MACOR cases should show any significant rectification at 8ms, and the plasma potential profiles confirmed this in Fig. 5.5. All three cases show a maximum rectification of 2-7V/kA. With the exception of a small area in the 2mm MACOR case that shows rectification of about 15V/kA at $(x, y) = (-24, 4)cm$. The rectification at this location is due to exposed copper coax at the back of the antenna

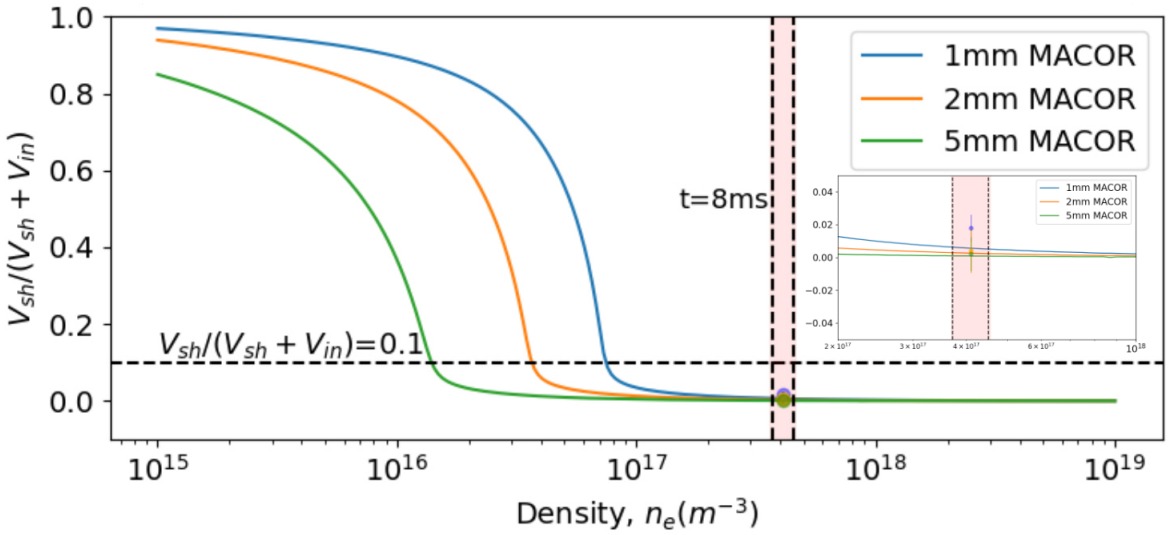

Figure 5.8: Predicted sheath control due to insulating side-walls: $V_{sh}/(V_{sh}+V_{in})$ as a function of density for 1mm, 2mm, and 5mm MACOR thickness enclosure walls. The dashed vertical line corresponds to the density in the expected hot spot at t = 8 ms. The three data points with error bars are shown for the measured rectified potential at 8 ms for the three cases of 1mm, 2mm, and 5mm MACOR. Note that the plot inset shows the data points with error bars more clearly.

enclosure box.

According to Fig. 5.9 at t = 13 ms, all three MACOR experiments should exhibit plasma potential less than 10% of the maximum rectified potential of 95V/Amp. The results shown in Fig. 5.6a,d, and g, show a maximum rectified potential of about 10 Volts during the t = 13ms potential profiles. Although the rectified potential is not well under 10% of the maximum value, we still see that the DC potential is significantly reduced at t = 13ms.

Next, according to the vertical line at t = 22ms in Fig. 5.9, we expect to see rectified potentials that are 20% of the maximum rectified potential in the case of 1mm MACOR experiment. For the case of 2mm and 5mm MACOR, the rectified potentials should be

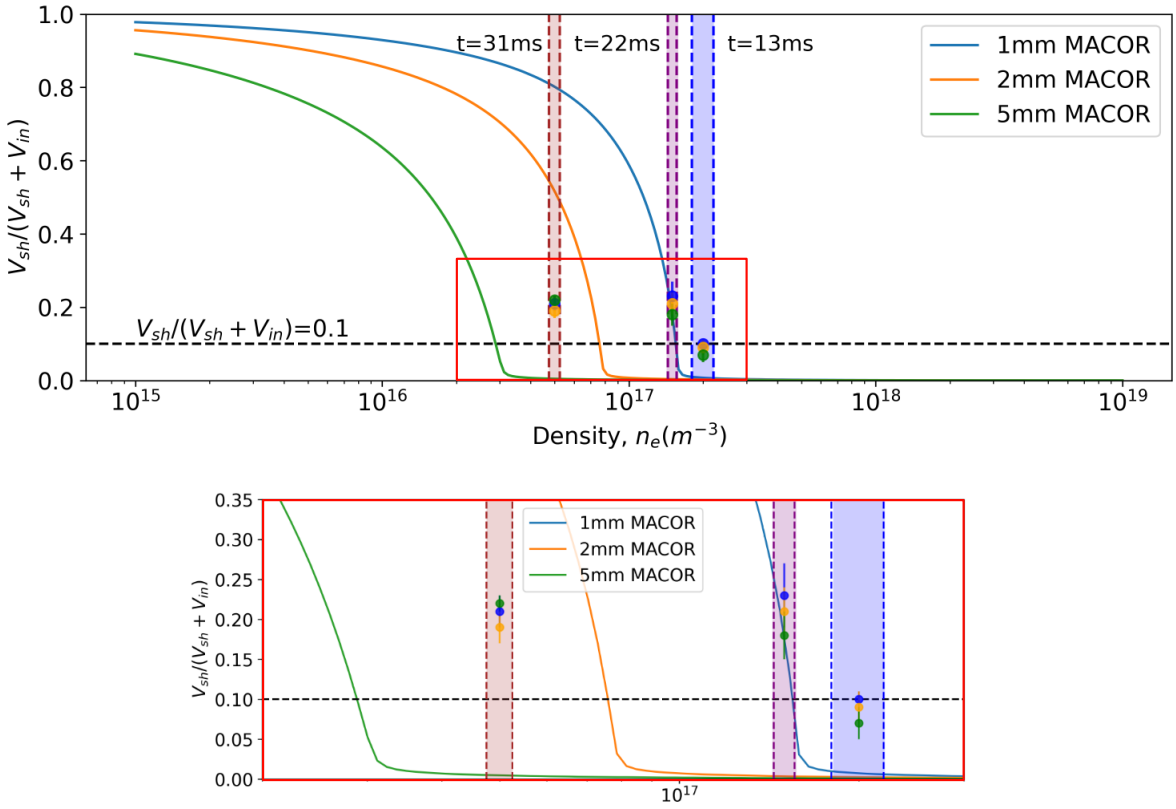

Figure 5.9: Predicted sheath control due to insulating side-walls: $V_{sh}/(V_{sh}+V_{in})$ as a function of density for 1mm, 2mm, and 5mm MACOR thickness enclosure walls. The dashed vertical lines correspond to densities in the expected hot spot at t = 13, 22, and 31ms. The data points with error bars are shown for the measured rectified potential at 13, 22, and 31 ms for the three cases of 1mm, 2mm, and 5mm MACOR.

well below 10% of the maximum value. The results in Fig. 5.6b show that we recover approximately 22V/Amp of breakthrough rectification in the case of 1mm MACOR. This is about 22% of the maximum rectification, which matches well with the predicted value. Fig. 5.6e also shows approximately 22V/Amps of breakthrough rectification is recovered for 2mm MACOR, with the rectified region being smaller than the 1mm MACOR case. The results in Fig. 5.6h for the 5mm MACOR case shows a very small region where the rectified potential region reaches about 20 V/Amps of breakthrough rectification, which is 21% of the maximum rectification compared to the expected result of well below 10%. Although the specific values of breakthrough rectification don't agree well with the model-predicted values, the region of rectified potential does get smaller for thicker MACOR enclosures, which is in agreement with the model that predicts a greater extent of mitigation for thicker MACOR enclosures.

Lastly, according to the vertical line at t = 31ms in Fig. 5.9, we expect to see rectified potentials that are 82%, 55%, and <10% of the maximum rectification in the case of 1mm, 2mm, and 5mm respectively. The results in Fig. 5.6c, f, and i all show a maximum breakthrough rectification of about 22 V/Amps, which is again about 22% of the maximum rectification. In this case, not only does the maximum rectification not match the predicted model values, but we also see a peculiar trend with the size of the hot-spot that shows the area of highest rectification. According to the model, we expect an improvement in sheath mitigation for thicker MACOR enclosures. But comparing results from 1mm and 2mm MACOR to 5mm MACOR at 31ms in Fig. 5.6c, f, and i, the 5mm case shows a larger area of rectified potential at the same magnitude of rectification. Since the model in consideration is a 1D model, we cannot use it to help discern what type of 2D changes are expected in potential as a function of plasma parameters and MACOR thickness. The results in Fig. 5.6 generally show larger DC sheath potentials for lower plasma density, as suggested by the model. Additionally, for the case of 13 and 22ms, the general trend shows larger areas of breakthrough rectification for the thinner MACOR enclosure cases.

The results captured at a single point in Fig. 5.7 show how the rectified potential changes as a function of discharge time at a single point. Fig. 5.2 shows that after the discharge is turned off at 10ms, the density continuously decays into the afterglow. And according to the sheath mitigation model predictions in Fig. 5.9, we expect the rectified potential to continuously increase as the density drops and eventually plateau to the maximum rectified potential. The results in Fig. 5.7 show that the rectified potential does, in fact, continuously increase till about 30 ms, then decreases until 80 ms, and then again increases between 80 to 200 ms. The drop in potential between 30 to 80 ms is unexpected and cannot be explained by the voltage divider model. This unexpected result of the plasma potential decreasing between 30 to 80ms points to characteristics of this experiment that are likely not well captured by the 1D sheath mitigation model. Although it's unclear what these unaccounted characteristics may include, the 2D spatial nature of this problem is not accounted for by the 1D voltage divider model.

The 2D plasma potential profiles in the Fig. 5.6 show changes in the extent of sheath mitigation both in the hot spot size and in the rectified potential's relative magnitude. Fig. 5.7 reveals an interesting feature of decreasing potential rectification during a portion of the afterglow. Future experiments can be conducted to explore better the mechanism that causes this feature by collecting spatial profiles of plasma potential and density at a few different times around 30 to 80ms.

CHAPTER 6

Coupling to the parasitic Slow-wave on the LAPD

Parasitic coupling to the slow wave in the low-density edge of tokamaks is a prominent deleterious effect associated with ICRF heating in fusion plasmas. Coupling to the slow wave is problematic for reasons including wasted RF power being carried away from the RF antenna and far-field sheath effects. Coupling to the slow wave must be well understood and mitigated in order to achieve efficient heating via ICRF. Experiments were performed on the Large Plasma Device (LAPD) at UCLA to document and study slow wave propagation in the low-density edge in front of the antenna with a single-strap RF antenna. Results from these experiments show both the short wavelength backward propagating slow wave in the edge as well as the longer wavelength forward propagating fast wave in the core.

6.1 Introduction

ICRH is one of the most prominent methods of heating plasmas for fusion experiments. ICRH has been used for heating in machines like JET, CMOD, and ASDEX-U; additionally, there are plans to continue using ICRH on future devices, including ITER and SPARC. One of the inherent issues with ICRH is wave coupling, that is, coupling power to the fast wave in the core for heating. An ICRH antenna is often placed in the low-density scrape-off layer (SOL) of a Tokamak. Conversely, slow waves are evanescent above the lower-hybrid resonance density and propagate below the resonance density limit in the low-density SOL. This is problematic because the location of the antenna and the plasma density in front of the antenna favorably couple to the slow wave. A portion of the RF power gets pumped into

the slow wave, which often causes other issues, such as far-field sheaths. Slow waves have a dominant electric field parallel to the background magnetic field and are often launched due to the current strap not being perfectly perpendicular to the background field. Faraday screens are often used to short out electric fields along the background magnetic field that are responsible for coupling to the slow-wave [46]. The Faraday screen components are, in theory, designed to be parallel to the background magnetic field but are often not aligned precisely to the combined toroidal and poloidal magnetic fields. Therefore they are not fully adequate in preventing coupling to the slow wave.

6.2 Experimental Setup and Diagnostics

This chapter will present results from experiments all carried out in the LAPD with a single-strap RF antenna previously described in section 2.3. The antenna enclosure can be moved in and out of the machine to be placed at a desired location, either in the plasma edge or closer to the core. Additionally, as shown in Fig. 6.1, a Faraday Screen (FS) can be added in front of the antenna strap to minimize $E_{\parallel}$ fields from the antenna. The FS was only used for some of the results presented in this chapter. The results that come from experiments with FS will be labeled accordingly in the results section. Once the entire antenna box is inserted into the LAPD cylindrical volume, the antenna assembly can also be rotated such that the FS screen can be aligned or offset by a desired angle with respect to the background magnetic field. Similarly, the results from experiments with rotated antenna straps will also be labeled accordingly in the results section.

The general setup for this experiment is very similar to the setup described in sections 4.0.2 and 5.2. A number of different diagnostics were used to acquire the data presented in this work. All the electric field data was acquired using 3-axis dipole probes. These probes have a pair of insulated conductors with small whiskers exposed to the plasma for each direction of measurement. The difference in the floating potential is representative of the

Figure 6.1: Single-Strap RF Antenna with Faraday Screen

.

electric field as long as there aren't any temperature gradients or electron tails. The density measurements were all acquired using Langmuir probes. Ion saturation measurements and sweeps are recorded for radial density profile measurements.

6.3 Slow and fast mode dispersion

The dispersion relation for the fast and slow wave as a function of density is shown in Fig. 6.2 for typical LAPD parameters. This plot shows that the slow wave propagates below the lower-hybrid resonance at $n \approx 7 \times 10^{15} m^{-3}$. Additionally, the fast wave propagates above the cutoff at $n \approx 2 \times 10^{18} m^{-3}$. There are nearly three orders of magnitude difference in density for both these waves to propagate simultaneously in the LAPD. Due to the difference in the scaling of the cutoff and resonance depending on the density and background magnetic field, for typical Tokamak parameters, with a significantly larger background magnetic field, the separation in density between the fast wave cut-off and the LH resonance is about an order of magnitude.

The large separation in density for slow wave and fast wave propagation in LAPD parameters presents a big challenge in these experiments. In order to achieve a desirable LAPD profile, the plasma profile is tailored by the background magnetic field and by carrying out the experiment at the beginning of the discharge. First, the profile is tailored by setting the field at the sources to 350 Gauss and the main length of the machine to 1700 Gauss. Since the antenna is located in the 1700 Gauss section, the field ratio squeezes the plasma profile down by a factor of approximately 2.2 in front of the antenna. Secondly, the experiments are done during the first 5ms of the discharge. At the start of the discharge, the core density is high, and the edge density is very low. As time progresses, the plasma profile expands and fills up the edges of the machine. Fig. 6.3 shows the radial density profile of the LAPD during the first 5ms of the discharge. As a result of tailoring the background magnetic field profile, the density profile was tailored such that it allowed fast-wave propagation in the

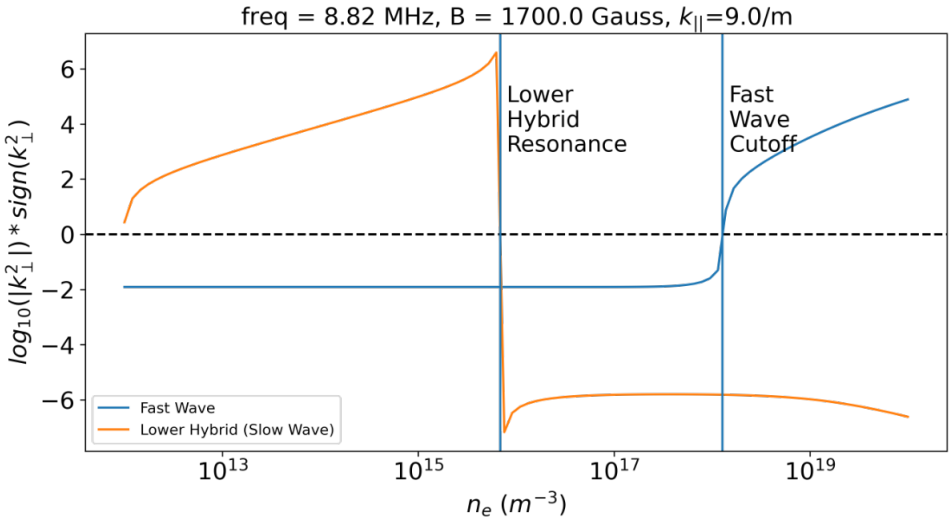

Figure 6.2: Slow and fast mode dispersion as a function of density in LAPD plasma parameters.

.

dense core and slow-wave propagation in the much lower-density edge.The wave propagation in this density profile is shown in Fig. 6.4 where there is a backward propagating short perpendicular wavelength feature in the edge and a much larger perpendicular wavelength feature in the core.

6.4 Results

6.4.1 Slow Wave propagation in the low-density edge of LAPD

The results shown in Fig. 6.4 contain x-t planes of the parallel electric field in the antenna side edge of the LAPD. For these experiments, a solid copper box enclosure was used, as should in Fig. 6.1, but without the Faraday screen. The front of the antenna was placed at $x = -41cm$, and the electric field measurements were taken along a line in the x-direction at $z = 96cm$ (3 ports away from the antenna). Note that the location of the antenna is defined as $z = 0cm$ for reference. Additionally, a favorable density profile was achieved by

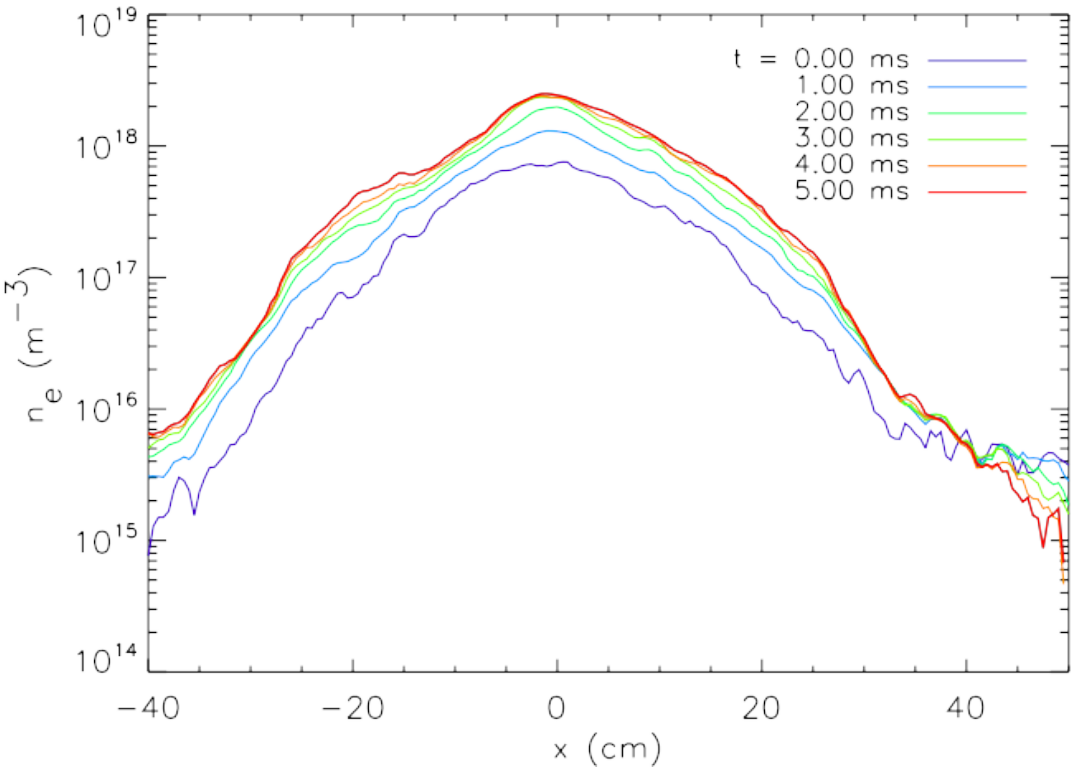

Figure 6.3: Radial density profile in the LAPD during the first 5ms of the discharge [10].

setting the background field to 350 Gausss near the sources and to 1700 Gauss in the section around the antenna. In Fig. 6.4, the two left panels show unfiltered $E_{\|}$ data as a function of x with time progressing in the $+y$ direction of the plots. Note that both plots have two main features labeled on the figure. The first is the longer wavelength features closer to the core, which signifies the fast-wave. Second, there are more faint features near $x \approx -36cm$ with a much shorter perpendicular wavelength; this is the backward propagating slow-wave in the low-density edge. We can tell that this wave is backward propagating because the feature moves outwards toward the antenna as time progresses upwards. Comparing Fig. 6.4c to a, we notice that the slow-wave feature moves outward in the machine from $x = -36cm$ at $t = 50\mu s$ to $x = -37cm$ at $t = 800\mu s$. This is a consequence of the density evolution during the discharge. Evident from Fig. 6.3, as the discharge builds, the density in the edge also increases, and the LH resonance density limit moves outwards in the machine. Therefore, the slow-wave propagation is observed further out in the machine as time progresses.

6.4.2 Dependence of density profile evolution on RMS fluctuations

Figure 6.5 also clearly shows the density dependence of slow wave propagation. Using the data shown in Fig. 6.4, RMS fluctuation amplitudes of $E_{\|}$ at different times during the discharge were calculated and are shown in Fig. 6.5. Note that these RMS fluctuations are plotted mainly for the edge of the plasma showing the RMS amplitudes of the slow wave. The peak amplitude for $t = 0$, when the discharge is still developing, is centered at $x = -36cm$ while the peak amplitude for $t = 5ms$, when the discharge is further developed, and the plasma density has moved outward, is centered at $x = -38cm$. Overall the peak amplitude in the edge moves outward in time. This is in accordance with the density evolution observed in Fig. 6.3. As the plasma discharge evolves in the first 5ms, the density in builds and increases; therefore, the density needed for the slow mode to propagate also moves outward.

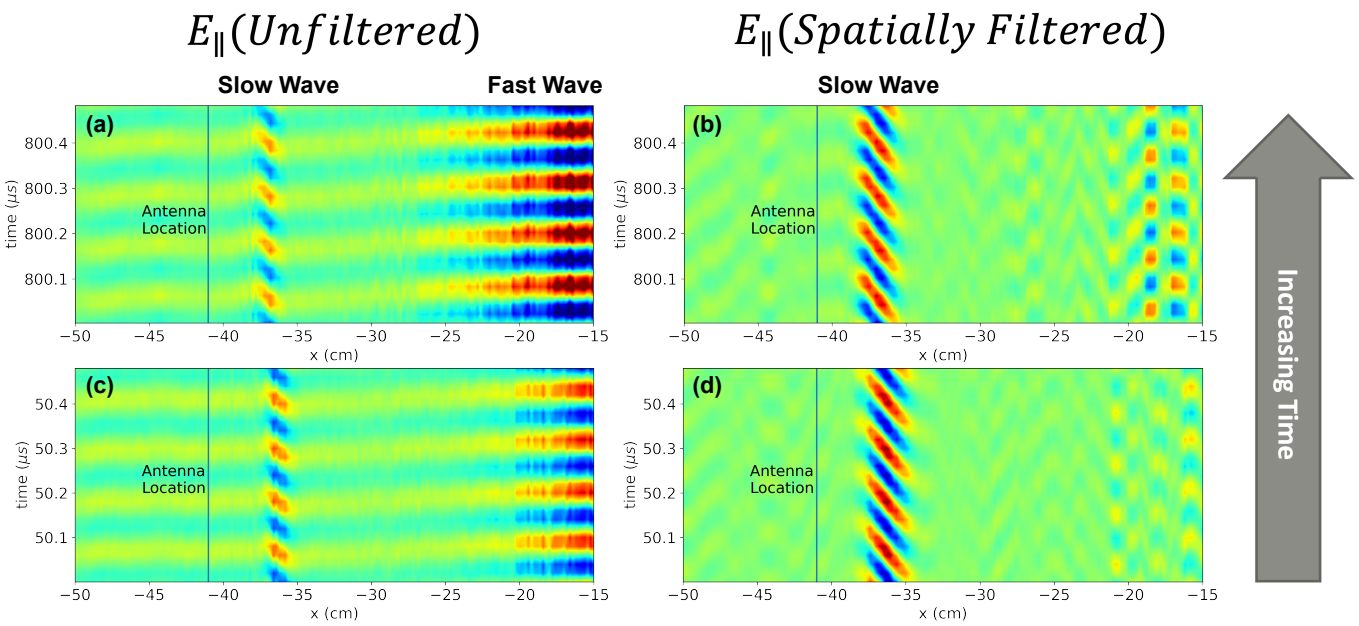

Figure 6.4: $E_{\parallel}$ as a function of radial position and time. Plots in panels (a) and (c) show the raw, unfiltered data. Plots in panels (b) and (d) were generated by applying a spatial filter to filter out long wavelength features. Note that time increases from bottom to top. This data was taken at z = 96cm, and recall that the antenna is placed at z = 0 [10].

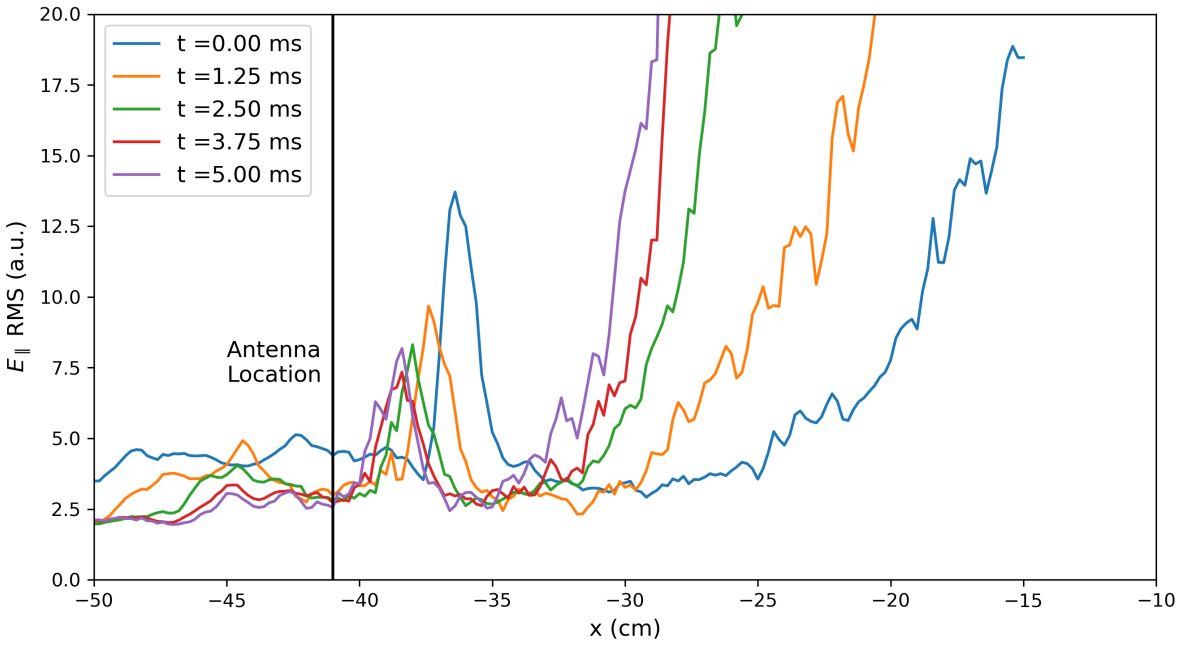

Figure 6.5: RMS fluctuations of $E_\parallel$ in the LAPD edge at different times during the discharge while the density builds up [10].

6.4.3 Antenna tilt angle scan with Faraday shield

In the next set of experiments, a Faraday screen was placed in front of the antenna, as shown in Fig. 6.1. These experiments aimed to compare the amount of power coupled to the slow wave while the alignment between the Faraday screen and the background magnetic field is varied. As shown in Fig. 6.6a, α, is defined as the angle between the antenna strap and the y-axis. When $\alpha = 0$, the FS is perfectly aligned with the background magnetic field, and the coupling to the slow wave should be minimized. As α is gradually increased, the FS and the background magnetic field become more and more misaligned. As a result, the excited $E_{\parallel}$ also increases, and therefore more power is coupled to the slow-wave. Fig. 6.6b shows the power density of the wave electric field in the edge of the machine. When $\alpha = 0$, the wave electric-field power density is practically 0 in the edge. As α increases, so does the power density in the edge. The edge wave power density is highest for the largest tilt angle of $\alpha = 50°$.

6.4.4 Establishing operating slow-wave conditions with new cathode

The work summarized thus far was done using an old BaO cathode. The south-end cathode was upgraded from a BaO to a larger LaB_6 cathode in 2020 [10]. The upgraded cathode allows for a larger and hotter plasma. Although these conditions expand the parameter regime for experiments that are possible on the LAPD, the expansion of the parameter regime makes the slow wave conditions more challenging to achieve. Since the upgraded cathode results in a larger and denser plasma, it is, therefore respectively, more challenging to achieve low enough density for slow-wave propagation in the edge. After this upgrade, a set of experiments were done on the LAPD to find discharge conditions where the slow wave can be launched and documented.

The first set of experiments aimed to reproduce previously observed results. This was done by magnetically compressing the plasma and running at a relatively low discharge

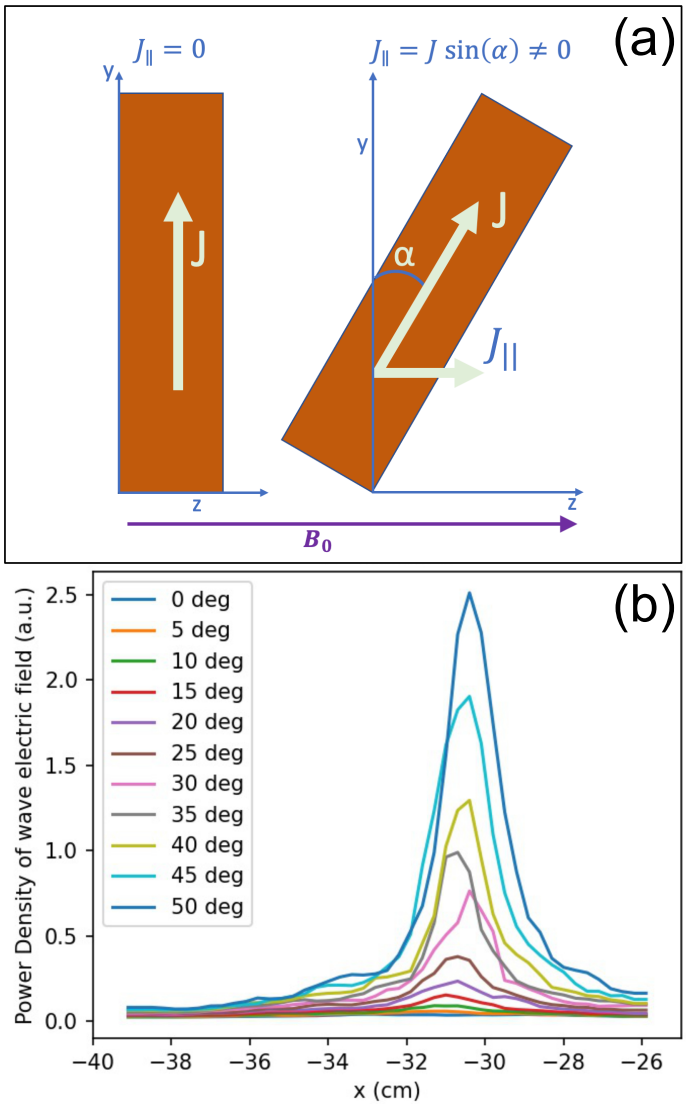

Figure 6.6: (a) A schematic of the antenna current strap in the LAPD coordinate system. Angle $\alpha = 0$ when the strap is perpendicular to the background magnetic field, and the Faraday Screen perfectly aligns with the background magnetic field. (b) Electric wave field power density as a function of the spatial coordinate x for several different angles, α [10].

current. The magnetic field at the cathode was set to 400 G, while the magnetic field in the main portion near the antenna was set to 2200 G. Additionally, the discharge was operated at approximately 2.5 to 3kA. Fig. 6.7 shows the Ex component of the wave in an xz plane of the edge plasma. The top two panels in this figure show the Ex component for two different times within one antenna cycle, separated by $0.1\mu s$. Comparing the two top panels at 12MHz, we notice that the edge feature near 35.5cm is propagating outward towards the antenna as time progresses. When comparing the bottom two panels for $f_{antenna} = 15MHz$, we notice that the edge feature is still propagating outward but is now at 33 cm. This makes sense for the slow wave since higher frequencies have a lower hybrid resonance at higher densities. Therefore the slow wave is able to propagate further inward in the plasma at higher frequencies.

This set of experiments was done with a variable frequency low-power (up to 500 Watts) amplifier where the frequency was scanned in a range of 2 to 15MHz. For frequencies below 8MHz, the lower-hybrid resonance was too low, and we were not able to document the slow wave in the far edge of the plasma. The big-picture goal of this work is to study slow-wave propagation at high power to document parasitic losses, quantify the effect of slow-wave coupling on fast-wave propagation in the core, and study far-field sheaths that can result from the $E \parallel$ component of the slow-wave. The high-power amplifier that was available for use in such experiments is a fixed-frequency amplifier at about 2.35MHz. After being able to document the slow wave down to 8MHz with a Helium plasma, there were a number of experiments performed in an effort to push the antenna frequency down to 2.35MHz and still be able to document the slow wave. This would allow us to do slow-wave experiments with the fixed-frequency high-power amplifier.

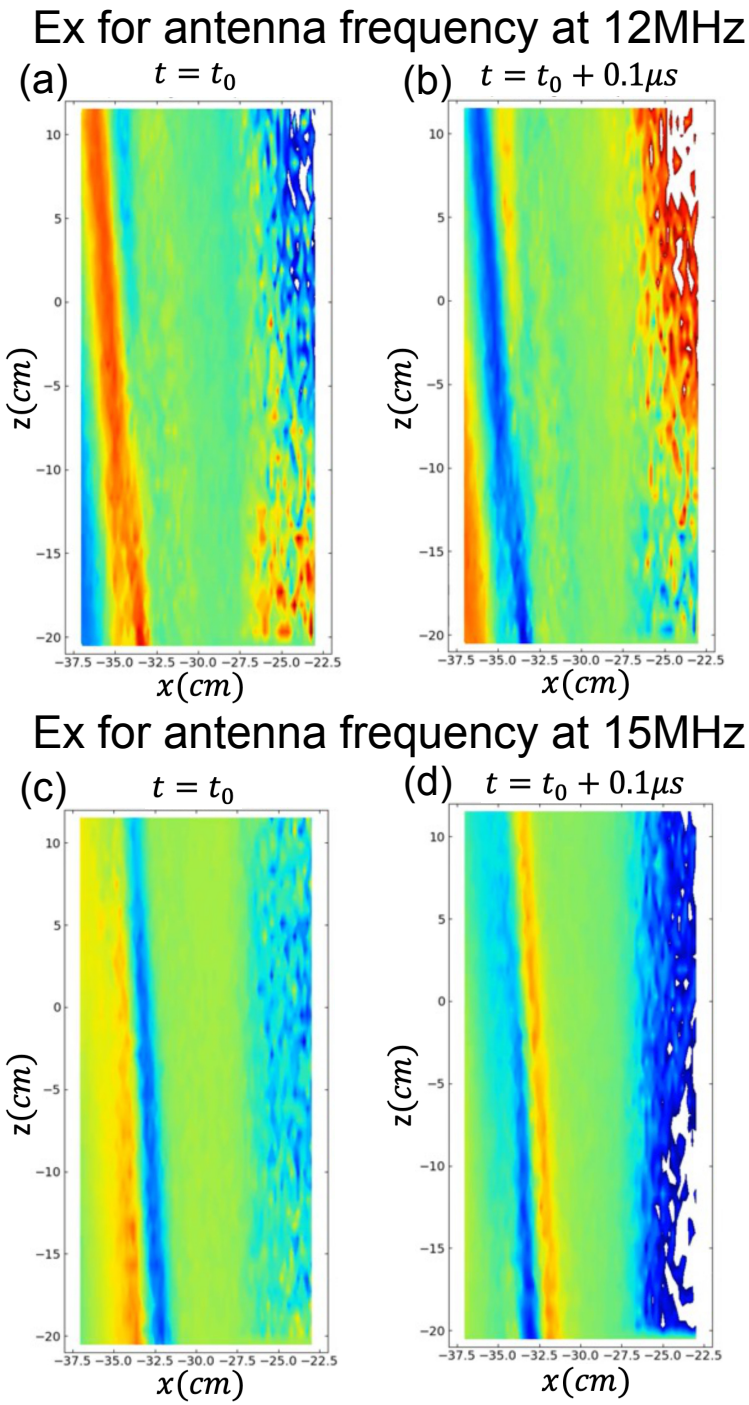

Figure 6.7: Ex component of the wave in the x-z plane. (a) Ex for $f_{antenna} = 12MHz$ at time t_0. (b) Ex for $f_{antenna} = 12MHz$ at time $t_0 + 0.1\mu s$. (c) Ex for $f_{antenna} = 15MHz$ at time t_0. (d) Ex for $f_{antenna} = 15MHz$ at time $t_0 + 0.1\mu s$.

6.4.5 Efforts to get lower density in the edge for slow-wave propagation at high power

One way to observe the slow wave for lower frequencies is to decrease the plasma density in the edge below the lower-hybrid resonance. There were a few different techniques that were tried to achieve this. The first was to lower the discharge current. But since we were already operating at a relatively low discharge current, we quickly entered the regime where we could no longer achieve consistent discharges because the anode voltage was too low to achieve breakdown. The next two efforts included using limiters to block out the primaries in the edge and produce a physically small plasma column. In these efforts, we used both the annular limiters and the rectangular limiters on the antenna side. Finally, the last effort to get lower density in the edge was to use biased annular limiters to spin the plasma to get reduced radial particle transport. These techniques allowed us to achieve the necessary density for slow wave propagation at 6MHz. But none of these efforts would help achieve the necessary density for 2.35MHz.

6.4.6 Exploring the use of Argon for low-frequency slow wave propagation

Another technique explored to achieve slow wave propagation at low density included using a heavier species plasma with a higher lower-hybrid resonance density. Fig. 6.8 shows the dispersion relation for typical LAPD parameters and $f_{antenna} = 2.35MHz$. The red curve shows the slow wave dispersion for Argon, and the orange curve shows the slow wave dispersion for Helium. Note that the lower-hybrid resonance for Ar is nearly an order of magnitude higher and, therefore, should allow us to achieve slow wave propagation with lower frequencies.

Similar to the Helium experiment summarized above, a frequency scan was done with an Argon plasma. Fig. 6.9 shows an x-t plot of the Ex component of the wave. In the right-most panel at 15MHz, we can clearly see the backward propagation feature centered around 38cm.

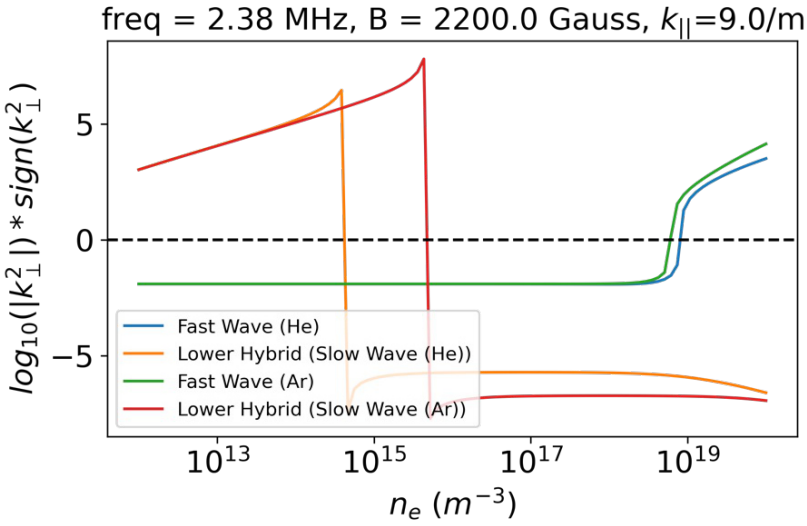

Figure 6.8: Fast and slow wave dispersion plots for typical LAPD parameters and $f_{antenna} = 2.35MHz$ including Helium and Argon species.

In the center panel at 4MHz, a backward propagating feature can still be observed centered around 41 cm. In the left-most plot at 3MHz, we no longer see any backward propagating slow wave features. As expected, as the frequency is lowered, the slow wave feature moves outward to lower density. But even with an Argon species, we were only able to lower the slow-wave frequency down to 4MHz. The results summarized above show that although we were able to achieve slow-wave propagation at lower frequencies with Argon in comparison to Helium. But we were still not able to lower the frequency far enough to use the available fixed-frequency high-power amplifier.

6.5 Discussion

In this chapter, we have presented results from experiments whose aim was to study slow wave propagation with and without the use of the Faraday screen on the single-strap RF antenna. As mentioned in the results, all the slow wave experiments were done at low power (<500W). Experiments summarized in sections 6.4.1, 6.4.2, and 6.4.3 were all done before

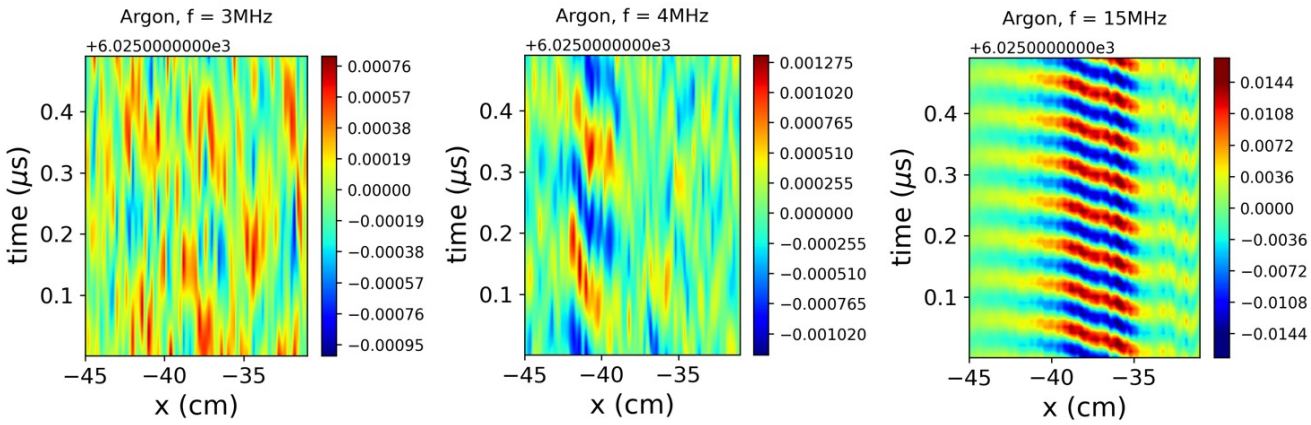

Figure 6.9: X-T plots for the Ex wave component in an Argon plasma with $f_{antenna}$ = 3, 4, and 15 MHz

the cathode upgrade in 2020. Results presented in sections 6.4.4, 6.4.5, and 6.4.6 were performed with the upgraded large LaB_6 cathode. As discussed earlier, ICRF antennae are often designed to maximize $J_\perp$ and therefore also maximize the launched $E_\perp$ in Tokamaks to couple to the fast wave. But due to some misalignment with the background magnetic field and fringing fields, the antenna can often have some $J_\parallel$ and $E_\parallel$, which can launch slow waves in the low-density edge.

The first set of results is presented in Figs. 6.4, and 6.5 are evident of situations where misalignment and fringing fields can result in launching the slow wave. For these experiments, although the antenna was in the "upright" position where the strap should only have a circulating $J_\perp$, the results show clear evidence of slow-wave propagation in the edge of the LAPD. The slow-wave results have all the characterization of a typical slow wave. In Fig. 6.4, we can see that the slow wave in the edge has a much shorter perpendicular wavelength compared to the portion of the fast wave seen in the core. The slow wave feature also has a phase velocity that propagates backward toward the launcher. In Fig. 6.5 we can see the RMS value of slow waves moving outward in time as the density builds. Knowing the fact that the slow wave dispersion has an upper-density limit beyond which the wave cannot

propagate due to the lower-hybrid resonance as seen in Fig. 6.2. According to Fig. 6.3 we expect the lower-hybrid resonance density limit to move outward in the machine as the discharge time progresses. This consequence can be observed in Fig. 6.5. The $E_{\parallel}$ RMS peak moves outward with discharge time as expected from the evolving density profile.

In order to minimize the effects of fringing fields and misalignment of the antenna strap, a Faraday screen is often used to minimize the $E_{\parallel}$ field launched by an Rf antenna. The second set of experiments studied the impact of rotating the antenna strap with respect to the background magnetic field on the amount of power coupled to the slow wave in the edge. Fig. 6.6a shows the definition of the tilt angle α in the LAPD coordinates. Fig. 6.6b shows the changing tilt angle's impact on the edge's wave power density. As expected, when the tilt angle is at its maximum of 50 degrees, we observe a maximum amount of power coupled to the slow wave in the edge. As the tilt angle is gradually decreased down to 0, we observe a gradual decrease in the edge wave power density.

After the 2020 cathode upgrade, additional experiments were done on the LAPD to reestablish conditions for slow-wave propagation. Section 6.4.4 shows results where the back-propagating slow wave was documented with the new cathode. The remaining work was done to explore whether we could use the existing fixed-frequency high-power amplifier to run high-power slow wave experiments. Through these experiments, we've learned that building a high-power RF supply at a frequency greater than 4MHz would be necessary to carry out high-power slow-wave experiments on the LAPD.

The results in this chapter demonstrate that the LAPD is a suitable test bed for slow-wave coupling experiments. These results were gathered from experiments carried out at low antenna power (<500W). But the framework for these experiments provides a path forward for carrying out similar tests at high power (about 100kW). By doing such experiments in the future, we can record parasitic losses and investigate how coupling to the slow wave affects fast-wave propagation in the core. Additionally, by doing slow-wave studies at high power, we would be able to observe and investigate far-field sheaths. The slow wave has dominant

$E_{parallel}$ fields, which can lead to far-field sheaths on plasma-facing components further down the machine.

CHAPTER 7

Conclusions and Future Work

7.1 Conclusions

The phenomena of RF sheath rectification and coupling to the lower hybrid (slow) wave greatly hinder ICRF heating in fusion plasmas. Making ICRF an efficient and effective method of heating for upcoming fusion devices requires addressing their impacts, such as impurity production, convective cell formation, etc. The work summarized in this thesis explores ways to better understand and mitigate RF-inducted DC sheaths and coupling to the lower hybrid (slow) wave. The chapter will be organized in the following way- key findings, the role of finding in the broader field, and potential for future work on the LAPD.

7.1.1 Key Findings

The overall goal of the RF-induced DC sheath mitigation work was to find ways to minimize the DC RF sheath next to the antenna enclosure and ensure that comparable power was still being coupled to the necessary fast wave in the core. The initial set of experiments summarized in Chapter 4, looked at how RF-induced DC sheaths were affected by electrically insulating antenna enclosures. With the aid of a matching network and high-power amplifier, a single-strap RF antenna was powered to launch fast waves in the dense LAPD core plasma. As a part of this thesis work, some improvements and alternations were made to the RF amplifier and the matching network. For instance, LT spice simulations helped determine the adjustments made to the matching network to optimize the current coupled to the

plasma. The antenna design was also upgraded to better protect against RF noise, which was corrupting various data streams and electronics. Comparisons were done between data from three distinct experiments where the enclosure materials were copper, MACOR (electrically insulating), and MACOR over copper, respectively. In the instance of the MACOR-copper side walls, the non-conductive MACOR material was exposed to the bulk plasma, while a layer of copper was placed below to allow image currents to flow. All three experiments were conducted in a helium plasma with a 1kG background magnetic field. During each experiment, the plasma's core density ranged from n_e around $5 \times 10^{12} cm^{-3}$ to $8 \times 10^{12} cm^{-3}$.

In the SOL region, where the antenna enclosure walls and the grounded limiters are connected by field lines, the copper experiment's plasma potential measurements reveal a sizable potential rectification of up to 90 Volts. While coupling similar wave power to the fast wave in the dense core of the plasma, for the MACOR and MACOR-copper stack studies, the results reveal a considerable reduction in RF rectification. Additionally, neither of the results from MACOR and copper-MAROR experiments showed any evidence of convective cell formation. The MACOR-copper experiment suggests that insulating plasma-facing materials have at least an equally strong impact on reducing potential rectification, as does replacing them entirely with insulating components.

In order to better understand the reduction in RF-induced sheaths and the role of material and plasma properties, another series of experiments were conducted with various thickness MACOR enclosures. Myra and colleagues have published a 1D voltage divider model to predict the mitigation behavior based on the insulator material and plasma characteristics. In order to explore the impact of insulator material and plasma characteristics on the level of sheath mitigation experimentally, a set of 4 experiments with different enclosures were carried out. The 4 enclosures included copper, 1mm MACOR, 2mm MACOR, and 5 mm MACOR. Each of these experiments was further carried out at different times during the discharge to explore the dependence of sheath mitigation on plasma density. The copper experiment was repeated to get a reliable benchmark value for RF-induced sheath potentials. The results

from the MACOR experiment during the main discharge confirmed previously found results of sheath mitigation during the high-density discharge such that rectified potentials observed during the main discharge with copper were completely mitigated for all three MACOR experiments. Next, the results during the low-density afterglow qualitatively showed worse mitigation with decreasing density and decreasing MACOR thickness. But the extent of mitigation predicted by the model did not match well with the experimental results. In fact, the experimental results showed better mitigation at low densities than was predicted by the model. The model in consideration is a 1D model that does not consider the effects of changing wave coupling with changing plasma density and 2D information on the plasma parameters and distribution of RF voltages on the antenna. The comparison between the model predictions and experimental results points to a need for a model that includes wave coupling, 2D information of plasma parameters, and distribution of RF voltages on the antenna to predict sheath mitigation.

Lastly, the parasitic lower hybrid (slow) wave in the LAPD edge was documented in addition to the sheath mitigation work described above. Plasma densities and temperatures in most fusion studies where coupling to the slow is a problem are frequently too high to allow for the placement of in-vessel diagnostics in the plasma volume. In the LAPD, densities, and temperatures are favorable for diagnosing the plasma volume with in-vessel probes. These experiments are distinctive because a fast-wave RF antenna was utilized to simultaneously launch the unwanted slow-wave in the edge and launch the fast-wave, which is employed for heating, in the core. Electric dipole probes were used to document this simultaneous coupling of waves. In order to improve the mapping of wave propagation along the length of the LAPD, two new dipole probes were constructed. Getting a range of densities in the LAPD covering the slow wave and fast wave propagation regions has been a major hurdle in this endeavor. In order to overcome this challenge, different approaches were tested for better wave accessibility. These approaches included employing annular limiters, square edge limiters, various species plasmas, and tailoring the plasma profile using the background

magnetic field. As a result of the work done for documenting slow-wave propagation with the new LaB_6 source, we are better prepared to conduct high-power slow-wave experiments for upcoming research.

7.1.2 Role of findings in the broader field of fusion research

The work with MACOR and copper-MACOR enclosures for demonstrating sheath mitigation during high-density discharges while coupling comparable power to the fast wave in the core paves the path forward for exploring insulating materials for covering PFCs of an RF antenna in a fusion device. These experiments were the first time where sheath reduction was documented, along with a 2D map of the plasma potential adjacent to the antenna.

These results and the results from the MACOR low-density (afterglow) experiments bring attention to the fact that the antenna structure and the rectified potential structure are complex and must be studied as a dynamic 2D problem. Additionally, the MACOR low-density (afterglow) results motivate the need for 2D sheath models that consider wave coupling, 2D information of plasma parameters, and distribution of RF voltages on the antenna.

Wave coupling studies on the LAPD using the single strap RF fast wave antenna have demonstrated that the problem of slow-wave propagation in the low-density edge region requires further attention and investigation. These results are a reminder that in order to effectively use ICRF heating in devices such as SPARC and ITER, we must tackle the issue of slow-wave coupling in the edge of tokamaks.

7.1.3 Potential for future work on the LAPD

Regarding near-field RF-induced sheath mitigation, further work can be done to understand better the dependence of plasma potential profile on the 2D potential profiles of the antenna walls. The walls of the antenna could be outfitted with probes for potential measurements

such that the enclosure wall potentials can me mapped out while the density and plasma potential are evolving during the discharge. Having this ability could shed light on how the changing core density and, therefore, the changing plasma coupling affects the enclosure wall potentials and the near-field rectified potentials.

Another peculiarity documented during the sheath mitigation experiments is shown in Fig. 5.7. Although we expected the rectified potential in the hotspot to monotonically increase as the density decreased, we unexpectedly observed a decrease in potential during a portion of the afterglow (during 30 to 80ms). Being able to track the enclosure wall potentials during this time could shed light on possible reasons for this unexpected drop in rectified potential. Such future experiments could also benefit from measuring the spatial profiles of plasma potential and density at a few different times, around 30 to 80ms.

Lastly, the low-power($<$500W) slow-wave coupling studies have demonstrated that the LAPD is an appropriate test bed for slow-wave coupling studies. The work presented in this thesis paves the way forward for doing analogous studies at high power (100kW). Such experiments would allow us to document parasitic losses and study how coupling to the slow-wave impacts fast-wave propagation in the core. Since the slow wave has a dominant $E_{\parallel}$, which can result in far-field sheaths on plasma-facing components down the machine, with significant power coupled to the slow wave, we would have the ability to document and study far-field sheaths.

REFERENCES

[1] M.J. Martin, W. Gekelman, B. Van Compernolle, P. Pribyl, and T. Carter. Experimental Observation of Convective Cell Formation due to a Fast Wave Antenna in the Large Plasma Device. *Phys. Rev. Lett.*, 119(205002):1–5, 2017.

[2] V Bobkov, F Braun, R Dux, A Herrmann, H Faugel, H Fünfgelder, A Kallenbach, R Neu, J-M Noterdaeme, R Ochoukov, et al. First results with 3-strap icrf antennas in asdex upgrade. *Nuclear Fusion*, 56(8):084001, 2016.

[3] Ph Chappuis, C Portafaix, E Thomas, B Bertrand, R Walton, V Riccardo, R Baker, I Barlow, A Kaye, A Lorenz, et al. Design of a limiter for the jet ep icrh antenna. *Fusion engineering and design*, 75:413–416, 2005.

[4] R Ochoukov, DG Whyte, I Faust, B LaBombard, B Lipschultz, O Meneghini, J Myra, G Wallace, and S Wukitch. Experimental investigation of rf sheath rectification in icrf and lh heated plasmas on alcator c-mod. In *AIP Conference Proceedings*, volume 1406, pages 207–210. American Institute of Physics, 2011.

[5] M Kubič, JP Gunn, L Colas, S Heuraux, E Faudot, and A Ngadjeu. Attenuation of icrh-induced potentials in the sol of tore supra. In *AIP Conference Proceedings*, volume 1406, pages 215–218. American Institute of Physics, 2011.

[6] V Bobkov, D Aguiam, R Bilato, S Brezinsek, L Colas, H Faugel, H Fünfgelder, A Herrmann, J Jacquot, A Kallenbach, et al. Making icrf power compatible with a high-z wall in asdex upgrade. *Plasma Physics and Controlled Fusion*, 59(1):014022, 2016.

[7] JR Myra, DA D'ippolito, DA Russell, LA Berry, EF Jaeger, and MD Carter. Nonlinear icrf-plasma interactions. *Nuclear Fusion*, 46(7):S455, 2006.

[8] H. S. Bulter and G. S. Kino. Plasma Sheath Formation by Radio-Frequency Fields. *AIP Phys. Fluids*, 6():1346–1355, 1963.

[9] JR Myra, DA D'ippolito, JA Rice, and CS Hazelton. Radio-frequency sheath mitigation by insulating antenna limiters. *Journal of nuclear materials*, 249(2-3):190–198, 1997.

[10] B Van Compernolle et al. Fast wave experiments on lapd in support of fusion. In *23rd Topical Conference on Radiofrequency Power in Plasmas, Hefei, China*, 2019.

[11] R Hemsworth, H Decamps, J Graceffa, B Schunke, M Tanaka, M Dremel, A Tanga, HPL De Esch, F Geli, J Milnes, et al. Status of the iter heating neutral beam system. *Nuclear Fusion*, 49(4):045006, 2009.

[12] MJ Singh, D Boilson, AR Polevoi, Toshihiro Oikawa, and Raphael Mitteau. Heating neutral beams for iter: negative ion sources to tune fusion plasmas. *New Journal of Physics*, 19(5):055004, 2017.

[13] Jiale Chen, Xiang Jian, Vincent S Chan, Zeyu Li, Zhao Deng, Guoqiang Li, Wenfeng Guo, Nan Shi, Xi Chen, et al. Self-consistent modeling of cfetr baseline scenarios for steady-state operation. *Plasma Physics and Controlled Fusion*, 59(7):075005, 2017.

[14] Xiang Jian, Jiale Chen, Vincent S Chan, Ge Zhuang, Guoqiang Li, Zhao Deng, Nan Shi, Guoliang Xu, Gary M Staebler, and Wenfeng Guo. Optimization of cfetr baseline performance by controlling rotation shear and pedestal collisionality through integrated modeling. *Nuclear Fusion*, 57(4):046012, 2017.

[15] P Vincenzi, J-F Artaud, E Fable, G Giruzzi, M Siccinio, and H Zohm. Neutral beam injection for demo alternative scenarios. *Fusion Engineering and Design*, 163:112119, 2021.

[16] Brian Lloyd. Overview of ecrh experimental results. *Plasma physics and controlled fusion*, 40(8A):A119, 1998.

[17] M Bornatici, R Cano, O De Barbieri, and F Engelmann. Electron cyclotron emission and absorption in fusion plasmas. *Nuclear Fusion*, 23(9):1153, 1983.

[18] T Omori, MA Henderson, F Albajar, S Alberti, U Baruah, TS Bigelow, B Beckett, R Bertizzolo, T Bonicelli, A Bruschi, et al. Overview of the iter ec h&cd system and its capabilities. *Fusion Engineering and Design*, 86(6-8):951–954, 2011.

[19] IH Hutchinson, R Boivin, F Bombarda, P Bonoli, S Fairfax, C Fiore, J Goetz, S Golovato, R Granetz, M Greenwald, et al. First results from alcator-c-mod. *Physics of Plasmas*, 1(5):1511–1518, 1994.

[20] Gregory Wallace. Behavior of lower hybrid waves in the scrape off layer of a diverted tokamak. 2009.

[21] MH Cho, C Chan, N Hershkowitz, and T Intrator. Measurement of vacuum space potential by an emissive probe. *Review of scientific instruments*, 55(4):631–632, 1984.

[22] Itsuo Katsumata and Moroe Okazaki. Ion sensitive probe-a new diagnostic method for plasma in magnetic fields. *Japanese Journal of Applied Physics*, 6(1):123, 1967.

[23] R Ochoukov, DG Whyte, D Brunner, I Cziegler, B LaBombard, B Lipschultz, J Myra, J Terry, and S Wukitch. Investigation of rf-enhanced plasma potentials on alcator c-mod. *Journal of Nuclear Materials*, 438:S875–S878, 2013.

[24] L Colas, JP Gunn, I Nanobashvili, V Petržílka, M Goniche, A Ekedahl, S Heuraux, E Joffrin, F Saint-Laurent, C Balorin, et al. 2-d mapping of icrf-induced sol perturbations in tore supra tokamak. *Journal of nuclear materials*, 363:555–559, 2007.

[25] Vl Bobkov, F Braun, R Dux, L Giannone, A Herrmann, A Kallenbach, HW Müller, R Neu, J-M Noterdaeme, Th Pütterich, et al. Operation of icrf antennas in a full tungsten environment in asdex upgrade. *Journal of nuclear materials*, 390:900–903, 2009.

[26] V Lancellotti, D Milanesio, R Maggiora, G Vecchi, and V Kyrytsya. Topica: an accurate and efficient numerical tool for analysis and design of icrf antennas. *Nuclear Fusion*, 46(7):S476, 2006.

[27] W Gekelman, H Pfister, Z Lucky, J Bamber, D Leneman, and J Maggs. Design, construction, and properties of the large plasma research device- the lapd at ucla. *Review of scientific instruments*, 62(12):2875–2883, 1991.

[28] Walter Gekelman, P Pribyl, Z Lucky, M Drandell, D Leneman, J Maggs, S Vincena, B Van Compernolle, SKP Tripathi, G Morales, et al. The upgraded large plasma device, a machine for studying frontier basic plasma physics. *Review of Scientific Instruments*, 87(2):025105, 2016.

[29] Robert L Merlino. Understanding langmuir probe current-voltage characteristics. *American Journal of Physics*, 75(12):1078–1085, 2007.

[30] Francis F Chen. Langmuir probe analysis for high density plasmas. *Physics of Plasmas*, 8(6):3029–3041, 2001.

[31] JP Sheehan and N Hershkowitz. Emissive probes. *Plasma Sources Science and Technology*, 20(6):063001, 2011.

[32] MJ Martin, J Bonde, W Gekelman, and P Pribyl. A resistively heated ceb6 emissive probe. *Review of Scientific Instruments*, 86(5):053507, 2015.

[33] ET Everson, P Pribyl, CG Constantin, A Zylstra, D Schaeffer, NL Kugland, and C Niemann. Design, construction, and calibration of a three-axis, high-frequency magnetic probe (b-dot probe) as a diagnostic for exploding plasmas. *Review of Scientific Instruments*, 80(11):113505, 2009.

[34] RL Stenzel. A new probe for measuring small electric fields in plasmas. *Review of scientific instruments*, 62(1):130–139, 1991.

[35] Stephen J Wukitch, RL Boivin, PT Bonoli, JA Goetz, J Irby, I Hutchinson, Y Lin, A Parisot, M Porkolab, E Marmar, et al. Investigation of performance limiting phenomena in a variable phase icrf antenna in alcator c-mod. *Plasma physics and controlled fusion*, 46(9):1479, 2004.

[36] SJ Wukitch, B Lipschultz, E Marmar, Y Lin, A Parisot, M Reinke, J Rice, J Terry, and C-Mod Team. Rf plasma edge interactions and their impact on icrf antenna performance in alcator c-mod. *Journal of nuclear materials*, 363:491–497, 2007.

[37] Michael John Martin. *Radio Frequency Enhanced Plasma Potential and Flows in the Scrap-Off Layer of an Active Antenna*. University of California, Los Angeles, 2017.

[38] R Majeski, PH Probert, T Tanaka, D Diebold, R Breun, M Doczy, R Fonck, N Hershkowitz, T Intrator, G McKee, et al. The phaedrus-t antenna system. *Fusion engineering and design*, 24(1-2):159–172, 1994.

[39] DA D'Ippolito, JR Myra, JA Rice, and CS Hazelton. Rf sheaths in spherical tokamaks and their control using insulating limiters. In *AIP Conference Proceedings*, volume 403, pages 463–466. American Institute of Physics, 1997.

[40] V Bobkov, D Aguiam, R Bilato, S Brezinsek, L Colas, A Czarnecka, P Dumortier, R Dux, H Faugel, H Fünfgelder, et al. Impact of icrf on the scrape-off layer and on plasma wall interactions: From present experiments to fusion reactor. *Nuclear Materials and Energy*, 18:131–140, 2019.

[41] DA D'Ippolito, JR Myra, JA Rice, and CS Hazelton. Rf sheaths in spherical tokamaks and their control using insulating limiters. In *AIP Conference Proceedings*, volume 403, pages 463–466. American Institute of Physics, 1997.

[42] W. Gekelman, P. Pribyl, Z. Lucky, M. Drandell, D. Leneman, J. Maggs, S. Vincena, B. Van Compernolle, S. K. P. Tripathi, G. Morales, T.A. Carter, y. Wang, and T. Dehaas. The upgraded Large Plasma Device, a machine for studying frontier basic plasma physics. *Rev. Sci. Instrum.*, 87(205002):1–19, 2017.

[43] D Leneman and W Gekelman. A novel angular motion vacuum feedthrough. *Review of Scientific Instruments*, 72(8):3473–3474, 2001.

[44] M.J. Martin, J. Bonde, W. Gekelman, and P. Pribyl. A restively heated CeB_6 emissive probe. *AIP ReView of Scientific Instruments*, 86(0535077):1–7, 2015.

[45] G Bal, BV Compernolle, P Pribyl, MJ Martin, J Larson, and TA Carter. Reduction in rf sheath rectification with insulating antenna enclosure walls. *Nuclear Fusion*, 62(8):086043, 2022.

[46] J-M Noterdaeme, F Ryter, M Söll, J Bäumler, G Becker, H-S Bosch, M Brambilla, F Braun, H Brocken, A Eberhagen, et al. The role of the faraday screen in icrf antennae: comparison of an optically open and optically closed screen in asdex. In *13th EPS Conference on Controlled Fusion and Plasma Physics*, pages 137–140. European Physical Society, 1986.